ABSTRACT

Title of Dissertation: SURFACE MODIFICATION OF METAL OXIDE NANO PARTICLES BY CAPILLARY CONDENSATION AND ITS APPLICATION

Seonmin Kim, Doctor of Philosopy, 2006

Dissertation directed by: Professor Sheryl H. Ehrman
Department of Chemical & Biomolecular Engineering

Titania nanoparticles were modified using tetraethyl orthosilicate in a capillary condensation process and nanoparticles interconnected by silica layers were obtained. The amount of the silica layer was tunable by adjusting saturation conditions and the thickness of the layer generally increased as the saturation ratio increased up to a saturation ratio of 1.0. However, layer thickness was significantly affected by the geometric dimensions of the space between nanoparticles.

Grand canonical Monte Carlo simulation was utilized in order to study the role of particle surface curvature and gap space between particles in capillary condensation. The curvature of the particle surface and the gap space played a crucial role in the meniscus formation. Simulation results suggested that the effect of gap space becomes significant at the saturation ratios less than 0.8 and the effect of the particle curvature is important near the saturation ratio of 1.0. From these results, these effects need to be considered for the formation of silica layers with a specific thickness.

In order to further investigate the effect of addition of a silica layer, photocatalytic activity of surface-modified bi-phase titania nanoparticles was characterized on the basis of a pseudo-first order kinetic model. The results indicate that surface modification can enhance the photoactivity of original titania nanoparticles when an optimal amount of silica layer is present on the surface of nanoparticles.

SURFACE MODIFICATION OF METAL OXIDE NANOPARTICLES BY CAPILLARY CONDENSATION AND ITS APPLICATION

by

Seonmin Kim

Dissertation submitted to the Faculty of the Graduate school of the
University of Maryland, College Park in partial fulfillment
of the requirements for the degree of
Doctor of Philosophy
2006

Advisory Committee:

Professor Sheryl H. Ehrman, Chair
Professor Gregory Jackson
Professor Lourdes G. Salamanca-Riba
Professor Srinivasa R. Raghavan
Professor Timothy A Barbari

© Copyright by

Seonmin Kim

2006

ACKNOWLEDGEMENTS

In completing this dissertation, I am very grateful for the guidance, support, and encouragement of my research advisor, Professor Ehrman. I also would like thank Professors Barbari, Salamanca-Riba, Raghavan, and Jackson for serving on my dissertation committee. I am deeply indebted to Professor Kyu Yong Choi for his generous encouragement of my academic career at the beginning of my graduate studies. This research was funded by the United States National Science Foundation (grant: DMR-0093649). The access to experimental facilities in the Brookhaven National Laboratory for the use of their EELS facility is gratefully acknowledged.

I would like to acknowledge discussions about TEM analysis of Professor Salamanca-Riba, and wisdom and insight about simulation programming of Professor Jackson. I also thank Tiejun Zhang for assistance with HRTEM measurement, Dr. Ranjan Pati for obtaining XRD result, Bindhu Varughese for assistance with XPS measurement, and Robert Kile and Lihua Zhang at Brookhaven National Laboratory for their assistance with EELS analysis. Many thanks to members of my research group at UMD, particularly Dr. Ranjan K. Pati.

I would like to show my appreciation to my soul mates in Korea (Dongho Kim and Byungsan Kang) and my friends in church. I was really grateful to many friends both physically and spiritually when I had hard time after sudden surgery. If they would not been close to me, it might take longer time to finish this dissertation.

Finally, I would like to thank my family in Korea including my sister and parents, who always support and aid my pursuit of this research. This fulfillment would not have been possible without my family.

TABLE OF CONTENTS

LIST OF FIGURES

Page

LIST OF TABLES

NOMENCLATURE

γ	surface tension
ΔP	pressure difference due to the surface curvature
V	volume per molecule
P_s	saturation pressure at the specific temperature
$\rho(\Gamma)$	probability density function
Q_{ens}	partition function for the ensemble
Ψ_{ens}	thermodynamic potential
$f(o \rightarrow n)$	flow of configuration o to n
$\alpha(o)$	probability generating configuration n from o
$acc(o \rightarrow n)$	probability of accepting a move in MC simulation
Γ	set of particle positions and momenta
H	Hamiltonian
A	Helmholtz free energy
k	adsorption rate
K	adsorption equilibrium constants
C	concentration of organic chemical in solution

Re	Reynolds number ($\rho v d / \eta$)
l_e	entrance length
ρ	density
C_p	heat capacity
k	thermal conductivity or reaction rate constant
D	diffusion coefficient
α	thermal diffusivity ($k / C_p \rho$)
T_e	temperature of bubbler
$T_{wall,1}$	wall temperature of pre-heating zone
$T_{wall,2}$	wall temperature of the chamber
$T_{atmosphere}$	temperature of outer medium
P/P_e	saturation ratio
θ_c	contact angle
κ	sum of the two principal curvatures
R_g	gas constant
θs	angle between the x-axis and the tangential line at the contact point
h	meniscus height
θ	angle of contact point for the parametric expression of particle surface

R and R' horizontal radius and vertical radius of particle

b_s binding energy

ε attractive energy between nearest neighbors

d gap space between two particles

c_i occupation number (0 or 1)

μ chemical potential

T_c critical temperature

μ_c critical chemical potential

I. INTRODUCTION

Nanotechnology has become incorporated into many existing engineering applications and has become more important for developing new materials. Nano-sized materials show unusual physical and chemical properties that differ from those of bulk materials. These different properties are thought to result from either of two reasons: the surface effect and the volume effect. The surface effect comes from surface atoms that form a high proportion of the particle mass and influence surface-controlled properties. The volume effect can be explained by the fact that the number of atoms composing a particle is insufficient for bulk properties to exist (Gleiter, 1989).

Among the various kinds of nanomaterials, titania (TiO_2) is a very interesting material that shows outstanding chemical stability, high refractive index, great ultraviolet absorptivity and photochemical activity. Because of those characteristics, titania particles have been used in many applications such as in paint as pigments, in waste-water treatment as photocatalysts (Yu et al., 2003), in separation processes as filters or membranes (Verweij, 1998), and in photovoltaic processes as components of solar cells (Barbe et al., 1997). The various production methods of nanopowders can be classified into three categories: chemically reactive gas phase synthesis (flame synthesis, oxidation

process, and pyrolysis or hydrolysis of organo-titanium compounds), wet chemistry process (sol-gel process), and physical vapor deposition (inert gas condensation and ion beam assisted deposition).

One laboratory-scale process for synthesizing metal nanoparticulate films is a hybrid process based upon chemical vapor deposition and gas-to-particle conversion (Nguyen et al., 2002). This process has the advantages of single-stage, atmospheric, solvent-free and low substrate temperature operation. Nanostructured films produced by this process are very porous and they could potentially be used as filters, catalysts, or sorption media. Those films are composed of agglomerate particles that are bonded with each other by the combination of van der Waals and chemical (covalent and ionic) interactions. However, the as-synthesized films are not mechanically strong enough to maintain the original structural form because agglomerates of particles in the film are held together by van der Waals forces as shown in Figure 1.1.

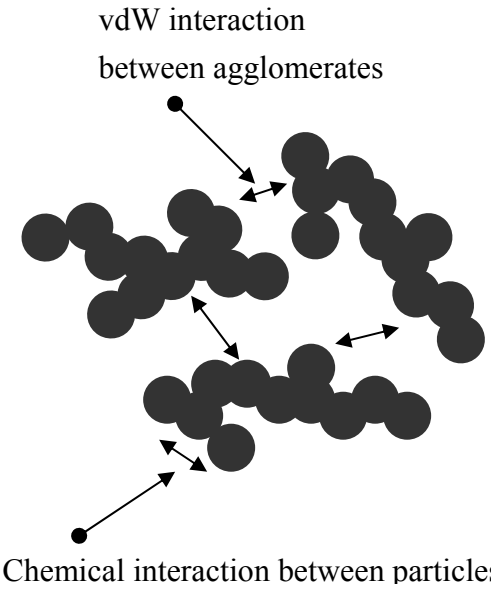

Figure 1.1 Typical structure of synthesized films by a hybrid process showing van der Waals interactions between agglomerates and chemical interactions between nanoparticles within agglomerates.

This disadvantage of the film makes its application limited and it is very difficult to use the film for commercial purposes. To avoid this problem, many different approaches have been attempted such as annealing, encapsulation to form composite nanoparticles, and coating with self-assembled monolayers. In particular, self-assembled monolayers have attracted increasing attention for their potential applications in optical and electronic devices (Wang et al., 1998). However, all the methods could change the surface properties of original nanoparticles by decreasing the surface area or by encapsulating the original surface with a different material.

In this dissertation, three different subjects are investigated: the development of a new process for forming an interconnection between titania nanoparticles based on capillary condensation and surface reaction, the understanding of capillary condensation phenomena at nanoscale dimensions, and the exploitation of surface modification of titania nanoparticles to enhance photocatalytic activity. These studies are performed by various methods including experiments, computer simulations, theoretical analyses based on macromolecular thermodynamics (geometrically specific Kelvin equation), and kinetic analyses of photocatalytic reaction rates. These combined studies are helpful to understand the characteristics of capillary condensation in the nanoscale regime and could be applicable for some nanoscale modification processes related to heterogeneous condensation.

This dissertation is outlined as follows. Chapter 2 contains basic physical background and reviews of the literature about capillary condensation based on macromolecular thermodynamics, Monte Carlo simulations based on statistical thermodynamics, and photocatalytic reactions in terms of kinetic analysis.

Chapter 3 describes details of the tubular laminar flow chamber design performed with the aid of a commercial computational fluid dynamics program. The chamber is designed for the study of capillary condensation in a controlled manner

because very accurate temperature and vapor pressure control is required to maintain the objective saturation condition around the sample.

In Chapter 4, by using this flow chamber, a new process is presented and used to produce various amounts of bridge-shaped layers on titania nanoparticles. The detailed experimental setup is described and the various analytical techniques (X-ray photoelectron spectroscopy, Fourier transform infrared spectroscopy, transmission electron microscopy, and electron energy-loss spectrometry) are used to characterize the modified nanoparticles. The comparison of TEM results and theoretical analysis based on the Kelvin equation suggests that this process is a useful method to modify the nanoparticles in a controlled way.

Chapter 5 presents the investigations of nanoscale capillary condensation phenomena using the grand canonical Monte Carlo (GCMC) simulation approach. For a system describing tetraethoxy orthosilicate condensation on titania particles shown in Chapter 3, this computational technique is used to exploit how the nanoscale geometries of the particles and the proximity of two solid surfaces as well as saturation conditions affect capillary condensation at the nanoscale. The details of simulation results and the comparison of these results to a theoretical analysis are also systematically discussed.

In Chapter 6, I apply this capillary condensation process for making interparticle connections between bi-phase (anatase and rutile) titania nanoparticles and investigate a photocatalytic activity of surface-modified samples towards photo degradation of methylene blue using an annular quartz photocatalytic reactor. The activity is estimated assuming the reaction can be described by pseudo 1st order reaction kinetics and the samples are characterized by various analytical techniques (TEM, BET, and XRD).

Finally, based on the results of this dissertation and the results of previous investigators, conclusions are given for the surface modification of titania nanoparticles by capillary condensation. In addition to the development of the process of capillary condensation, theoretical study based on grand canonical Monte Carlo simulations and the effect of capillary condensation on photocatalytic activity are also summarized. Suggestions for future research related to the application of this surface modification process for nanostructured materials are given with concluding remarks.

II. BACKGROUND

2.1 Capillary Condensation

Vapor usually condenses into liquid over a flat surface if the vapor pressure is higher than the saturation pressure. Here, saturation pressure is defined as the equilibrium vapor pressure over a flat surface. The term 'equilibrium vapor pressure' refers to the equilibrium vapor pressure over any surface regardless of curvature. However, at specific surfaces such as pores, slits, or gaps, vapor can condense at a lower pressure than the saturation pressure. This general relationship between geometric shape and the equilibrium vapor pressure can be explained on the basis of well-known thermodynamic models. The fundamental Kelvin-Laplace equation is widely applied to describe the mechanical equilibrium of capillarity.

$$\Delta P = P_{in} - P_{out} = \gamma\left(\frac{1}{R_1} + \frac{1}{R_2}\right) \tag{1}$$

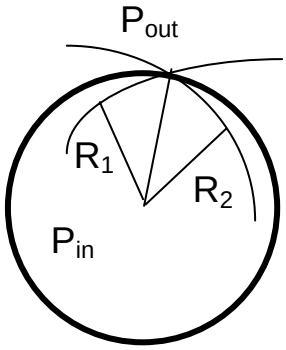

Figure 2.1 Schematic diagram showing variables in the Kelvin Equation.

Here, γ is the surface tension, ΔP is the difference in pressures due to the surface curvature, and R_1 and R_2 are two radii of curvature, as shown in Figure 2.1. Gibbs theory is also used to describe the relationship between the pressure of a curved surface and the pressure of saturated vapor. In case of simple spherical bodies, for which both radii of curvature are equal to the sphere radius (r), equation (1) has the following forms

$$\Delta P = \frac{2\gamma}{r} \tag{2}$$

and

$$RT \ln \frac{P}{P_s} = \frac{2\gamma V}{r} \tag{3}$$

where V is the volume per molecule, P_s is the saturation pressure at the specific temperature, and R is the gas constant (Adamson and Gast, 1997). The above equation (3) is called the Kelvin equation and it can predict the equilibrium radius of curvature for

a vapor-condensed liquid interface that results from capillary condensation. The Kelvin equation is very simple but has been shown to be valid for systems including water and organic solvents studied down to the meniscus radius 2-4 nm even though it is derived on the basis of macroscopic thermodynamics (Digilov, 2000) and the assumption that γ is constant with r.

There have been a lot of investigations of capillary condensation that are focused on condensation in pores and between atomic force microscope (AFM) tip and substrate surfaces. In these studies, the effect of the experimental conditions such as temperature, geometry, and the amount and stability of condensed liquid on specific surfaces was investigated. Recently, many groups have been interested in the phenomenon of capillary condensation between two solid bodies at nanocontacts because it plays an important role in scanning probe instruments and magnetic hard disk devices (Willett et al., 2000). In the dissertation, capillary condensation on the surface of nanoparticles is investigated by geometrical analysis in which the relationship between partial pressure and the radius of curvature of the liquid-fluid interface is derived in order to obtain the proper experimental conditions resulting in a specific coverage of liquid meniscus. In general, an equation describing the pressure difference across an interface is obtained by numerical integration over an arbitrary interface that may be written as follows:

$$\Delta P = \gamma(\frac{1}{r_1} + \frac{1}{r_2}) = \gamma\left[\frac{1}{r(1+\dot{r}^2)^{1/2}} - \frac{\ddot{r}}{(1+\dot{r}^2)^{3/2}}\right] \quad (4)$$

where r(x) is the meridional bridge profile, and r_1 and r_2 are local principal radii of normal curvature in orthogonal directions at points along the meridional bridge profile. The dot notation refers to differentiation with respect to x. Usually, the radius of curvature r_1 is within the liquid bridge and is positive in sign. r_2 is evaluated from the bridge profile and can be positive or negative depending on the pressure difference between the inside and outside. The effect of gravity is neglected in equation (4) because of the small amount of condensate. Some additional approximations are needed to solve for the pressure difference because the calculation of the exact shape of the liquid-vapor interface is rather tedious and requires complex numerical integration (Hotta et al., 1974). In Chapter 4, a relationship for the pressure difference is derived for the case of a meniscus at the contact point between nanoparticles based on the assumption that the meniscus is symmetric with respect to the y-axis and the capillary surface joining the particles forms circular contact lines. It was verified by previous study (Clark et al., 1968) that describing the cross-section of the liquid-vapor interface by a circle is a very good approximation.

2.2 Computer simulation

In recent years, the method of computer simulation has become an alternative to conventional techniques for the solution of physical and chemical problems because computer simulations can be used to obtain numerical results for systems of greater generality than those which have been successfully treated analytically. The statistical mechanics of even very simple models, such as the three-dimensional Ising model (Binder and Baumgärtner, 1984), cannot be solved exactly, and much less is known about models with realistic potentials between the atomic degrees of freedom. In this sense, computer simulations are often designed to check the accuracy of some approximation made in the analytical treatment of a model.

Computer simulation allows us to study properties of many body systems. However, not all properties can be directly measured in a simulation. Conversely, most of the quantities measured in a simulation do not correspond to properties in real experiments. The conversion of this very detailed information into macroscopic terms is the essence of statistical mechanics, which is reviewed shortly. The detailed explanations of statistical mechanics are available from various sources in the literature (Hill, 1986; Allen and Tildesley, 1987; Binder and Heermann, 1988).

In this thesis, a one component macroscopic system is considered for simplicity. The thermodynamic state of such a system is usually defined by a small set of parameters such as the number of molecules N, the temperature T, and the pressure P. Other thermodynamic properties may be derived through the equations of state and the fundamental equations of thermodynamics. The macroscopic properties are completely dictated by the few variables like NPT characterizing the thermodynamic state, not by many molecular spatial positions (r) and momenta (p) that specify the instantaneous mechanical state of N-body system. These coordinates of positions and momenta, along with the equations of motion of the system, can determine the future and past course of the system and a conceptual space of the coordinates can be thought of a phase space for the system under consideration.

The state of the classical N-body system at any time t is completely specified by the location of one point in phase space, which is called a phase point (Γ). As the system evolves in time, one can estimate its mechanical property in each phase point that is consistent with the specific thermodynamic state defined by a few parameters. The time average of this mechanical property over a long time corresponds to a parallel thermodynamic property. However, in practice, such a calculation of time averages for large numbers of molecules is complex and may not be the proper approach to

thermodynamic properties implicit in conventional statistical mechanics. Thus, Gibbs suggested replacing the time average by the ensemble average, which is a collection of a very large number of systems constructed to be a replica of a thermodynamic state specified by macroscopic parameters in the same phase space. The entire ensemble appears as a cloud of points in phase space and those points are distributed according to a probability density $\rho(\Gamma)$. This probability density function is determined by the ensemble defined by macroscopic parameters, so the notation of ρ_{ens} is generally used. If $\rho_{ens}(\Gamma)$ represents an equilibrium ensemble, its time dependency vanishes, which is based on ergodicity (Tolman, 1938). In that case, the time average can be replaced by the ensemble average taken over all possible states in equilibrium.

Generally, $\rho_{ens}(\Gamma)$ is defined by a weight function, which satisfies the following equations.

$$\rho_{ens}(\Gamma) = \frac{w_{ens}(\Gamma)}{Q_{ens}} \tag{5}$$

$$Q_{ens} = \sum_{\Gamma} w_{ens}(\Gamma) \tag{6}$$

The weight function is essentially a non-normalized form of $\rho_{ens}(\Gamma)$, with the partition function Q_{ens} (also called the sum over states) acting as the normalizing factor. The partition function serves as a bridge between the mechanical energy states of a macroscopic system and the thermodynamic properties of that system. If Q_{ens} is

obtained as a function of the macroscopic properties defining the ensemble, one can calculate a thermodynamic potential, Ψ_{ens}, in terms of mechanical and molecular parameters (McQuarrie, 1976).

$$\Psi_{ens} = -\ln Q_{ens} \tag{7}$$

This is the function that has a minimum value at thermodynamic equilibrium (e.g. the negative of the entropy S for a system at constant NVE and the Gibbs function G for a constant NPT system).

One possible approach to the computation of thermodynamic quantities is a direct evaluation of Q_{ens} for a particular ensemble. However, this summation over all possible states is not feasible for many-molecule systems. People would like to conduct the summation so as to exclude the large number of irrelevant states, and include only those with a high probability. Unfortunately, it is generally not possible to estimate Q_{ens} directly in this way. However, generating random numbers from the probability density $\rho_{ens}(\Gamma)$ allows function evaluation to be concentrated in the regions of space that make important contributions. This importance sampling is central to the Monte Carlo technique.

The cores of most molecular dynamics/Monte Carlo simulation programs are, if not identical, very similar. Here, some basic concepts and formulations of common

Monte Carlo simulations for typically used ensembles are briefly presented: the canonical (constant NVT) ensemble, isothermal-isobaric (constant NPT) ensemble, and the grand canonical (constant μVT) ensemble. General procedures to validate Monte Carlo algorithms (Frenkel and Smit, 2002) for various ensembles are as follows:

1. Choose the distribution of interest. This distribution, denoted $\rho_{ens,}$ will depend on the details of the ensemble.

2. Impose the condition of detailed balance from one configuration to another,

$$f(o \to n) = f(n \to o) \tag{8}$$

where f(o→n) is the flow of configuration o to n. This flow is given by the product of the probability of being in configuration o, ρ(o), the probability generating configuration n, α(o), and the probability of accepting this move, acc(o→n),

$$f(o \to n) = \rho(o) \times \alpha(o \to n) \times acc(o \to n). \tag{9}$$

Here, I denote the transition matrix that determines the probability of performing a trial move from o to n by α(o→n), where α is usually refereed to as the matrix of the Markov chain (Kampen, 1981).

3. Determine the probabilities of generating a particular configuration.

4. Derive the condition that needs to be fulfilled by the acceptance rules.

Each trial move is accepted with a probability of acc(o→n). In order to decide whether to accept or reject the trial move, a random number is generated from uniform distribution in the interval [0,1]. The trial move is accepted if the random number is smaller than acc(o→n) and rejected otherwise; a procedure is based on the Metropolis algorithm (Metropolis et al., 1953). This probability of acc(o→n) is defined below for various ensembles.

Canonical Ensemble

In the canonical ensemble, the number of molecules, temperature, and volume are constant. The density of the canonical ensemble is proportional to

$$\exp(-H(\Gamma)/kT) \tag{10}$$

where Γ represents the set of particle positions and momenta, and $H(\Gamma)$ is the Hamiltonian. The partition function is

$$Q_{NVT} = \sum_{\Gamma} \exp(-H(\Gamma)/kT) \tag{11}$$

or, in quasi-classical form, for an atomic system

$$Q_{NVT} = \frac{1}{N!}\frac{1}{h^{3N}} \int drdp \exp(-H(r,p)/kT). \tag{12}$$

The appropriate thermodynamic function is the Helmholtz free energy A

$$A/kT = -\ln Q_{NVT} \tag{132}$$

Based on the partition function and the density probability, a general Monte Carlo simulation can be formulated using the following scheme:

1. Choose a molecule at random and calculate the energy of this configuration

2. Let this molecule move with a random displacement

3. This move is accepted based on a probability

$$acc(o \to n) = \min[1, \exp(-\frac{(H(\Gamma_o) - H(\Gamma_n)}{kT}))] \tag{14}$$

where min represents a function to choose the minimum value because the probability acc(o→n) cannot exceed 1. If rejected, the old configuration is kept.

Isobaric-Isothermal Ensemble

The isobaric-isothermal ensemble is widely used in Monte Carlo simulations because most real experiments are carried out under conditions of controlled pressure and temperature. Moreover, this ensemble can be used to measure the equation of state of a model system even if the virial expression for the pressure cannot be obtained in an exact form. Finally, it is often convenient to use constant NPT Monte Carlo to simulate systems in the vicinity of a first-order phase transition, because at constant pressure the system is free to transform completely into the state of lowest free energy, whereas in a canonical ensemble simulation the system may undergo phase separation where two bulk phases of different density exist together.

The probability density for the isothermal-isobaric ensemble is proportional to

$$\exp(-(H+PV)/kT)\,. \tag{15}$$

Now the volume V has joined the list of microscopic quantities comprising the state Γ.

The appropriate partition function is

$$Q_{NPT}=\sum_{\Gamma}\sum_{V}\exp(-(H+PV)/kT)=\sum_{V}\exp(-PV/kT)Q_{NVT}\,. \tag{16}$$

The summation over possible volumes may also be written as an integral, in which case some basic unit of volume V_0 must be chosen to render Q_{NPT} dimensionless. In quasi-classical form, for an atomic system,

$$Q_{NPT}=\frac{1}{N!}\frac{1}{h^{3N}}\frac{1}{V_0}\int dV\int drdp\exp(-(H+PV)/kT)\,. \tag{17}$$

The corresponding thermodynamic function is the Gibbs free energy

$$G/kT=-\ln Q_{NPT}\,. \tag{18}$$

In the constant NPT Monte Carlo simulation, V is simply treated as an additional coordinate, and trial move in V must satisfy the same rules in addition to trial moves. If it is assumed that the trial moves consist of an attempted change of the volume from V to V', in the Metropolis scheme such a random, volume-changing move will be accepted with the probability

$$acc(o\to n)=\min[1,\exp(-\frac{(H(\Gamma_o)-H(\Gamma_n))-P(V'-V)}{kT}-N\ln(V'/V))]\,. \tag{19}$$

Grand-Canonical Ensemble

The ensembles discussed so far have kept the total number of molecules constant. However, for some systems, one would need information on the average number of molecules in a system as a function of the external conditions. In adsorption studies one would like to know the amount of material adsorbed as a function of the pressure and temperature of the reservoir with which the material is in contact. An appropriate ensemble for this typical gas adsorption problem is the grand-canonical ensemble. In this ensemble, the temperature, volume, and chemical potential are fixed. These constraints make this simulation different from conventional ensembles, where the total number of molecules is fixed.

The density function for the grand canonical ensemble is proportional to

$$\exp(-(H-\mu N)/kT) \tag{20}$$

where μ is the specified chemical potential. In this case, the number of molecules N is a variable, along with the coordinates and momenta of those molecules. The grand canonical partition function is

$$Q_{\mu VT} = \sum_{\Gamma} \sum_{N} \exp(-(H-\mu N)/kT) = \sum_{N} \exp(\mu N/kT) Q_{NVT} \,. \tag{21}$$

In quasi-classical form, for an atomic system,

$$Q_{\mu VT} = \sum_{N} \frac{1}{N!} \frac{1}{h^{3N}} \exp(\mu N/kT) \int dr dp \exp(-H/kT) \,. \tag{22}$$

Although it is occasionally useful to assume that N is a continuous variable, for most purposes it is summed, rather than integrated.

In grand-canonical simulation, the trial moves from state one to another can proceed in three possible steps: a molecule is added, a molecule is removed, or an existing molecule is moved. Each trial move is accepted based on the partition function and density probability as follows.

1. Displacement of molecules

A molecule is selected at random and given a new conformation. This move is accepted with a probability same as the case of the canonical ensemble.

2. Insertion and removal of molecules

A molecule is inserted at a random position or a randomly selected molecule is removed. The creation of molecule is accepted with a probability

$$acc(N \to N+1) = \min[1, \frac{V}{\Lambda^3 (N+1)} \exp(\frac{(\mu - H(\Gamma, N+1) + H(\Gamma, N))}{kT})] \qquad (23)$$

and the removal of a molecule is accepted with a probability

$$acc(N \to N-1) = \min[1, \frac{\Lambda^3 N}{V} \exp(-\frac{(\mu + H(\Gamma, N-1) - H(\Gamma, N))}{kT})] \qquad (24)$$

Grand-canonical Monte Carlo (GCMC) simulations are more complicated to program than those in the canonical ensemble because the molecule creation and destruction must be considered with the molecule displacement in a reasonable way.

However, it can provide a direct route to the statistical properties of the system. For example, by determining the free energy of two different solid structures in two independent GCMC simulations, it is possible to identify which of the two structures is thermodynamically stable at a particular μ and T. GCMC simulations are also useful for studying inhomogeneous systems such as monolayer or multilayer adsorption near a surface. In these systems, the surface often interacts with the molecules with attractive or repulsive force so that the molecules near the surface undergo a different phase transition from the bulk. Thus, the adsorption and evaporation phenomena in cylindrical or slitlike pores or even irregular porous media have been investigated using GCMC simulation because of numerous theoretical and experimental interests for gas-fluid condensation transition. Effects of geometrical size and molecule-surface interaction were studied varying chemical potential and temperature to understand unusual phase transition behavior in such finite geometries (Bohlen and Schoen, 2005; Gatica and Cole, 2005; Kuchta and Firlej, 2005). Chemically or geometrically structured pores were also extensively considered to obtain a better comparison between theory and experiments for capillary phenomena in real pores (Puibasset, 2005; Hemming and Patey, 2006). For these reasons, the grand canonical ensemble was chosen for the Monte Carlo simulations reported in Chapter 5.

2.3 Photocatalytic activity of semiconductor particles

Considerable interest has been shown recently in the use of semiconductor particles as photocatalysts in the degradation of harmful organic contaminants. The initial discovery of photo-assisted electrolysis at the surface of TiO_2 single crystals led to many important developments in the area of photo-electrochemistry (Fujishim.A and Honda, 1972). The importance of photocatalysis lies in the fact that it can provide a potentially inexpensive and convenient way of treating organic contaminants.

Photocatalytic reactions occur when the semiconductor particle absorbs a photon of light more energetic than its bandgap. Under bandgap excitation semiconductor particles act as short-circuited microelectrodes and initiate oxidation and reduction processes of adsorbed substrates. When a photon with energy of *hv* matches or exceeds the bandgap energy of semiconductor, an electron is excited from the valence band to the conduction band, leaving a hole in the valence band (Figure 2.2). Excited state conduction band electrons and valence band holes can recombine and dissipate the input energy as heat, get trapped at the surface vacancies, or participate in redox reactions. The trapped electrons and trapped holes can also participate in the interfacial charge transfer process. Most organic photodegradation reactions utilize the oxidizing power of the

holes either directly or indirectly; however, to prevent a buildup of charge one must also provide a reducible species to react with the electrons.

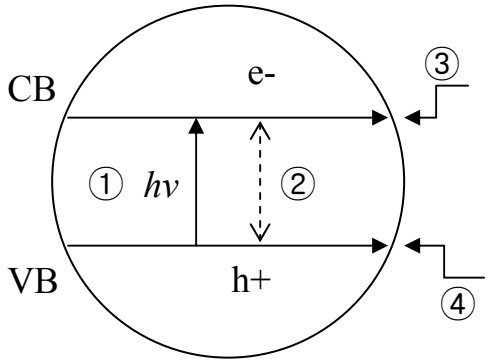

Figure 2.2 Primary steps in the photoelectrochemical mechanism: 1) formation of charge carriers by a photon, 2) charge carrier recombination, 3) initiation of a reductive pathway by a conduction band (CB) electron, and 4) initiation of an oxidative pathway by a valence ban (VB) hole.

Semiconductor photocatalysis, with a primary focus on TiO_2 as a durable photocatalyst, has been applied to a variety of problems of environmental interest in addition to water and air purification. It has been shown to be useful for the destruction of microorganisms (Ireland et al., 1993), for the inactivation of cancer cells (Cai et al., 1992; Cai et al., 1992), and for odor control (Sato et al., 1992).

Several simple oxide and sulfide semiconductors have bandgap energies sufficient for promoting or catalyzing a wide range of chemical reactions of environmental interest. However, among these semiconductors TiO_2 has proven to be the most suitable for widespread environmental applications because it is biologically and chemically inert; it is stable with respect to photo and chemical corrosion; and it is inexpensive. ZnO appears to be a suitable alternative to TiO_2 but it is unstable with respect to incongruous dissolution, forming $Zn(OH)_2$ on the particle surfaces which leads to catalyst deactivation over time.

The photocatalytic activities of two forms of TiO_2, anatase and rutile, is significantly different, with the former being a much more active catalyst. Rutile and anatase have similar crystal structures, which are both tetragonal. Rutile is the thermodynamically stable form to which anatase and brookite (an orthorhombic phase of TiO_2) convert when heated over 600 °C. The difference in the photocatalytic activities of both tetragonal phases may be due to differences in lattice structure. In addition to the differences in the optical and semiconductor properties, surface properties help account for the differences in photocatalytic activities. A study of the charge-carrier dynamics has shown that anatase TiO_2 exhibits higher yields and longer lifetimes for photo-induced charge carriers, and that surface modification changes the behavior

considerably (Schindler and Kunst, 1990). Studies have been made of the acidic and basic properties of anatase, and it has been found that surface properties affect adsorption significantly (Boehm, 1971). Surface properties have been related to the adsorption of oxygen, which may affect photoactivity (Boonstra and Mutsaers, 1975).

Heterogeneous electron transfer at the semiconductor-solution interface is greatly influenced by parameters such as the surface charge, site specific interactions and adsorption, and energetic of the semiconductor and substrate. These parameters can be controlled by varying the composition and reaction parameters of the medium in which TiO_2 particles are suspended. Among these parameters, the following parameters have been shown experimentally to have the most significant effects: pH, oxygen concentration, and light intensity. Varying pH not only shifts the band energies of the metal oxide semiconductor, but also varies the surface charge. Most of the examinations of the effect of pH on the initial degradation rate have found that the relationship between the degradation rate and pH was relatively constant in neutral and weakly acidic conditions except strong acid and basic conditions. In the strong acid and basic conditions, the effect of pH is varied in each system. However, the effect of pH on the degradation rates of some chemicals was relatively small (Alekabi and Demayo, 1986; Carraway et al., 1994). Oxygen concentration is also crucial to photocatalytic oxidation

carried out in slurries and no degradation occurs without oxygen or some other oxidant. Scavenging by O_2 can be rate limiting in the photocatalytic oxidation process. The relationship of oxygen concentration to degradation rates follows Langmuir-Hinshelwood (LH) kinetics, and maximum degradation rates are approached at around saturation at 0.5-1 atm oxygen partial pressure (Augugliaro et al., 1988). The effect of light intensity has been widely reported that at lower light intensities the rate of degradation is proportional to the light intensity and at higher incident light intensities the degradation rate is proportional to the square root of the light intensity (Kormann et al., 1991; Cunningham and Sedlak, 1994). The reason for the square root relationship has been explained by bulk recombination of holes and electrons within the catalyst particles (Okamoto et al., 1985).

Numerous researchers have reported that the rates of photodegradation of chemical compounds on semiconductor surfaces follow the classical Langmuir-Hinshelwood expression and that the adsorption to the semiconductor surfaces most often follows Langmuir adsorption isotherms (Jenny and Pichat, 1991; Zafra et al., 1991; Matthews and Mcevoy, 1992; Milis et al., 1994). This model assumes that at equilibrium, the number of surface adsorption sites is fixed; only one molecule may bind at each surface site; the heat of adsorption by the molecule is identical for each site and is

independent of surface coverage; there is no interaction between adjacent adsorbed molecules; the rate of surface adsorption of the molecule is greater than the rate of any subsequent chemical reactions; and no irreversible blocking of active sites by binding to product occurs (Hinshelwood, 1926). The rate of reaction can be written as a single component kinetic rate expression

$$r = -\frac{dC}{dt} = \frac{kKC}{1+KC} \tag{25}$$

where k and K are the adsorption rate and adsorption equilibrium constants respectively. The linearity of a plot of 1/r versus 1/C tests the validity of the LH model, where 1/k is the y intercept and 1/kK is the slope. In most of photocatalytic reactions, such expression is adequate to explain the basic initial kinetics of disappearance of the target reactant for the individual system. For low concentrations of reactant, the equation (25) can be simplified to

$$r = -\frac{dC}{dt} = k'C \ . \tag{26}$$

Thus, this pseudo 1st order kinetics was used to analyze the photocatalytic activity of titania nanoparticles in Chapter 6.

III. FLOW CHAMBER DESIGN

3.1 Abstract

To study capillary condensation in a controlled manner, very accurate temperature and vapor pressure control around the sample is required to maintain the specific saturation ratio. In this study, a tubular laminar flow chamber with a small radius was employed to minimize the temperature variance along the radial direction and to obtain a large region with constant saturation ratio. The applicability of this chamber was verified using a computational fluid dynamics program and some experimental conditions such as the chamber temperature and sample holder location were decided on the basis of the computational analysis.

3.2 Introduction

A tubular laminar flow chamber was designed to achieve a specific supersaturation state similar to laminar flow diffusion chambers used for nucleation studies (Hameri et al., 1996). Nucleation phenomena are important in global climatic conditions as well as air pollution formation, and materials processing, so there have been a number of experimental studies of the nucleation rate of several systems. The most commonly used devices include adiabatic expansion chambers (Strey et al., 1986), turbulent mixing flow chambers (Kreidenweis et al., 1989), thermal diffusion chambers (Katz, 1970), and laminar flow diffusion chambers (Vohra and Heist, 1996). Among those, the laminar flow chamber was selected as the basic design model because of following advantages. It can be operated at atmospheric pressure and does not need complex pressure control equipment. Various samples can be tested without complex start-up procedures. The difference in radial temperature is sufficiently small so as to maintain stable supersaturation around the sample.

3.3 Flow chamber design

In a laminar flow chamber, simultaneous convection, heat conduction, and vapor diffusion generally result in vapor concentration profiles. If the walls of the chamber are heated, most of condensation occurs at the center of flow where the saturation ratio is the highest. Similar working principles are applied to the flow chamber design. The laminar flow is initially saturated, and is cooled or heated by changing the wall temperature. The heat adjustment leads to supersaturation or undersaturation, and consequently heterogeneous condensation of vapor inside the chamber onto particles immobilized on a flat surface. In the design of the laminar flow chamber system, some assumptions were made before the dimensions and flow rate were chosen (Bird et al., 2002).

1) The density is assumed to be constant because temperature variation inside the chamber is not large. The flow is considered as incompressible flow.

2) The fluid is Newtonian and behaves as a continuum.

3) The flow is in steady state.

Additionally, the flow rate was adjusted to satisfy the condition for laminar flow that the Reynolds number ($Re = \rho v d / \eta$) is less than about 2100. Here, ρ is the density of the fluid, v is the average flow velocity, d is the diameter of the tube, and η is the velocity of the fluid. The length of the flow chamber was chosen in order to allow buildup of the parabolic profiles. The necessary entrance length (l_e) on the order of $0.035dRe$ should be much smaller than the total length (Perry et al., 1997). In a real system, the entrance length of 6.0 cm is much smaller than the chamber length of 10.2 cm.

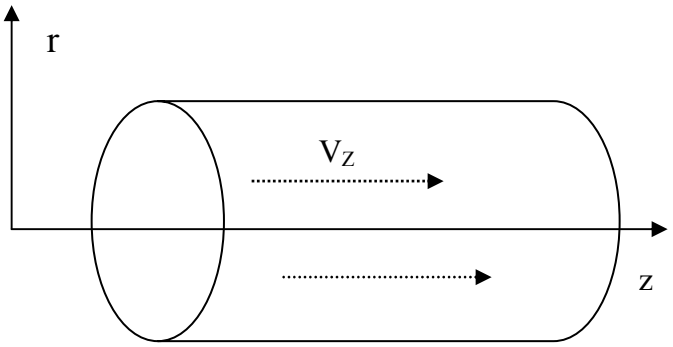

Figure 3.1 Cylindrical coordinates inside the flow chamber.

The flow chamber is a cylindrical tube that is connected the vapor supplier, a bubbler. Energy and mass transfer processes in the chamber can be described by the differential equations for a cylindrical tube of circular cross section as shown in Figure 3.1.

$$\frac{\partial}{\partial z}(\rho C_p v_z T) = \frac{1}{r}\frac{\partial}{\partial r}(kr\frac{\partial T}{\partial r}) + \frac{\partial}{\partial z}(k\frac{\partial T}{\partial z}) \quad (1)$$

$$\frac{\partial}{\partial z}(v_z C) = \frac{1}{r}\frac{\partial}{\partial r}(rD\frac{\partial C}{\partial r}) + \frac{\partial}{\partial z}(D\frac{\partial C}{\partial z}) \quad (2)$$

In equations (1) and (2), ρ and C_p are the mixture density and heat capacity, respectively. V_z is the axial component of the flow velocity, T is the mixture temperature, k is the mixture thermal conductivity, r is the chamber radius, z is the axial dimension, C is the vapor concentration, and D is the binary diffusion coefficient. Some assumptions can be used to simplify the original differential equations as stated above. The fluid is considered as viscous, incompressible, and Newtonian with constant properties. The fluid enters the chamber with a uniform temperature and it is heated or cooled through the wall whose temperature is maintained uniform. If viscous dissipation, internal heat generation, and axial heat conduction are neglected, the problem results in the classical Graetz problem. As a result of these assumptions, equation (1) and (2) reduce to

$$v_{max}[1-(\frac{r}{R})^2]\frac{\partial T}{\partial z} = \alpha\frac{1}{r}\frac{\partial}{\partial r}(r\frac{\partial T}{\partial r}) \quad (3)$$

$$v_{max}[1-(\frac{r}{R})^2]\frac{\partial C}{\partial z} = D\frac{1}{r}\frac{\partial}{\partial r}(r\frac{\partial T}{\partial r}) \quad (4)$$

Here, V_{max} is the maximum flow velocity, R is the chamber radius, and $\alpha = k / C_p\rho$ is the thermal diffusivity of the carrier gas and vapor mixture. The classical Graetz problem has been discussed in detail in many reports in the literature, and numerical solutions were obtained for many cases (Brown, 1960; Conley et al., 1985). In this study, a fluid

dynamics computational program, FLUENT, was applied to obtain solutions of the above differential equations instead of the numerical solution of the classical Graetz problem because FLUENT is applicable for the complex geometry of the chamber used in the real experimental setup and it can be used to obtain the concentration profile inside the chamber for different boundary conditions. The main objective is to verify that the saturation ratio is uniform at the location of the particle sample. The typical boundary conditions used in the analysis are the following,

$$T(r,0) = T_e \tag{5}$$

$$T(r, z=Z) = T_{Atmosph} \tag{6}$$

$$T(r, 0<z<m) = T_{wall,1}\ ,\ T(r, m<z<Z) = T_{wall,2} \tag{7}$$

$$\frac{\partial}{\partial r} C(r=R, z) = 0 \tag{8}$$

where T_e is the temperature of bubbler, $T_{wall,1}$ is the wall temperature of pre-heating zone, $T_{wall,2}$ is the wall temperature of the chamber, and $T_{atmosphere}$ is the temperature of outer medium.

For the real flow chamber composed of a cylindrical tube and an expansion section, the typical experimental conditions were applied: inlet temperature, T_e, is 81.1°C, $T_{atmosphere}$ is 25 °C, $T_{wall,1}$ is 91.1 °C, $T_{wall,2}$ is 81.1 °C and radius of the chamber is 1.9 cm.

In case the flow rate is 100 cc/min, the Re varies from 15 to 50 and the entrance length is 1 cm. The fluid in the system is a mixture of TEOS and argon, so all the properties in the differential equation were considered as mixtures. Argon properties can be easily found in the literature, but some thermodynamic properties of TEOS are not available such as viscosity, heat capacity, and thermal conductivity. For that reason, the TEOS thermodynamic properties including critical properties were estimated on the basis of the approximate correlation methods (Perry et al., 1997) (Appendix A). The estimations are given in Table 3.1. The mixture properties were also evaluated from the pure properties using the simple mixing rules developed by Twu and Coon (Twu and Coon, 1996).

Table 3.1 Various properties of TEOS and argon from literature (Perry et al., 1997).

	Argon	TEOS
Molecular Weight	39.94	208.33
Boiling Temperature (°C)	-185.7	168
Critical Temperature (K)	151	679*
Critical Pressure (atm)	48	93*
Viscosity (poise)	0.000258	0.000181*
Heat Capacity (J/mol/K) at 300 K	20.79	251.18*
Thermal Conductivity (cal/cm/sec/K)	0.000071	0.000054*

* calculated value based on the correlation model.

The temperature profile and saturation ratio (P/P_e) profile of the flow chamber were calculated numerically using FLUENT. The results in Figure 3.2 and Figure 3.3 showed how temperature and saturation ratio vary inside the chamber.

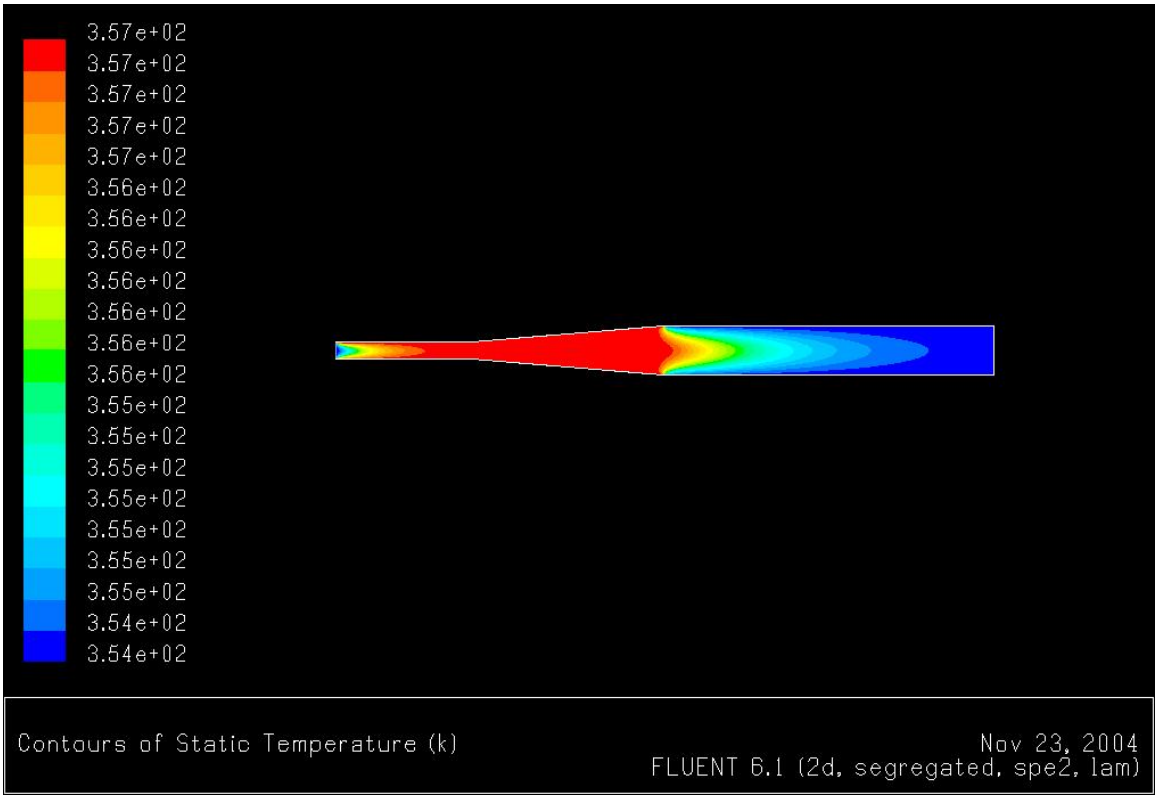

Figure 3.2 Temperature profile in the chamber (unit: K).

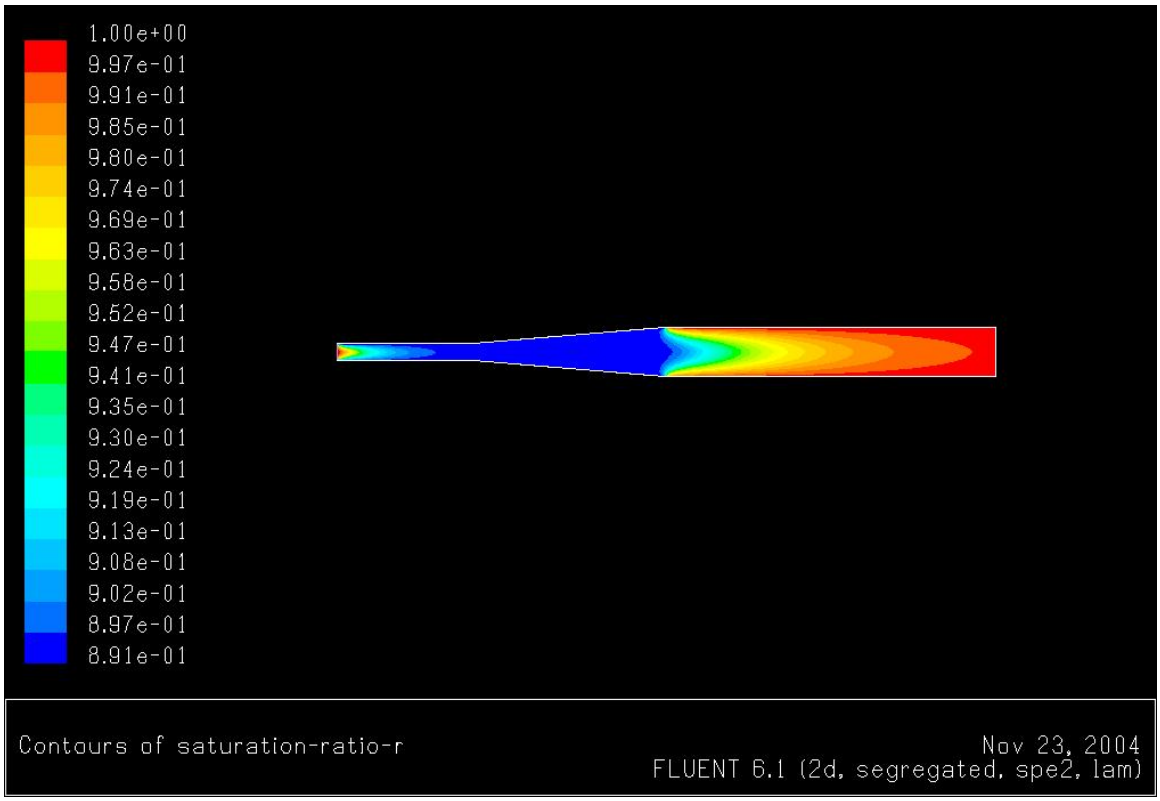

Figure 3.3 Saturation ratio profile in the cylindrical tube chamber.

The results in Figure 3.3 showed that there is a large region with constant saturation ratio near the end of the chamber and the region is sufficiently broad along the radial direction so as to obtain a uniform saturation ratio. If the sample with a sample holder is located in this region with a uniform saturation ratio, the constant saturation ratio around the sample can be controlled. The sample holder is believed to cause very little effect on saturation profile around the sample due to low Reynolds number ($Re \approx 15$). Thus, stable experimental conditions for capillary condensation can be achieved by adjusting process variables such as wall temperature, flow rate, chamber length, and inlet temperature. On the basis of the numerical simulations shown in Figure 3.3, the detailed diagram of the flow tube chamber was given in Figure 3.4 and experimental conditions were verified to obtain capillary condensation on the nanoparticle samples.

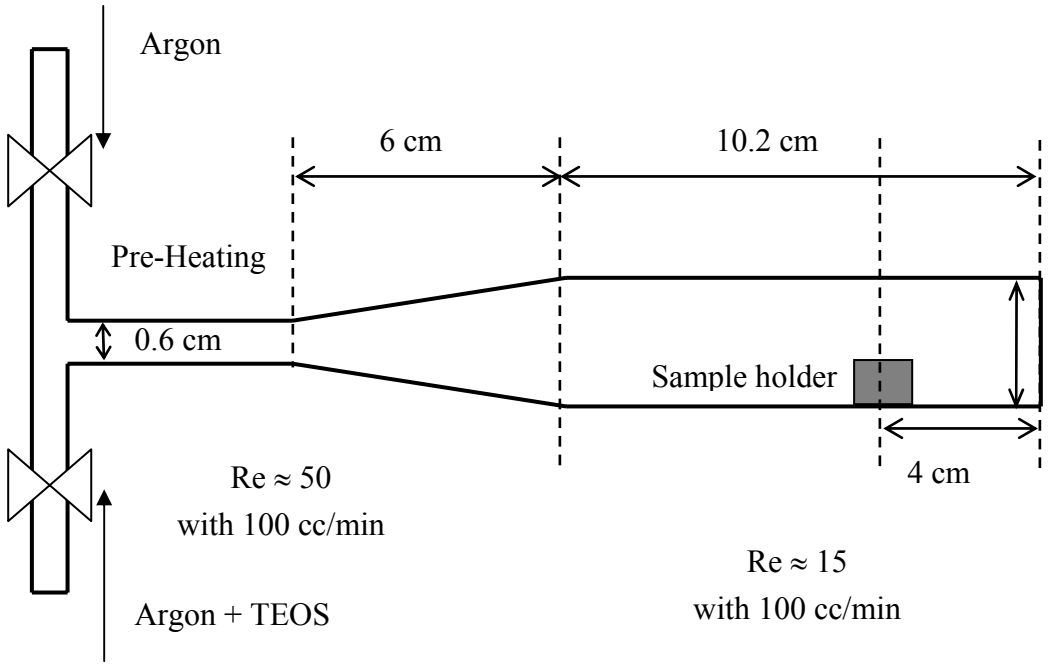

Figure 3.4 Flow tubular chamber diagram.

IV. CAPILLARY CONDENSATION ONTO TITANIA (TiO_2) NANOPARTICLE AGGLOMERATES

4.1 Abstract

A capillary condensation process was developed for the purpose of forming interconnections between nanoparticles at low temperatures. The process was performed in a temperature-controlled flow chamber on nanoparticle agglomerates deposited at sub-monolayer coverage on a transmission electron microscope grid. The partial pressure of the condensing species and the temperature of the chamber were adjusted in order to obtain the various saturation conditions for capillary condensation. The modified samples were analyzed by transmission electron microscopy, X-ray photoelectron spectroscopy, Fourier transform infrared spectroscopy, and scanning transmission electron microscopy with electron energy-loss spectrometry. Experimental results show that the bridge-shaped layers were dominantly formed in the neck region between particles, and were composed of amorphous silica. The analysis of TEM micrographs verified that the coverage of the layers is strongly dependent on the saturation ratio. Image analysis of TEM micrographs shows that this dependency is

qualitatively in agreement with theoretical predictions based on the classical Kelvin equation for the specific geometries in this system.

4.2 Introduction

Among the various kinds of nanomaterials, titania (TiO_2) is a very interesting material that shows outstanding chemical stability, high refractive index, great ultraviolet absorptivity and photochemical activity. Because of those characteristics, titania particles have been used in many applications such as in paint as pigments, in waste-water treatment as photocatalysts (Yu et al., 2003), in separation processes as filters or membranes (Verweij, 1998), and in photovoltaic processes as components of solar cells (Barbe et al., 1997). Recently, various techniques to design, fabricate, and manipulate nanostructured materials have been developed in order to achieve specific physicochemical characteristics for advanced applications. These techniques include heat treatment for structural development (Porter et al., 1999; Xia et al., 1999; Zhang et al., 2004), deposition of an additional component (Bell, 2003; Zhang et al., 2004), and coating of thin films (Brandriss and Margel, 1993; Wang et al., 1998). Among these techniques, self-assembled monolayer coatings have been extensively investigated for various nanoparticles due to their versatility and applied to synthesize core-shell particles

or hollow shell templates (Imhof, 2001; Wang and Caruso, 2002). The above methods have advantages and disadvantages. Generally, they result in a decrease of surface area, or a change of surface functionality of original nanoparticles, or both.

Recently our group has developed a hybrid process for synthesizing metal oxide nanoparticulate films based on gas-to-particle conversion and thermophoretic deposition (Nguyen et al., 2002). Nanostructured films produced by this process are porous and could potentially be used as filters, catalysts, or sorption media. However, the as-synthesized films have poor mechanical strength because the films are mainly composed of agglomerate particles bonded to each other by physical interactions. This disadvantage limits application of the films in commercial use and thus approaches for the enhancement of nanostructured films were considered.

The approach in this study is based on capillary condensation. Nanoscale capillary condensation is an important issue in fine powder engineering and, recently, various capillary characteristics at atomic force microscope (AFM) tips have been explored via experiments (Kohonen et al., 1999; Maeda and Christenson, 1999), theoretical developments (Marmur, 1993; de Lazzer et al., 1999), and computer simulations (Jang et al., 2002). Here, a new process was presented for forming silica interconnections between titania nanoparticles based on capillary condensation. Unlike

traditional coating methods for particles, which are usually performed in aqueous and/or organic solutions and result in a uniform coating on the entire surface, the proposed process was designed to produce a bridge-shaped layer in the contact zone between the particles. Unlike sintering which results in the formation or thickening of necks between particles, the process requires temperatures only slightly above room temperature. The process is based on condensation and surface reaction of a precursor, and the thickness of the layer depends on saturation conditions and the nature of particle surface and the precursor. Results are compared to predictions of layer thickness made using the Kelvin equation. This selective coating technique has potential use as a simple route to modify or enhance the properties of nanostructured materials, for an example mechanical strength, while minimizing loss of original surface area. Silica was chosen as coating material because it is easily observable in micrographs for comparison to theoretical predictions, but the approach in this study should be applicable to other material systems.

4.3 Experimental sections

Process design

Titania nanoparticle agglomerates were subjected to capillary condensation in a temperature-controlled flow chamber. The experimental setup consists of three components: glass bubbler and temperature bath for the vaporization of precursor, connecting lines for vapor transfer, and a chamber for capillary condensation. A schematic diagram of the process is given in Figure 4.1. The flow chamber is composed of three zones: preheating line, enlarging section, and main chamber. The preheating line is a 0.6 cm diameter tube. The enlarging section is a conical shape that connects the preheating zone with the main chamber, and the main chamber is a 1.9 cm inner diameter tube. All parts are made from brass to increase heat conductivity and are welded smoothly. The nanoparticles, which were placed onto a 3 mm diameter copper transmission electron microscope grid coated with formvar and carbon (Prod. No. 01813, Ted Pella Inc.), were exposed to precursor vapor in the chamber under uniform saturation conditions around the sample. Commercial titania nanoparticles (Tal Material Inc.) were used as the original sample. The number average diameter is 147 nm, estimated from the Brunauer-Emmett-Teller surface area measurement at 77 K using liquid nitrogen.

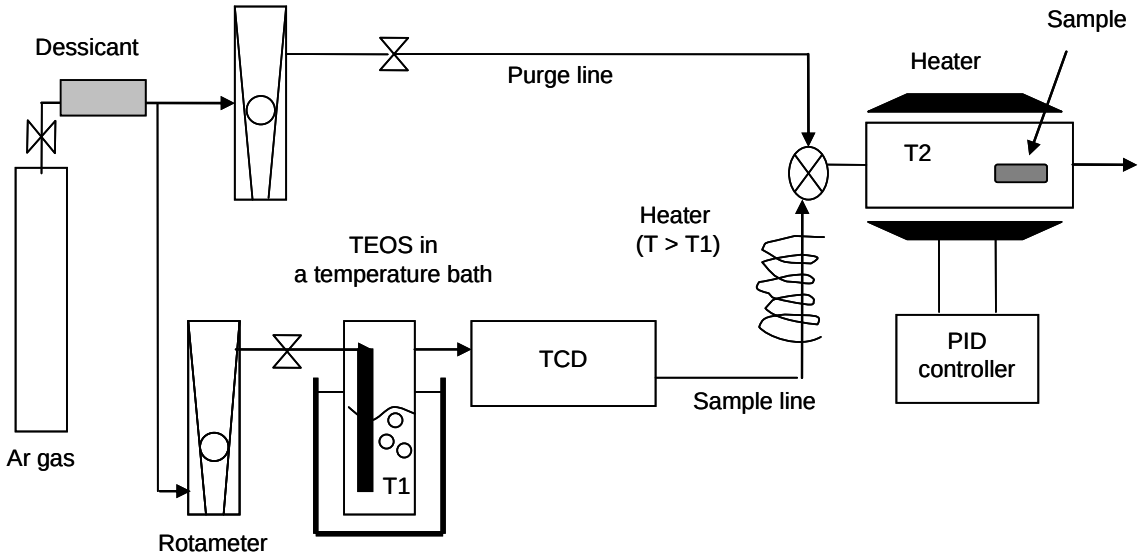

Figure 4.1 Schematic of the capillary condensation process.

Liquid tetraethyl orthosilicate (TEOS, $Si(OC_2H_5)_4$, 98+%; Sigma-Aldrich) was used as the precursor for silica coating. Generally, alkoxisilanes have been used as gaseous precursors for the growth of silicon dioxide layers because of high growth rate and conformal step coverage. In this study, TEOS was selected as the precursor for the formation of the silicon dioxide layer, because it is less toxic than other alkoxisilanes and is known to hydrolyze into silicon dioxide and ethanol in contact with ambient moisture. TEOS was vaporized in a glass bubbler (glass frit porosity of 145-175 μm, Ace Glass) by high purity argon carrier gas (99.9%), which was immerged in heating bath at a temperature of 81 °C. All the lines for TEOS vapor transfer and the headspace of the glass bubbler were wrapped with heating tape (SRT series, Omega; fiber glass heating cords, Cole Parmer Instruments), and covered by insulation tape (ZETEX, VWR Scientific) in order to minimize any loss of vapor by condensation onto the walls. The chamber was also wrapped by heating tape and its temperature was maintained by a proportional-integral-derivative (PID) controller (CNi1624-C24, Omega) in the range from 68 to 80 °C for the objective saturation condition. The sample was placed on a sample holder located inside the chamber. This chamber was designed based on similar chambers used in homogeneous nucleation rate studies (Anisimov et al., 1994; Hameri et al., 1996) and modified in order to obtain a uniform saturation conditions in the region

of the sample. The objective saturation condition was achieved by controlling the TEOS liquid temperature, the chamber temperature, and the carrier gas flow rate. A thermal conductivity detector (TCD, GOW-MAC Inc.), installed between the bubbler and the chamber, was used to quantitatively monitor the amount of TEOS vapor in real time.

Capillary condensation onto titania nanoparticles was performed in the following manner. Titania nanoparticles were loaded on a transmission electron microscope grid by dipping the grid into the powder reservoir and tapping the grid lightly to remove the excess. Particles stuck to the grid by electrostatic force and were well dispersed on the grid with sub-monolayer coverage. The TEM grid was placed in the sample holder and firmly fixed in the chamber. The chamber and connecting lines were first preheated for approximately 2 hours at a temperature at least 10 ºC higher than the objective temperature and purged with pure argon gas to remove any nucleation seed source such as dust, particles, and remaining chemicals. The chamber temperature was continuously maintained at the objective temperature for the desired saturation condition until the TCD baseline was stabilized. After the bubbler temperature and the chamber temperature were stabilized within ± 0.2 ºC, TEOS vapor was fed to the chamber at a rate ranging from 40 to 60 cc/min. The vaporized amount of liquid precursor was obtained by weighing the liquid mass in the bubbler before and after each experiment. The

saturation ratio around the sample was maintained through control of the precursor vapor pressure and the chamber temperature. The actual saturation ratio was obtained by correlating total amount of vaporized precursor with the continuous TCD measurement of the amount of the precursor in the flow. The introduced TEOS vapor condensed and formed meniscuses on the particles. The TEOS vapor was continuously supplied for 2 hours and the condensate was assumed to be in equilibrium with the vapor. Because the particles were placed on the TEM grid at sub-monolayer coverage, it is assumed that there are no significant mass transfer limitations. After 2 hours, the particle sample was exposed to the atmosphere overnight, allowing reaction of TEOS with ambient water vapor.

The adsorption and reaction of TEOS on the surface of titania has been investigated by others (Jin and White, 1988; Jurgens and Rogers, 1995) and the mechanism is thought to consist of condensation, concurrent hydrolysis, and rearrangement reactions in previous literature (Brinker, 1988). In this experiment, it is assumed that TEOS vapor first condenses on the titania surface and the condensate forms the equilibrium meniscus. The equilibrium meniscus is believed to hydrolyze slowly, reacting into amorphous silica once the sample is exposed to ambient humidity at room temperature. The typical density of amorphous silica, formed by flame reaction of

silicon tetrachloride for example, is much higher than that of TEOS (Perry et al., 1997), 2.2 g/cm^3 vs. 0.9 g/cm^3 and thus, one might expect the volume of the meniscus to shrink once TEOS reacts to silicon hydroxide then silica. However, according to a previous report (Yu et al., 2003) describing silica film formation from TEOS via sol-gel reaction, the film structure is significantly dependent on the rate of condensation reaction, which is governed by the type of catalysis. If the rate is low, the film seems to be sufficiently cross-linked so as to form a dense gel structure that is less porous (Yu et al., 2003). The density of silica layer with this type of gel structure is generally less than that of amorphous silica. In this work, no catalyst is used to promote condensation reaction, and thus condensation reactions are expected to be particularly slow, resulting in a gel-like structure with density comparable to TEOS. This suggests that the volume change associated with the reaction of the initial TEOS meniscus to the silica layer is not likely to be significant in this system.

Contact angle measurement

A contact angle measurement is of fundamental importance in all solid-liquid-fluid interfacial phenomena such as wetting of solid surfaces and capillary penetration into porous media. For the theoretical analysis of capillary condensation by the Kelvin equation, accurate measurement and correct interpretation of the contact angle is crucial.

In general, the wettability of the specific metal oxide surfaces is not well understood and experimental results in the literature are limited. Measurement of the contact angle between TEOS and titania was performed on a flat square surface. The measurement is based on a procedure previously reported for the wettability of transition metal oxide surfaces (Feng et al., 1998). For the contact angle measurement, a pure titanium plate (99.7 %, 10 cm X 10 cm, Alfa Aesar) was prepared by first polishing with abrasive films (diamond 0.8 μm, aluminum oxide 0.3 μm, and aluminum oxide 0.05 μm; South Bay Technology Inc.) for 10 minutes each. The polished surfaces were washed with acetone and methanol to remove polishing contaminants and other residual materials before the oxidation step. The smoothness of the polished surface was measured using a profilometer (Alpha-step 500, KLA-Tencor) and the average difference between the highest and lowest point was found to be less than 0.1 μm. A titania layer was formed on the polished metal surfaces by heating with air in a furnace at a temperature of 450 °C for 2 hours. The presence of a layer of titania was conformed by XPS measurement.

Contact angle measurements were made in air using the sessile-drop method. The drop images were captured by a CCD camera. If the geometry of the drop is spherical, the contact angle θc can be evaluated directly from the image by the following formula

$$\theta_c = \sin^{-1}\left(\frac{hd}{h^2 + d^2/4}\right) \quad (1)$$

where h is the height of the drop and d is the diameter of the contact circle. In this measurement, the contact angle of a water drop on the surface of the titania plate was measured in advance and the measured contact angle of 60° compared favorably with the result of 63° reported previously in the literature (Feng et al., 1998). For case of TEOS, the liquid drop spread out on the plate, with the TEOS liquid completely wetting titania surface, giving a contact angle of 0°.

Characterization techniques

Sample characterization was performed using the following methods: surface area analyzer (Quantachrome Instruments, Nova 1200), transmission electron microscopy (TEM, Hitachi H600 and Jeol 4000FX), X-ray photoelectron spectroscopy (XPS, Kratos Axis 165), Fourier transform infrared (FTIR, Nicolet 550 series) spectroscopy, and scanning transmission electron microscopy (STEM, JEOL 3000F) combined with electron energy-loss spectrometry (EELS). The main characteristics of the modified nanoparticles (size and morphology of particles, and formation of the layer on the particle surface) were observed by Hitachi TEM with an accelerating voltage of 100 kV. The Brunauer-Emmett-Teller (BET) surface areas of samples were measured to monitor the change in the surface area caused by the layer formation. The compositions of the

treated samples were verified through XPS and FTIR spectroscopy. The samples for FTIR spectra were mixed with KBr at a mass ratio of 1:3 and pressed into pellets. High resolution TEM (HRTEM) and STEM combined with EELS were used to analyze the structure and composition of the condensed layer on the titania surface.

4.4 Theoretical background

Capillary condensation phenomenon can be generally described by the Kelvin equation (Adamson, 1990), and the equilibrium vapor pressure over the curved surface can be formulated as a function of saturation vapor pressure and surface geometry as given by

$$R_g T \ln \frac{P}{P_s} = \kappa \gamma V = V \Delta P \tag{2}$$

where V is the volume per molecule, P_s is the saturation pressure at the specific temperature, ΔP is the difference in pressure due to the surface curvature, γ is the surface tension, κ is the sum of the two principal curvatures, and R_g is the gas constant. For the case of capillary condensation between two spherical particles as illustrated in Figure 4.2, the exact calculation of equilibrium vapor pressure is not straightforward because the real shape of the liquid-fluid interface is complex and non-spherical. In this study, the radial

cross section of the free surface is assumed to be circular and this geometric relationship was used to obtain the curvature of meniscus at the contact point (x, y).

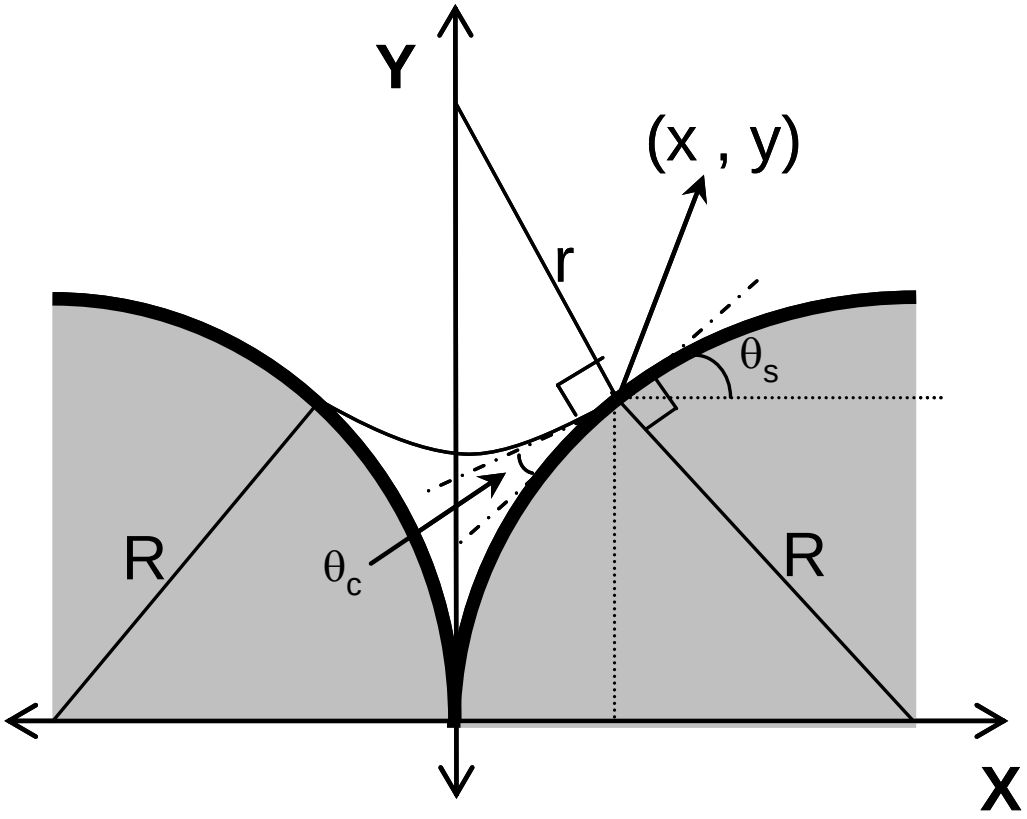

Figure 4.2 Illustration of capillary condensation at the space between two spherical particles (θc: intrinsic contact angle, θs: the angle between the x-axis and the tangential line at the contact point, R: particle radius, and r: radius of curvature of the meniscus).

Here, r denotes the unknown radius of curvature of the liquid surface, R the particle radius, θ_s the angle between the x-axis and the tangential line at the contact point, and θ_c the intrinsic contact angle between the liquid and solid. The *x*-*y* coordinates of the contact point are expressed with these geometrical considerations as follows.

$$y = R \sin(90 - \theta_s) = R \cos \theta_s \tag{3}$$

$$x = r \sin(\theta_s - \theta_c) \tag{4}$$

These coordinates are also located on the particle surface and obey the geometrical relationship of the spherical surface. One of the primary radii (r) can be expressed as a function of contact angle and particle size:

$$r = \frac{R(1 - \sin \theta_s)}{\sin(\theta_s - \theta_c)} \tag{5}.$$

If the value of θ_s is given, the pressure difference across the interface is calculated by

$$\Delta P = \gamma \left(\frac{1}{y} - \frac{1}{r} \right) . \tag{6}$$

The vapor pressure required for capillary condensation resulting in a specific meniscus height can be obtained by combining equations (2) and (6). The liquid amount is represented by the meniscus height (h) and its relative height is defined by h/R in the following expression.

$$\frac{h}{R} = \sin(90 - \theta_s) - \frac{(1 - \sin\theta_s)(1 - \cos(\theta_s - \theta_c))}{\sin(\theta_s - \theta_c)} \tag{7}$$

From the above equations (2), (3), (5), (6), and (7), it is observed that the relative meniscus height is dependent on the saturation condition. Predictions of meniscus height using this analysis are compared with experimental results in the next section.

4.5 Results and discussion

Samples of titania nanoparticles were subjected to condensation of TEOS in the controlled flow chamber and different saturation conditions were applied to vary the thickness of the layer. Surface-modified samples, prepared at a saturation ratio of 0.98, were used for the FTIR and XPS analyses. Figure 4.3 shows the 4000-500 cm^{-1} region of the spectra of the original titania sample and silica-coated titania. Both of the spectra are roughly similar to each other except in the region of ~1100 cm^{-1}. Two distinct peaks from the surface-modified titania are located around 1100 cm^{-1}, close to the characteristic peak of Si-O-Si bond stretching reported in the literature (Nyquist et al., 1997). The broad vibrational peaks for hydroxyl group around 3400 cm^{-1} are observable in both spectra because pure titania has chemically or physically adsorbed water molecules at room temperature, and modified titania forms titania-hydroxyl bond by the hydrolysis reaction of TEOS (Gamble et al., 1996). The peaks around 2900 cm^{-1} are clearly seen in

the modified sample and considered to be from C-H vibrations that are usually found at 2927, 2856, and 1400 cm^{-1} (Li et al., 2005). This C-H could be due to residual precursor on the titania surface. The rather weak and broad features observed in the spectra in the range 500-900 cm^{-1} are identified with the bulk TiO_2 skeletal frequency region. The bands from 910 to 960 cm^{-1} are widely known as the characteristic vibration of Ti-O-Si bond (Klein et al., 1996) but were not observed here likely because of the limited interfacial area between titania and silica. This comparison of FTIR spectra confirms the presence of Si-O-Si bonds in the modified sample.

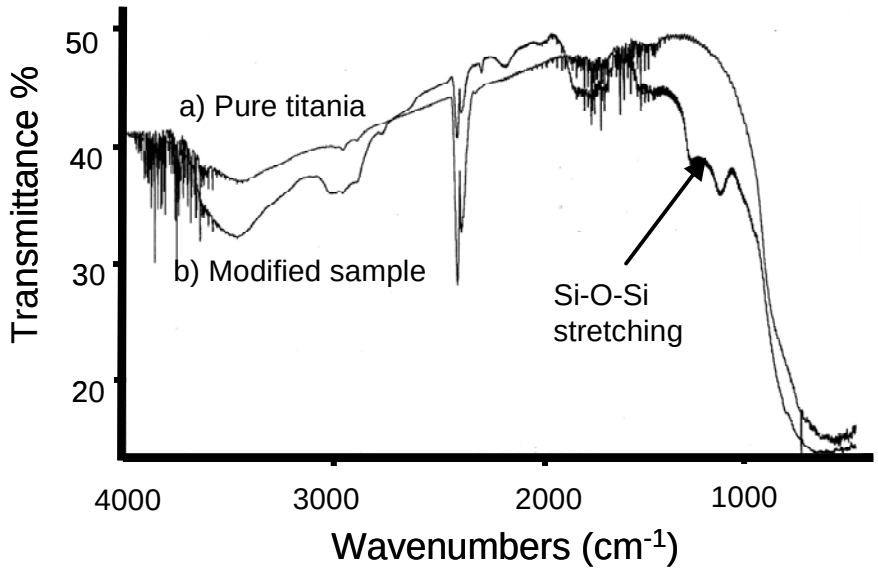

Figure 4.3 Spectra of (a) pure titania nanoparticles and (b) modified titania nanoparticles.

XPS was also used to probe the binding energies and the oxidation states of Si and Ti in order to verify the FTIR results and obtain a more detailed analysis of silica-coated titania. The XPS spectra of the original titania and the coated titania are also compared in Figure 4.4. The overall XPS spectra were recorded in the range of 0-1000 eV and the peaks associated with Ti-2p, O-1s, Si-2s, and Si-2p are shown. A large peak representative of Ti and a small peak representative of Si are observed by comparison of two spectra. From characteristic binding energies of titania and silica available in the literature(John F. M., 1995), the peak corresponding to Ti-2p of titania is located at the range of 458.8 ~ 459.2 eV and the peak corresponding to Si-2p of silica at the range of 103.3 ~ 103.7 eV. This comparison verifies the silica layer formation on the titania surface. In addition, the decrease of the Ti-2p peak intensity in the modified sample suggests that the outer surface of the titania nanoparticles is also covered by a silica layer a few nanometers thick because XPS is a surface-sensitive technique that analyses the sample to a depth of less than 10 nm (Wang et al., 1998; Pol et al., 2004).

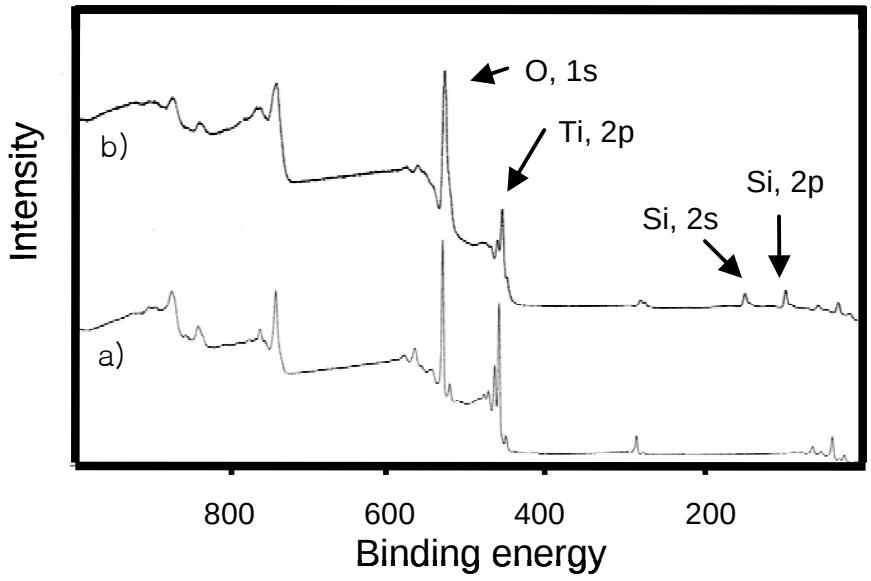

Figure 4.4 XPS results of a) pure titania and b) silica-coated titania.

The previous two techniques clearly verified the presence of silica in the modified sample but could not give any detailed information about the morphology and elemental distribution of the neck region. That information was obtained with HRTEM and STEM combined with EELS. The amorphous layer on the titania surface can be recognized more specifically in HRTEM images. As shown in the magnified HRTEM images in Figure 4.5, an amorphous layer is clearly identified, as distinct from crystalline titania based on the presence of lattice fringes which are only observable from crystalline

material. The layer is much thicker at the neck region between two particles than at the outer surface of particles. The layer at the right edge of the contact area appears to be thicker than the one at the left edge. The comparison of layers at both of the edges suggests that the shape of contact zone between two particles affects the formation of the layer. The conditions for capillary condensation depend on not only temperature and vapor pressure, but also the distance between particles and their shape.

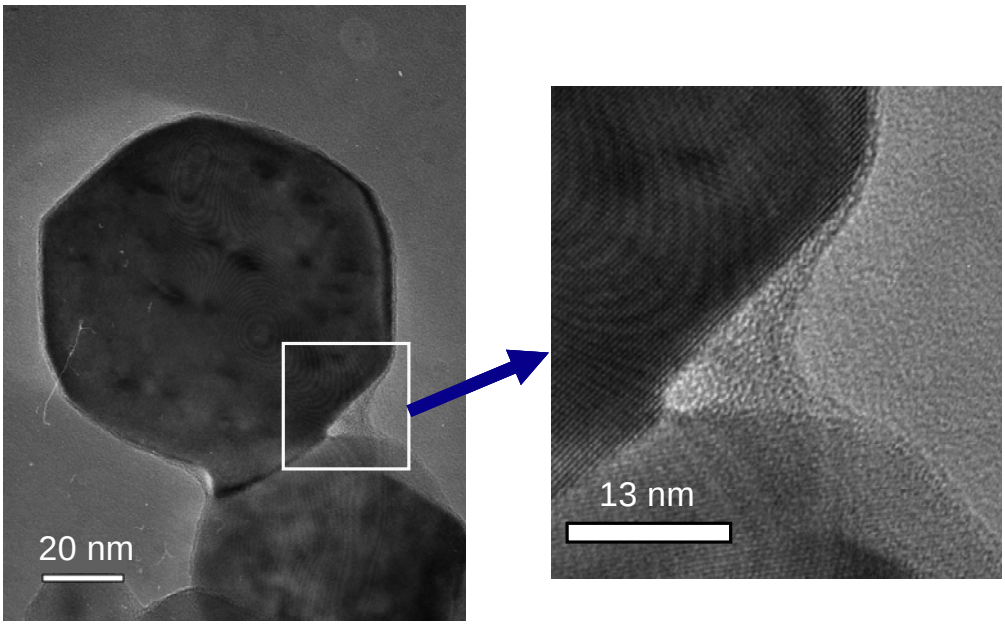

Figure 4.5 High resolution TEM image of selectively silica-coated titania nanoparticles.

In order to conform that the amorphous layer is silica and to check if there is any chemical variation on the particle surface, STEM-EELS analysis on the neck region and across an individual titania particle, which was prepared at a saturation ratio of 0.93, was performed. The technique is used to examine the elemental distribution with high spatial and chemical sensitivity. The EELS spectra are obtained by focusing the electron beam into a sub nanometer diameter probe and scanning the probe across the specimen, taking EELS spectra from many points. In this analysis, the target particles were selected far from the lacey TEM grid support and TEM images were obtained; a representative image is shown in Figure 4.6a. EELS spectra from the layer and the particle show clear peaks for Si-$L_{2,3}$ of silica around 100 eV and Ti-$L_{2,3}$ of titania around 460 eV. These inner shell excitation spectra suggest that the amorphous-like layer is silica. However, it is very hard to obtain a spectrum at the exact edge of the surface, and it is not clear whether the silica coats only the specific surface in the neck region. This drawback is solved by obtaining a series of spectra across the edge region of titania. In the high angle annular dark field (HAADF) image of Figure 4.6b, some nanoparticles with the diameter of ~ 60 nm appear white and they are interconnected with each other by silica, appearing as grey edges mostly in the neck region.

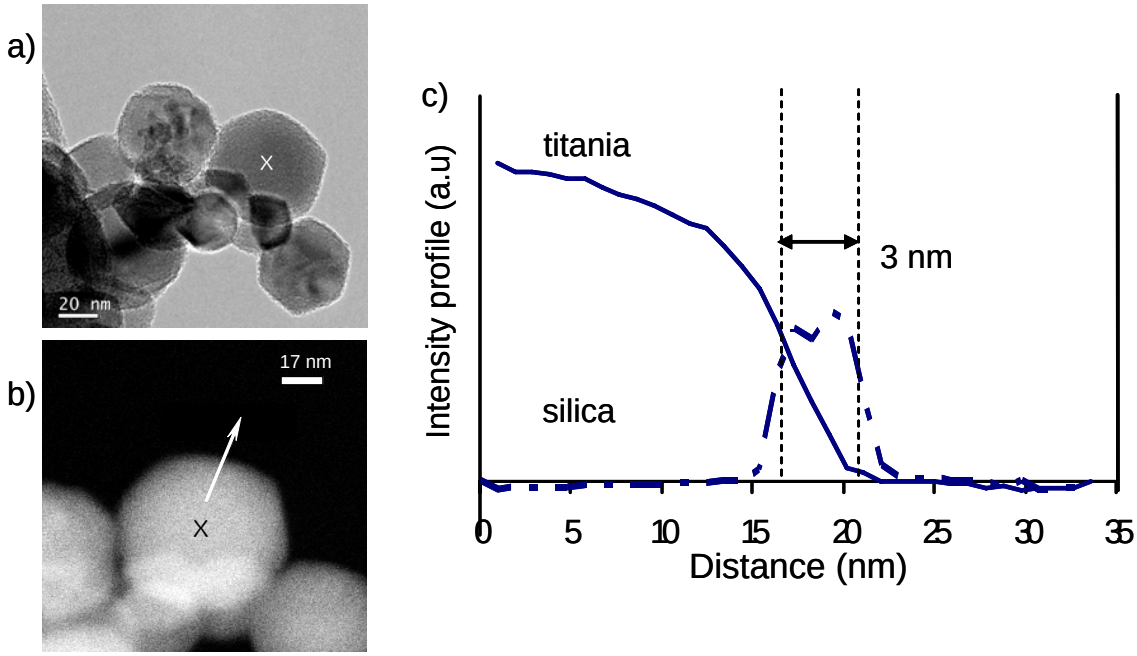

Figure 4.6 EELS analysis results: a) High resolution TEM image, b) High angle annular dark field image of a selectively-coated titania particle denoted by x in a) where a white arrow represents the path of the line spectra of 36 with a step size of 1 nm, c) Intensity profiles of two peaks for Si-$L_{2,3}$ of silica around 100 eV and Ti-$L_{2,3}$ for titania around 460 eV extracted from series of spectra along the depicted line in Figure 4.6b.

36 EELS spectra were measured along the line shown in Figure 4.6b, about 35 nm in length with an interval of about 1 nm. From the line-spectra across the edge, some information including intensity profiles and thickness can be estimated. The extracted intensity profiles are shown in Figure 4.6c and exhibit the Si-$L_{2,3}$ and Ti-$L_{2,3}$ profiles. The correlation of these profiles with the HAADF image allows mapping of the exact chemical distribution in the particles. In the profiles, one can see that the high intensity of silica is mainly observed in the edge region where the intensity of titania is nearly zero (Yoshioka et al., 2004). It represents that a thin silica layer approximately 3 nm thick covers even the outer surface of titania far from contact zone because the TEOS precursor is very wettable on the surface of titania and forms an adsorbed multilayer even in undersaturated conditions (saturation ratio < 1.0). Combining results from various analysis techniques, it can be concluded that an amorphous silica layer is formed on the titania surface by the condensation process and that this layer is built up more dominantly in the capillary zone than on other convex surfaces.

The saturation ratio effect on the relative meniscus height was also investigated. Titania nanoparticle samples were subjected to capillary condensation at various saturation conditions and TEM images at four different saturation ratios were obtained, with typical images given in Figure 4.7.

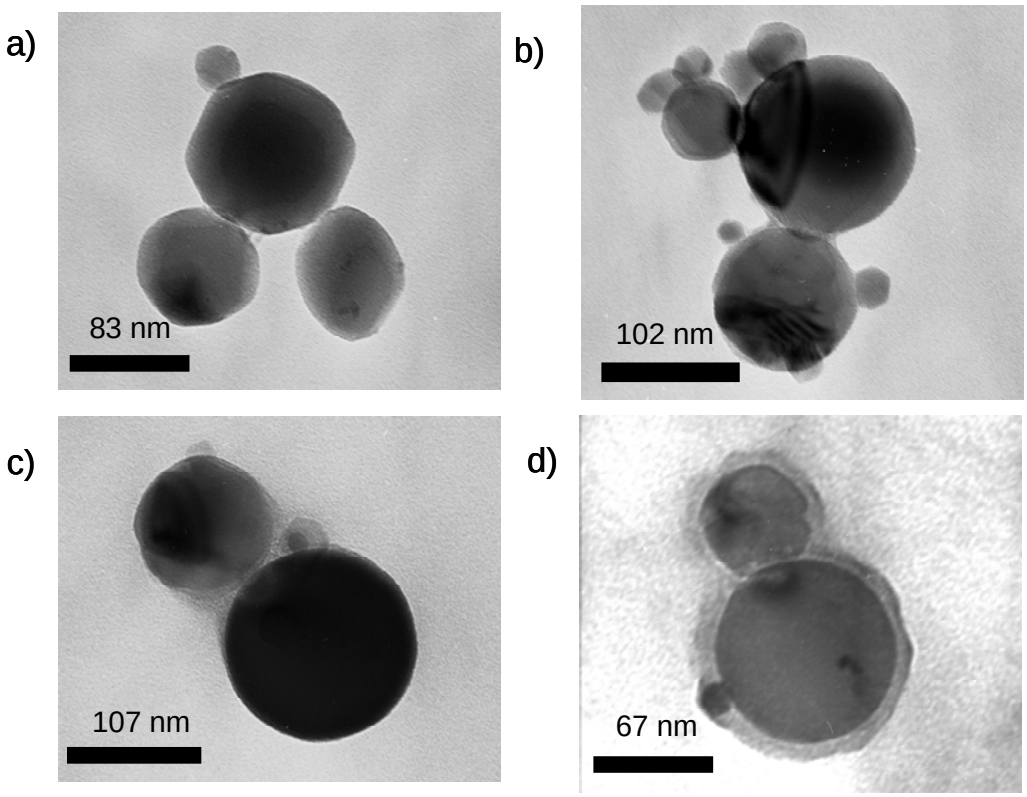

Figure 4.7 Variation of silica layer thickness with saturation ratio (SR) in capillary condensation: a) SR=0.81, b) SR=0.86, c) SR=1.2, and d) SR=2.0.

Amorphous silica formed by hydrolysis of TEOS is easily identified in the electron microscopic image because of contrast difference between it and the crystalline titania nanoparticles. As shown in Figure 4.7a, a very small trace of silica is observable at a lower saturation than 0.90. The small trace is not obvious in the TEM image when two particles are overlapping because of the limited visibility of a 2-dimensional image. As the saturation ratio increases, the layer becomes thicker in Figure 4.7b and the bridge-shaped layer is observed above the saturation ratio of 1.0 (Figure 4.7c). When a high saturation ratio of 2.0 is applied, all particle surfaces are uniformly covered by a silica layer about 8 nm thick, as shown in Figure 4.7d. The BET surface area measurement of a modified sample, which was treated at a saturation ratio of 1.1 showed that the surface area decreased very little from 10 m^2/g for the untreated sample to 9 m^2/g after condensation. This suggests that the surface modification process does not result in any significant loss of surface area of the original sample.

The experimental results show that the thickness of silica layer is strongly dependent on saturation ratio and is controllable in the experiments. This dependency was compared to a theoretical analysis using the Kelvin equation. In order to quantitatively compare the silica layer thickness on the different sized particles, the vertical layer height (h) was measured from the point of contact between two particles or

the closest proximity if the particles were not in contact. The relative thickness (*h/R*) is defined by dividing the meniscus height by the particle radius. The average relative thickness value at the specific saturation ratio was obtained from 3-5 TEM images and, as shown in Figure 4.8, the values at the different saturation ratios were compared with the theoretical predictions calculated from equations (2), (6), and (7). The y-error bars represent the standard deviations of the measurements of the average relative thickness. The x-error bars represent the standard deviations of the saturation ratio during the experiment, which were estimated from vapor pressure fluctuation in the flow. The standard deviation of the average saturation ratio was obtained from the vapor pressure data, which were evaluated every 5 minutes during a 2 hour experiment from the continuous TCD measurement. Most of experiments show the maximum deviation is less than 5%. The theoretical calculation shows that the relative thickness of the silica layer increases gradually below the saturation ratio of 0.90 and grows abruptly between 0.90 and 1.0. The experimental results also show a similar trend up to the saturation ratio of 1.0. However, above 1.0, the silica layer thickness does not increase in proportion to saturation ratio and seems to be invariant. This discrepancy is believed to occur because the thickness of the condensed layer above 1.0 is governed by equilibrium thermodynamic conditions and the interfacial stability of the liquid TEOS film.

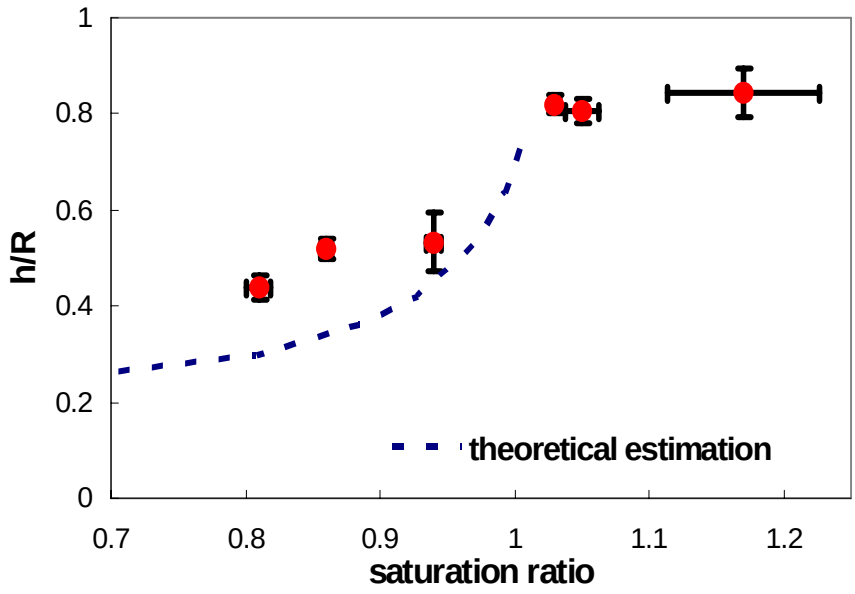

Figure 4.8 Comparison of experimental results and theoretical analysis based on Kelvin equation (h: vertical height of silica layer at the contact point between two particles and R: radius of particle). The theoretical analysis is valid only up to the saturation ratio of 1.0.

Generally, the thin film interfaces are thermodynamically metastable (Mazzoco and Wayner, 1999; Maeda and Israelachvili, 2002) and are easily affected by small fluctuations of the bulk pressure. In the proposed process, the temperatures of the bath and the chamber were carefully controlled in order to obtain a constant saturation condition but there are always some fluctuations observed in the TCD measurement due to non-uniform vaporization at the surface of the liquid precursor in the bubbler. These

fluctuations may affect the meniscus stability considerably above a saturation ratio of 1.0. From the experimental result shown in Figure 4.7d, a uniform silica layer forms on all surfaces at a saturation ratio of 2.0.

4.6 Conclusions

In this Chapter, titania nanoparticles interconnected by silica were prepared by a capillary condensation process. The silica layer was formed dominantly in the capillary zone between particles under the saturation ratio of 1.0 and thin layer on the outer surface of titania far from the capillary zone was also observed near the saturation ratio of 1.0. Although only the TEOS-titania system was used in the process, it should be possible to apply these results to different systems that have similar adsorption trends between the precursor and the particle surface because the main mechanism of coating is based on capillary wetting phenomena. No noticeable variation of BET surface area was observed after silica formation and measurements of the coated material with FTIR, XPS, TEM, and EELS clearly conformed that the layer consists of amorphous silica and the thickness of the layer varies on the surface of titania. The amount of condensed material could be controlled by adjusting the saturation conditions. The silica layer thickness

depends strongly on the saturation ratio up to a saturation ratio of 1.0 and a uniform silica layer was observed on the entire surface at the saturation ratio of 2.0. In undersaturated conditions (saturation ratio < 1.0), nanoscale meniscus formation is governed by macromolecular thermodynamic phenomena, which was analyzed on the basis of the Kelvin equation. The experimental results qualitatively agreed well with the theoretical analysis up to the saturation ratio of 1.0 where the relative thickness of silica layer increases as the saturation ratio increases. However, in supersaturated conditions (saturation ratio > 1.0), the change of the silica layer thickness could not be explained by the Kelvin equation because it is governed by equilibrium thermodynamic conditions as well as the interfacial stability of the meniscus.

The capillary condensation process is affected by many other aspects of particle geometry in addition to thermodynamic properties of temperature and vapor pressure. Thus, in contrast to the macroscopic Kelvin equation, molecular simulations such as Monte Carlo simulations of thermodynamic equilibrium are more practical to study the interfacial stability of the meniscus for systems whose dimensions are several molecular diameters. Some possible factors affecting capillary condensation such as the geometry of the particle surface and the gap distance between particles can be explained by introduction of non-spherical particle geometry and by application of Monte Carlo

simulation for capillary condensation over non-contacting particles with some gap spaces. These effects were investigated in Chapter 5.

V. GRAND CANONICAL MONTE CARLO SIMULATION STUDY OF CAPILLARY CONDENSATION BETWEEN NANOPARTICLES

5.1 Abstract

Capillary condensation at the nanoscale differs from condensation in the bulk phase, because it is a strong function of surface geometry and gas-surface interactions. Here, the effects of geometry on the thermodynamics of capillary condensation at the neck region between nanoparticles are investigated via a grand canonical Monte Carlo simulation using a 2-dimensional lattice gas model. The microscopic details of the meniscus formation on various surface geometries are examined and compared with results of classical macromolecular theory, the Kelvin equation. It is assumed that the system is composed of a lattice gas and the surfaces of two particles are approximated by various shapes. The system is modeled on the basis of the molecular properties of the particle surface and lattice gas corresponding to titania nanoparticles and tetraethoxy orthosilicate (TEOS) molecules, respectively. This system was chosen in order to reasonably emulate previous experimental results for capillary condensation on nanoparticle surfaces in Chapter 4. Qualitatively, simulation results show that the

particular geometry in the capillary zone, the surface-surface distance, and the saturation ratio are important for determining the onset and broadening of the liquid meniscus. The meniscus height increases continuously as the saturation ratio increases and the meniscus broadens faster above the saturation ratio of 0.90. The change of the radius curvature of the particle surface affects the dimension of capillary zone, which drives more condensation in narrow zones and less condensation in wide zones. The increase of surface-surface distance results in the decrease of meniscus height or even the disappearance of the meniscus entirely at lower saturation ratio. These effects are significant at the nanoscale and must be carefully considered in order to develop predictive relationships for meniscus height as a function of saturation conditions.

5.2 Introduction

The gas-liquid transition in a confined space such as a slit or pore often occurs at a lower pressure than the bulk saturation pressure. This phenomenon of capillary condensation has been of interest for many decades in various research fields such as the vapor-liquid phase equilibria in a confined geometry (Defay and Prigogine, 1966; Melrose, 1972), the dispersion and wetting of powders (Carman, 1953), the deformation

of moist soils and porous media (Haines, 1925; Fisher, 1926), and the adhesion of dust and powder to surfaces (Zimon, 1982). An approximate description of meniscus in a confined geometry is easily made in terms of the Kelvin equation but an exact treatment must take into account the deviation of the meniscus from sphericity (Adamson and Gast, 1997). Starting with the early work of Haines (Haines, 1925) and Fisher (Fisher, 1926), many researchers have investigated the characteristics (shapes, curvatures, volumes and capillary forces) of the liquid meniscus between two solid bodies analytically (Orr et al., 1975; Debisschop and Rigole, 1982; Lian et al., 1993) and experimentally (Mcfarlane and Tabor, 1950; Mason and Clark, 1965).

This phase transition by capillary condensation, especially in small scale, is susceptible to fluctuations and hysteresis effects, various finite size effects, and surface characteristics. Because of those uncertainties, various simulation studies were performed to investigate the capillary condensation phenomena in a confined geometry. Effects of geometrical dimension on the gas-fluid transition were presented in well-defined slitlike pores, which showed how the condensation behavior changes relative to its bulk behavior (Binder and Landau, 1992; Papadopoulou et al., 1992). The phase behavior in geometrically and chemically heterogeneous pores was also studied by computer simulation techniques in order to understand unusual adsorption phenomena in

real pores with complex structure and network topology (Rocken and Tarazona, 1996; Bock and Schoen, 1999). The capillary condensation in various nanoporous materials (Coasne and Pellenq, 2004; Puibasset and Pellenq, 2005; Birkett and Do, 2006) has been an emerging topic due to practical interest in the application of nanostructured materials as filters, sorption medias, and gas storage materials.

Recently, this subject has been of interest because of the recognition of the effects of capillary condensation at nanocontacts, which are of importance for several measurement techniques such as atomic force microscopy (AFM) and sphere tensiometry, and their applications. For example, the capillary force between AFM tips of various shapes and a flat surface was investigated by exact and approximate numerical calculations and discussed through comparison to the Kelvin equation (Marmur, 1993; de Lazzer et al., 1999). Their results showed that the accuracy of the approximation depends on the contact angles involved, the geometry of tip shape, and the space between the tip and flat surface. A capillary force measurement technique was developed for a pendular liquid bridge between rigid spheres (Willett et al., 2000; Adams et al., 2002). The equilibrium aspects of capillary condensation in a similar system were also studied using a surface force apparatus (Kohonen et al., 1999; Maeda and Christenson, 1999),

and results indicated that the phase behavior of liquid condensates is dependent on the degree of confinement of the material.

In the experimental study of Chapter 4, a new process was developed to make interparticle connections between nanoparticles using capillary condensation and surface reaction, as shown schematically in Figure 5.1. The main purpose of this process is to modify or enhance the properties of nanostructured material such as mechanical strength while minimizing loss of original surface area. Experimental observations in the form of transmission electron microscopic (TEM) images showed that the thickness of the coated layer is strongly dependent on the nanoscale geometries of the particles and the proximity of two solid surfaces as well as on saturation conditions. Although the numerical and analytical manipulations of the Kelvin equation describe the capillary phenomenon, macroscopic theories are questionable for describing systems whose dimensions are several molecular diameters or less (Binder and Landau, 1992; Albano et al., 1997). Additionally, macroscopic theories do not give the microscopic details of gas-liquid interfaces including fluctuations in the meniscus and an exact density profile of the meniscus.

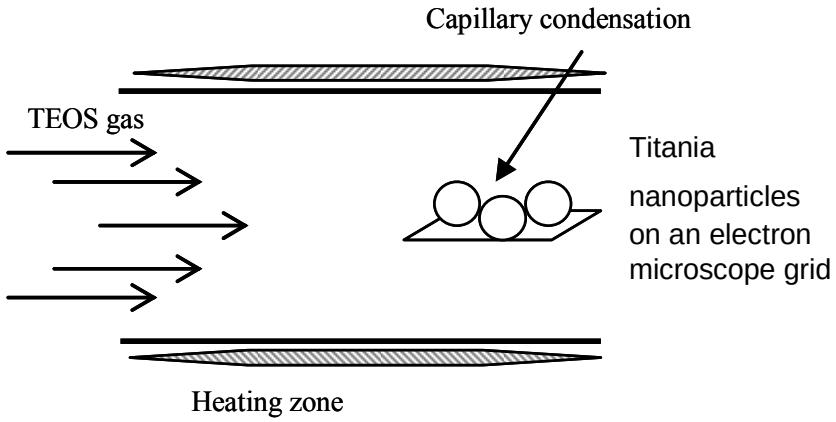

Figure 5.1 Illustration of a capillary condensation process.

To obtain more detailed information about nanoscale capillary condensation phenomena, the grand canonical Monte Carlo (GCMC) simulation approach has been utilized, a technique commonly used to investigate phase equilibria of heterogeneous adsorption. Here, instead of simulating a complex experimental system in detail, I qualitatively examine meniscus behaviors for different surface geometries and various surface-surface distances using a simple model, a 2-dimensional lattice gas on solid surfaces. This lattice gas model, in spite of its simplicity, is practical for simulating different saturation conditions and geometrical structures with relatively large lattice sizes at a reasonable speed. Additionally, the surface binding energy was adjusted under conditions of fixed chemical potential and temperature in order to resemble

characteristics of wettability of TEOS on the surface of titania. The results of this simulation work are amenable to direct experimental verification in a qualitative sense.

This study is outlined as follows. Sec. 5.3 gives the analysis of the capillary condensation on spherical and elliptic surfaces of particles by approximate numerical calculations of Kelvin equation. In Sec. 5.4, I describe in detail the lattice gas model, the system geometry, and the method used in the GCMC simulation. The details of simulation results and the comparison of macroscopic analysis are systematically discussed in Sec. 5.5. The dependence of the meniscus height on the particle surface curvature and the distance between particles is also investigated. Sec. 5.6 summarizes conclusions of this study.

5.3 Analytical approach of capillary condensation phenomena

I consider a system of two particles in close contact with a small amount of liquid filling the gap. Two identical particles are assumed to be rigid and rotationally symmetric with respect to the *x*-axis, and the liquid meniscus is also symmetric with respect to the *y*-axis. Thus, the only half of the cross-sectional geometry was shown in Figure 5.2. The meniscus touches both the particles at a contact point (x_0, y_0) where one

of the primary radius is y_0 and the contact angle is θ_c. Generally, the pressure difference (capillary pressure) for spherical bubbles or drops can be formulated by the classical Kelvin equation. However, the radius of curvature of the liquid-gas interface must be determined in order to obtain the pressure difference across it and the exact calculation of the arbitrarily shaped meniscus is tedious requiring numerical integration (Fisher, 1926; Melrose, 1966; Melrose and Wallick, 1967).

In this study, the radial cross section of the free surfaces is assumed to be circular, which is very good approximation for the various interfacial shapes (Mason and Clark, 1965; Clark et al., 1968), and the curvature of the meniscus is obtained at the contact point (x_0, y_0). Under these assumptions, some analytical expressions to determine capillary pressure can be derived. The relationship for the case of spherical particles ($R' = R$) was shown in Chapter 4.

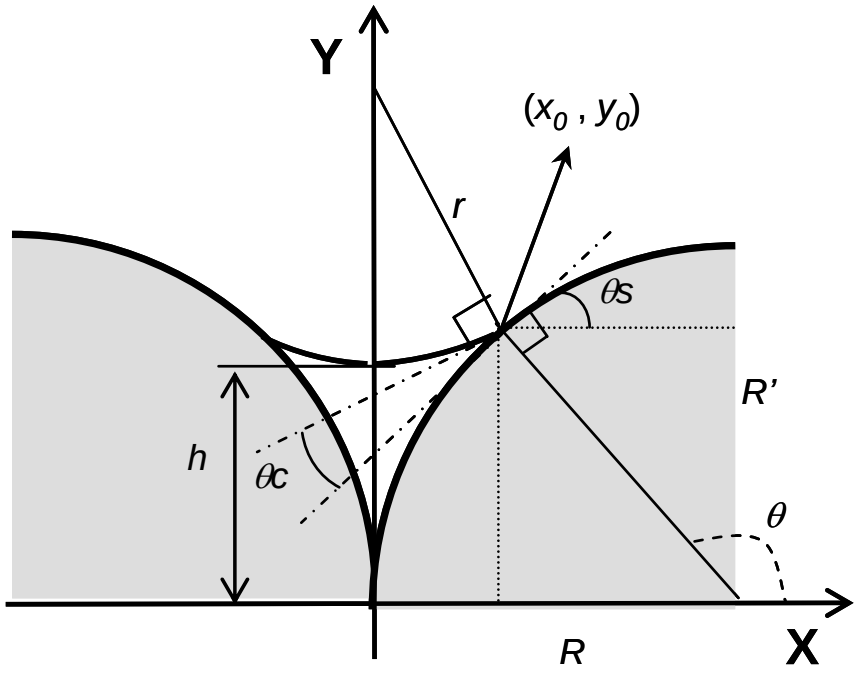

Figure 5.2 Cross-sectional geometry of liquid meniscus when two particles are in close contact. In the figure, the angle of θc represents the intrinsic contact angle, θs the angle between the x-axis and tangential line at the contact point (x_o, y_o), and θ the angle of contact point for the parametric expression of particle surface. The particle shape is characterized by R and R' which represent major axes in a two dimensional surface. The meniscus height is depicted by *h* and two primary radius curvatures are given as r and y_0, respectively.

$$\Delta P = \gamma\left(\frac{1}{y_0} - \frac{1}{r}\right) \tag{1}$$

$$y_0 = R\sin(90 - \theta_s) = R\cos\theta_s \tag{2}$$

$$r = \frac{R(1 - \sin\theta_s)}{\sin(\theta_s - \theta_c)} \tag{3}$$

In these equations, ΔP is the difference in pressures due to the surface curvature, γ is the surface tension, r is the unknown radius of curvature of the liquid surface, R is the radius of particles, θ_s the angle with the x-axis at the edge of the condensate meniscus, and θ_c the intrinsic contact angle. The liquid amount is represented by the meniscus height (h) and its relative height is defined by h/R' in the following expression.

$$\frac{h}{R'} = \sin(90 - \theta_s) - \frac{(1 - \sin\theta_s)(1 - \cos(\theta_s - \theta_c))}{\sin(\theta_s - \theta_c)} \tag{4}$$

For the case of $R' \neq R$, the cross-sectional shape of particle surfaces is assumed elliptical and the meniscus is still assumed to be circular. Therefore, the contact points (x_0, y_0) of the liquid-gas interface with the particles obey the following relationship

$$\frac{(x_0 - R)^2}{R^2} + \frac{y_0^2}{R'^2} = 1 \tag{5}$$

where R is the length of the major axis, R' is the length of the minor axis, and (x_0, y_0) are the coordinates of the contact points. The contact points are located on the surface of particles and can also be represented by parametric expressions in terms of trigonometric functions, as shown in equations (6) and (7). The other equation comes from the

condition that the meniscus interface forms an intrinsic contact angle with the particle surface. By summarizing the above considerations, the contact point (x_0, y_0) and tangential line at the contact point can be expressed respectively

$$x_0 = R(1+\cos\theta) = r\sin(\theta_s - \theta_c) \tag{6}$$

$$y_0 = R'\sin\theta \tag{7}$$

and

$$\tan\theta_s = \frac{dy}{dx} = -\frac{R'}{R\tan\theta} \tag{8}$$

where θ is the angle between the line connecting the contact point and the center of the particle, and the x-axis. From equations (5), (6), and (7), the radius of the circular meniscus is given as

$$r = \frac{R(1+\cos\theta)}{\sin(\theta_s - \theta_c)} \tag{9}$$

where θ varies from 90º to 180º. By using equations (1), (6), (7) and (9), the pressure difference across the interface can be represented as function of the dimensions of particle (R and R'), the contact angle (θ_c), and the angle between the horizontal and the line tangent to the surface at the contact point (θ_s). The relative meniscus height is also derived in the same way as for the spherical particle.

$$\frac{h}{R'} = \sin\theta - \frac{R}{R'}\frac{(1+\cos\theta)(1-\cos(\theta_s - \theta_c))}{\sin(\theta_s - \theta_c)} \tag{10}$$

5.4 Simulation details

In the present study, a gas-liquid transition was investigated by means of GCMC simulation for a 2-dimensional lattice gas model. In this model, it is assumed that the system consists of many lattice sites on a square grid and each lattice site is either empty or occupied by only one molecule with nearest neighbor attractive interactions in the bulk. All the lattice sites are classified as either bulk or surface sites. When the lattice site is adjacent to hard walls such as an adsorbed molecule on solid surfaces, it has interactions with the wall as well as the nearest neighbor sites. The model system describes the lattice gas molecules confined between two curved surfaces of either spheres or ellipses separated by d lattice spacings, as shown in Figure 5.3. The curved surface is represented by two major axis lengths of R and R' in the horizontal and vertical directions, respectively. The surface sites are defined as the collection of lattice sites nearest to the continuous surface line. They are attracted to the surface with a binding energy (b_s) as well as to their nearest neighbors with an attractive energy (ε). The system is symmetric with respect to the y-axis and periodic boundary conditions (Frenkel and Smit, 2002) are imposed on $x = R+d/2$ and $x = -(R+d/2)$ in order to minimize computational time. For the other boundaries, a stochastic boundary condition (Frenkel and Smit, 2002) at $y = 2R'$

and a reflecting boundary condition (Jang et al., 2002) only for the existing gap space at y = 0 are applied.

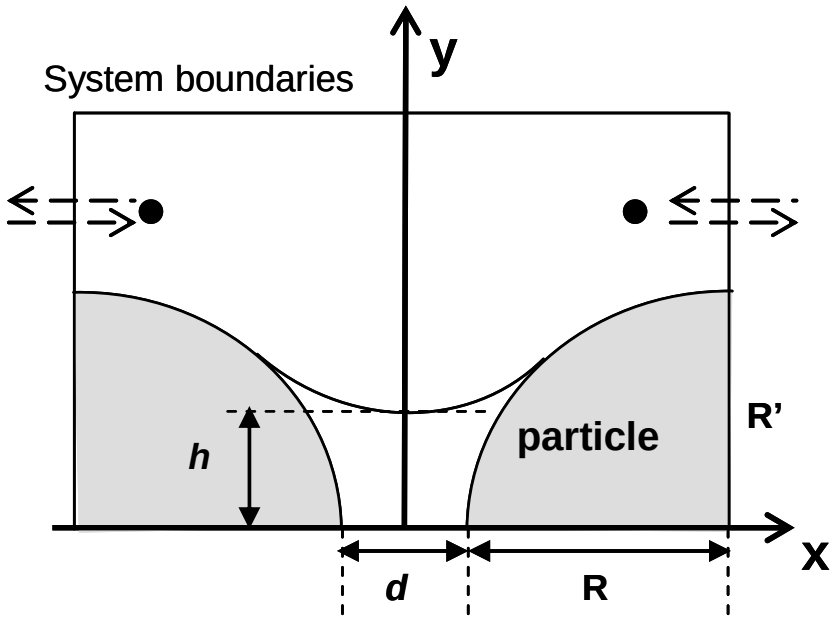

Figure 5.3 Schematic of a simulated system: lattice gases are confined by two solid surfaces. The amount of condensates is characterized by the meniscus height (h). A two-dimensional plane is composed of 131 X 196 ~ 295 X 196 square lattices depending on particle geometry (ratio of R and R') and gap spacing (d). The periodic boundary condition is applied at the horizontal ends ($x = \pm(R+d/2)$) and the reflecting boundary condition is at y=0. At y=2R' open to the reservoir, the stochastic boundary condition is used.

The system described above is represented by a Hamiltonian (H), which is expressed in terms of the occupation number c_i (0 or 1) for the ith sites as follows:

$$H = -\varepsilon \sum_{\substack{i,j = nearest \\ neighbor\ pair}} c_i c_j - b_s \sum_{\substack{k = particle \\ surface}} c_k \tag{11}$$

The typical grand canonical ensemble assumes that the system is in equilibrium with bulk reservoir at constant chemical potential μ, volume V, and temperature T. The relevant Hamiltonian for GCMC is H-μN (N = number of occupied sites). However, it is well known that a lattice gas model in a grand canonical ensemble corresponds to an Ising model in a canonical ensemble (Hill, 1956). In this study, the Ising model with Metropolis importance sampling (Binder and Baumgärtner, 1984) was applied and the simulation results were interpreted by changing the spin value (1 or -1) into the occupation number (1 or 0) of the ith site. Simulation runs were carried out over a minimum of 10000 Monte Carlo steps per site, out of which the first 4000 steps were discarded for equilibration. The sites located in the capillary space (y<R') were visited more often than the bulk (y>R'). Each Monte Carlo step amounts to considering a site for removing a particle, if it was occupied, or for adding a particle, if it was empty, which is little different from conventional GCMC simulation (no displacement step). As an

initial condition, I use completely empty lattice sites in order to consider the adsorption phenomena observed in the experimental study reported earlier.

Using this relatively simple lattice model for emulating previous experimental study in Chapter 4, it is necessary to reasonably estimate the geometric and energetic parameters: lattice dimensions, interaction parameters, and thermodynamic variables. Those parameters help the model to describe the equilibrium shape of tetraethoxy orthosilicate (TEOS) meniscus on the surface of titania (TiO_2). Thus, I can attempt to connect simulation results to experimental results previously reported in Chapter 4.

One lattice spacing in the lattice dimension is approximated based on the Lennard-Jones (L-J) parameters for TEOS (Fokin et al., 2001). The typical TEOS-TEOS distance in the liquid phase is 7.17 Å which is equivalent to 1.02σ in terms of the L-J parameter of TEOS. The potential energy at that distance is assumed to be the attractive energy (ε) between the nearest neighbor sites. From the above dimension, the horizontal radius (R) of the particle is fixed as 98 lattice spacings, or 70.3 nm, which is a typical particle size used in the experiment. The vertical radius (R') is varied as R'= 65, 98, and 147 lattice spacings with R fixed at 98 lattice spacings in order to study the effect of the deviation from sphericity. The gap space between particles is also changed from d=0 to d=12 lattice spacings for investigating the effect of particle proximity.

The interaction between TEOS and the surface of titania is hard to estimate because there are few reports of experimental adsorption. Some previous experiments were conducted by other groups to investigate the mechanism of TEOS adsorption by thermal desorption spectroscopy, and their results showed that TEOS adsorbs on titania surface by a dissociative reaction and produces an intermediate mixture of adsorbed di- and triethoxysilanes (Gamble et al., 1993; Gamble et al., 1996). However, various theoretical calculations of adsorption energy for small molecules (water, ammonia, and alcohol) were performed by first principles calculations (Bates et al., 1998; Bates et al., 1998) and a semi-empirical method (Bredow and Jug, 1995; Homann et al., 2004). These reports have presented the adsorption energy of water and methanol on the surface of titania surface. The molecules adsorb by dissociative reaction and the calculated values were comparable to experimentally measured adsorption energies (Hollabaugh and Chessick, 1961; Carrizos et al., 1971; Anderson et al., 1972). The calculated values are, in general, from 65 to 110 kJ/mol, which is approximately 2-8 times stronger than a typical hydrogen bond strength from 15 to 25 kJ/mol (Thiel and Madey, 1987). It is assumed that TEOS undergoes an adsorption mechanism similar to water and methanol on the titania surface and that its adsorption energy is the same order of magnitude. Based on the above numbers, various ratios of titania-TEOS interaction to TEOS-TEOS

interaction from 2.6 to 8.0 were tested and the ratio of the surface binding energy (b_s) to the attractive energy (ε) is chosen as 2.6 in this study, which is a reasonable value considering the observed complete wetting behavior (Pandit et al., 1982) of TEOS on titania surfaces.

Temperature is considered in terms of a reduced temperature as $T^* = T/T_c$, where T_c is the bulk critical temperature for the lattice gas model and is only dependent on the attractive energy ($k_B T_c/\varepsilon=1/2(\mathrm{Ln}(1+\sqrt{2}))$) (Hill, 1987). In this simulations, the results are presented for a reduced temperature of $T^* = 0.52$, which corresponds to a reasonable temperature for the capillary condensation process. The critical chemical potential is also known exactly as $\mu_c = -2\varepsilon$ and the saturation ratio (SR) can be expressed as

$$SR = \exp[(\mu - \mu_c)/k_B T]. \qquad (12)$$

This saturation ratio was varied from 0.40 to 0.98 in this study.

The average occupancy of each site was evaluated from regularly sampled lattice configurations after the equilibration. From this information, I obtained the density profile in order to determine the meniscus height. The phase of each site was decided based on the average site occupancies, a liquid site if its density is above 0.5 and a gas site if it is less than 0.5. For the horizontal position at $x = 0$, total number of liquid sites are vertically counted from the lowest sites at $y = 0$ and the meniscus height (h) is

reported with respect to the particle size (R') as a relative meniscus height (h/R'). The simulation algorithm was evaluated by changing the ratio of surface energy to bulk interaction energy ($b_s/\varepsilon<0.5$, $0.5<b_s/\varepsilon<1$, and $1<b_s/\varepsilon$) and complex wetting or drying behavior (complete or incomplete) on a flat solid surface (Pandit et al., 1982) was confirmed under various temperatures.

5.5 Results and discussion

Capillary condensation phenomena on the surface of nanoparticles was studied by using Monte Carlo simulations and analytical calculations (Kelvin equation) for a specific system with various geometries. Unlike the previous reports, which covered idealized pores, tip-substrate gaps in atomic force microscopy, and gaps between two infinite plates, here, capillary condensation between two curved surfaces was investigated in detail. The geometry of the particle surface, proximity between particles, and saturation condition are the focus here with the goal of obtaining molecular level insight into liquid meniscus formation. It is intended to explain variability in relative meniscus height at the same saturation ratio, which was observed in the previous experimental study shown in Chapter 4, in terms of nanoscale size and meniscus stability.

Consider first the capillary condensation of lattice gases between two spherical particles in close contact. A confined fluid structure is easily observed in terms of local density. Figure 5.4 presents the local density profiles in a 2-dimensional plane at four different saturation conditions, corresponding to saturation ratios of 0.60, 0.80, 0.92, and 0.98. As shown in the figure, red indicates the highest average density of a lattice site and purple the lowest. Lattice sites with average density higher than 0.5 form a bridge-shaped meniscus around the contact point of two surfaces. The dimension of this meniscus generally increases with increasing saturation ratio and the height of the meniscus at the middle (x=0) is used as characteristic length. The height is increased by 8 lattice spaces (~ 6 nm) when the saturation ratio is increased from 0.60 to 0.80 but this increment become significantly large (24 spaces, ~ 17 nm) from 0.92 to 0.98. This shows that the saturation condition could be tuned in order to obtain a specific meniscus dimension and, especially at the saturation between 0.90 and 1.0, the meniscus height is significantly affected by the saturation condition.

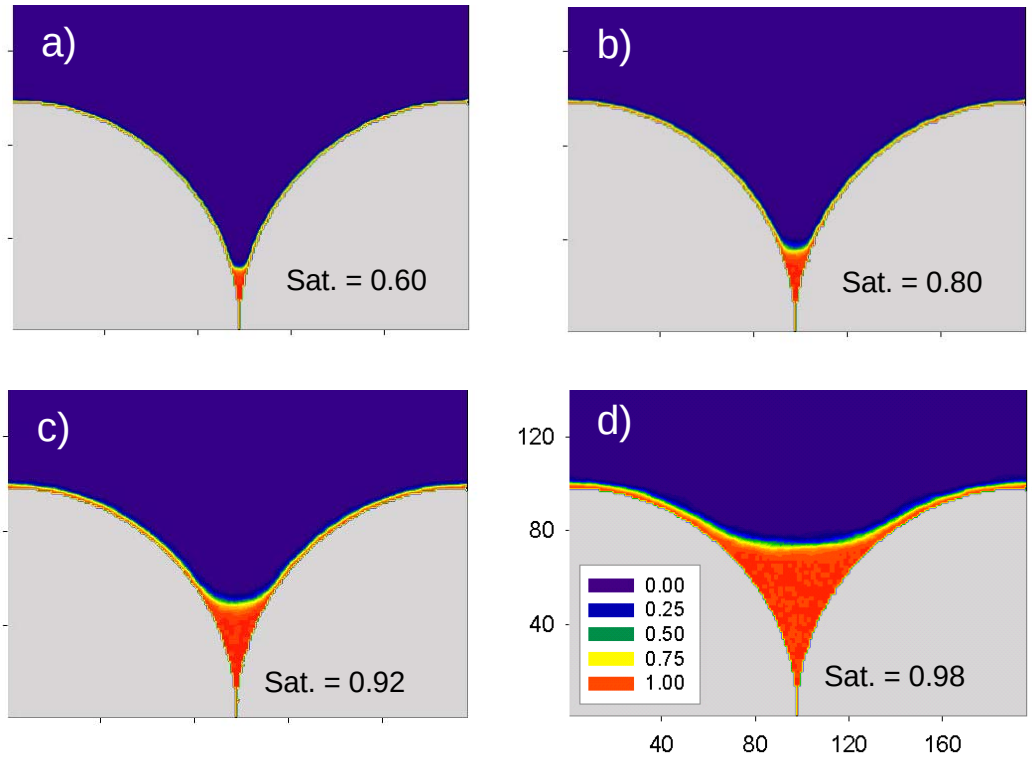

Figure 5.4 Liquid meniscus formation between spherical particles at various saturation conditions with a reduced temperature of T^{*}=0.52. Colors represent the average densities of each site, grey areas represent the titania particles, and scales in x-y axis show the number of lattice sites with one lattice size of 7.17A.

In more detail, the particle surface far from the meniscus was observed. The lattice gases used in the simulation have a strong interaction with the particle surface ($b_s/\varepsilon > 1$) and all the lattice sites on the surface are generally occupied at under-saturated condition. The simulation results show that a single monolayer covers the particle surface at the saturation ratios less than 0.80 and double or triple layers above 0.90.

For capillary condensation over two spherical particles in contact, the characteristic length of the meniscus was obtained at each saturation condition and compared with estimates made using the analytical expression given in equation (4). Figure 5.5 shows the meniscus between two contacting particles expands continuously and there is no abrupt phase transition, unlike what is frequently observed in simulations of capillary phenomena occurring in slit-like pores (Rocken and Tarazona, 1996; Libby and Monson, 2004) and tip-substrate systems (Jang et al., 2002) at saturation ratios less than 1.0. This continuous increase in meniscus height for two particles in contact has an important implication for possible thermodynamic control of the experimental study. Based on the estimate of the physical dimension of the lattice, the results suggest that the relative height of the meniscus (h/R') can be tuned from 0.23 to 0.74, which corresponds to 17 nm and 52 nm in the system. The vertical dimension of the meniscus changes

linearly with saturation ratioat saturation ratios less than 0.80 and increases rapidly above 0.8.

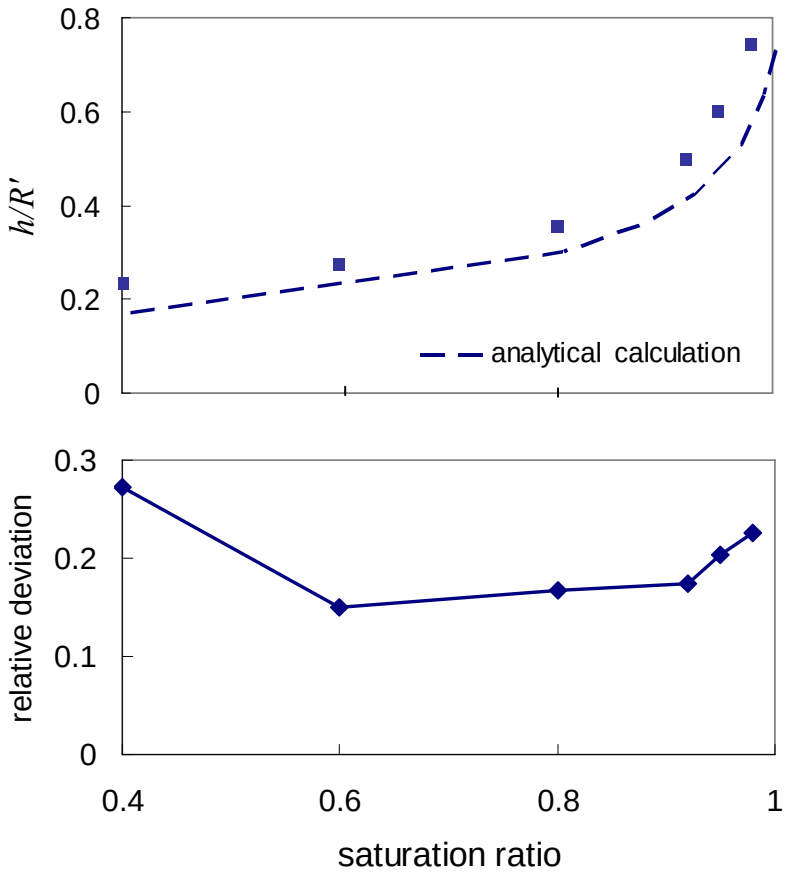

Figure 5.5 Comparison of simulation results with analytical calculation based on Kelvin equation at various saturation conditions. The simulation results are shown as solid symbol. Relative deviation is defined as (simulation -analytical calculation)/simulation.

The comparison of the analytical calculations with simulation results also shows that the prediction of meniscus height by the macromolecular theory (Kelvin equation) is consistent with simulation results in spite of deviations, the magnitude of which vary with saturation ratio. However, this comparison reveals interesting features of meniscus at the nanoscale. The relative deviation of the analytical calculation in Figure 5.5 is significant especially at the extreme limits of saturation. These deviations are believed to arise for two different reasons: one is from meniscus shape and the other from meniscus size.

In Sec. 5.3, macromolecular theory was used in order to derive the relationship between partial pressure and meniscus height by assuming that the meniscus shape is spherical and the surface tension remains constant regardless of meniscus size. Generally, when capillary condensation drives meniscus formation between two contacting solid bodies, the meniscus has a shape of a pendular ring. From a detailed study of pendular rings (Orr et al., 1975), the meridional profile of the meniscus is acknowledged to be a portion of a nodoid with constant curvature in case of negative capillary pressure; the pressure inside the meniscus is lower than that of the surroundings. The assumption of a circular meniscus profile (toroid) usually causes a negligible difference in shape from nodoid at small amount of meniscus volume (Mayer and Stowe,

2005). As the meniscus volume increases, the difference becomes progressively large because the actual meniscus shape is similar to that of a catenoid, as shown in Figure 5.4d. The toroidal approximation is known to result in the maximum error in that case (Melrose and Wallick, 1967).

The other error at the lower limit is likely due to the limitations of the Kelvin equation. Much work has been done to determine the limits of applicability of the Kelvin equation (Fisher and Israelachvili, 1981; Kohonen and Christenson, 2000; Miyahara et al., 2000) and it is known that the Kelvin equation overestimates the bulk vapor pressure for meniscus radius smaller than 2-4 nm because the surface tension becomes smaller than bulk values for small meniscuses (Brodskaya and Piotrovskaya, 1994; Moody and Attard, 2001; Moody and Attard, 2003). In the theoretical analysis of Sec. 5.3, this suggests that the estimated meniscus height using Kelvin equation becomes much lower than the height of the simulation result at low saturation ratio. The calculation results for the meniscus show that the mean radius curvature of the meniscus is 1.2 nm at the saturation of 0.37. In summary, the analytical prediction based on macromolecular theory shows reasonable results at the intermediate saturation, but it seems less exact for the saturation condition near 1.0 due to a non-spherical meniscus

interface and for a small meniscus with mean radius curvature less than few nanometers because of deviations of surface tension from bulk values.

The meniscus stability is also checked by considering deviation of each configuration from the average density profile. In Figure 5.6, the average profiles at different saturations are compared with these randomly selected snapshots. Each black dot in the snapshots represents an occupied site. Those comparisons demonstrate how the meniscus fluctuates at different saturation ratios. At the saturation of 0.80, the interface of meniscus from the snapshots is continuous and smooth without any significant fluctuations. The particle surface far from the capillary zone is covered by only single occupied sites. However, at the saturation of 0.98, the shape of meniscus fluctuates significantly and the thickness of the adsorbed multilayer far from the meniscus also fluctuates. The large fluctuation at high saturation implies a large fraction of the lattice sites near the interface undergo gas-liquid transition and vice versa, which destabilizes the meniscus.

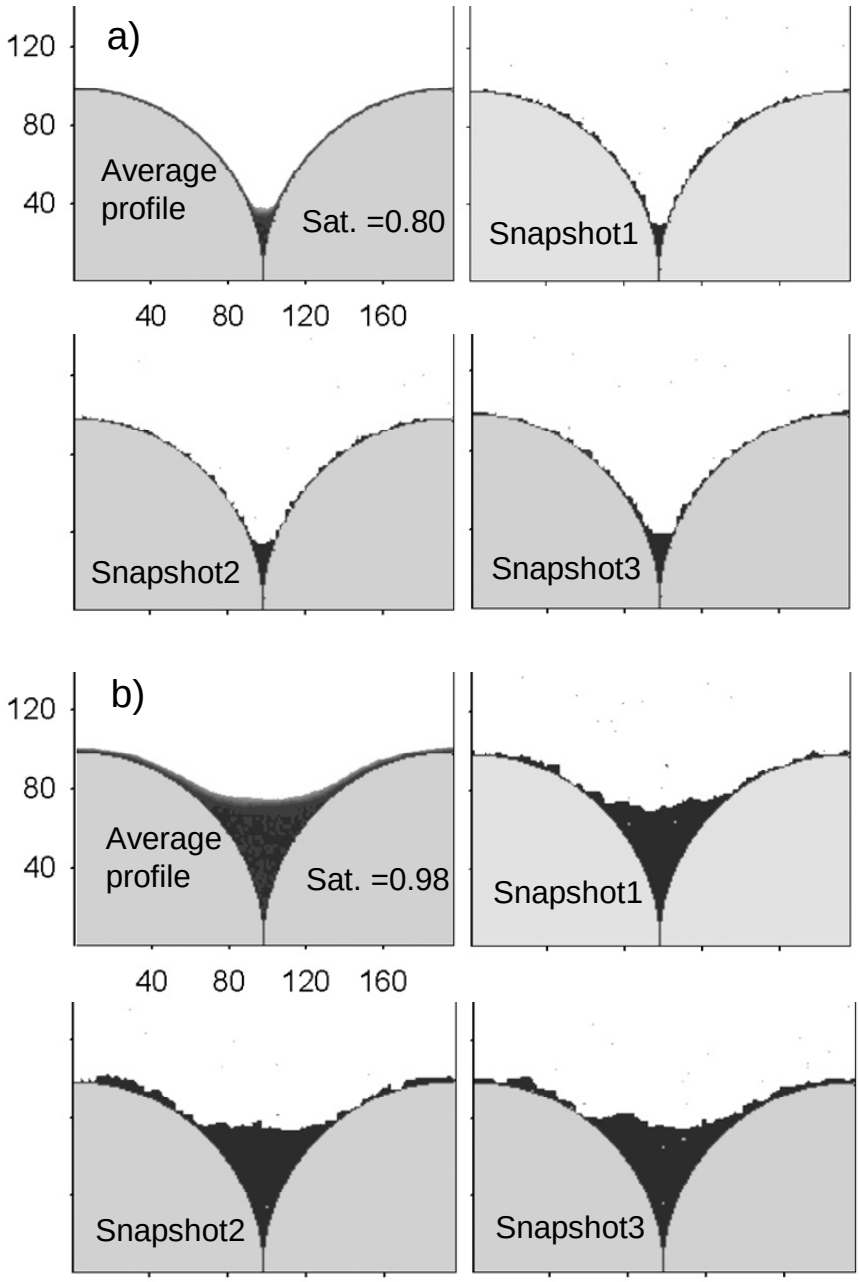

Figure 5.6 Average profiles of the meniscus and individual snapshots selected from equilibrium configurations for two different saturation conditions of 0.80 and 0.98. In these plots, the upper left represents the average profile and other three show the different snapshots.

The effect of particle surface curvature on capillary condensation was investigated by considering elliptically shaped surfaces with different ratios of two major axis lengths (1.5 x R =R', R = R', and R = 1.5 x R'). Figure 5.7 represents how the surface geometry affects the amount of condensate from average profiles of the menisci. For the case of R < R', the capillary zone between two contacting surfaces become narrower than for the spherical surfaces. More condensation is driven in that narrower zone at the same saturation ratio, which results in the elongated meniscus. By contrast, in case of R<R', it results in the decrease of meniscus height. As shown in Figure 5.8, the relative meniscus heights for different curvature of the particle were compared. This effect of the surface shape becomes progressively more significant as the saturation ratio increases, and the differences of the meniscus height between non-spherical and spherical shape are ~3 nm at the saturation ratio of 0.40 and ~11 nm at the saturation ratio of 0.98, respectively. The simulation results for non-spherical cases were also compared with theoretical calculations by equation (10) and the relative deviations are given in Table 5.1. These deviations show a trend similar to what is observed for the spherical surface in Figure 5.5. The deviation becomes significantly large at the lower and higher end of saturation, and also increases as the capillary zone is wider (R>R') at the same saturation. It reflects that the theoretical calculation may not estimate the meniscus height accurately regardless of saturation conditions, in case of meniscus formation on non-spherical particles. The simulation results show that the curvature effect could result in a deviation of approximately 20 % from the meniscus height in the spherical case.

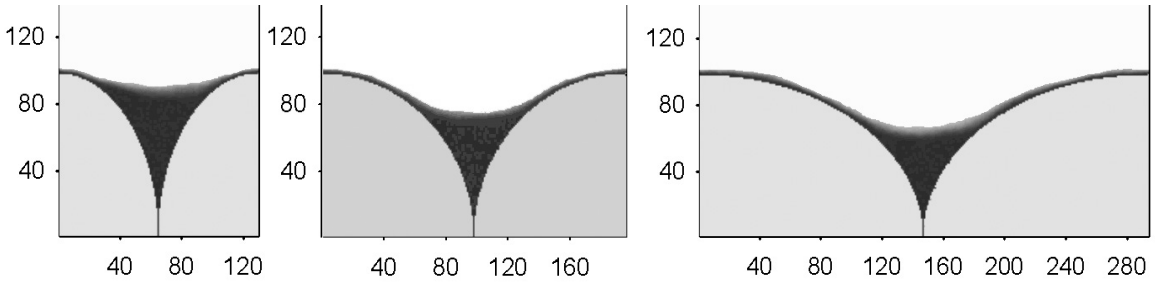

Figure 5.7 Average profiles of the menisci over various geometrical shapes of the particles at a saturation ratio of 0.98. The left image is for the case of *1.5* x *R* =*R*', the middle for *R* = *R*', and the right for *R* = *1.5* x *R*'. Scales in x-y axis show the number of lattice sites with the same lattice size of Figure 5.4.

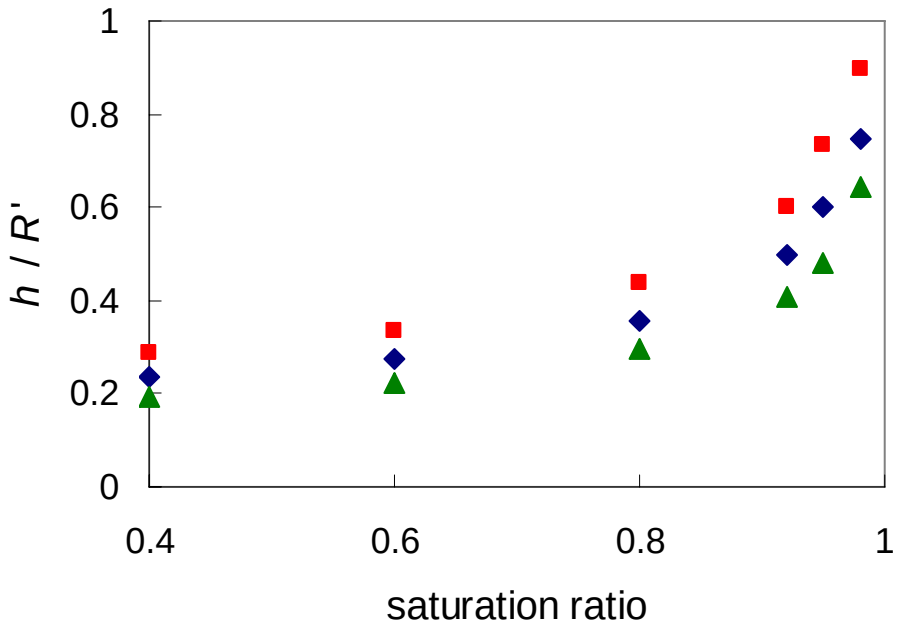

Figure 5.8 Effect of the particle curvature on a relative meniscus height by capillary condensation. Square (■) symbols represents a case of *1.5* x *R* =*R*', diamond (♦) *R* = *R*', and triangle (▲) *R* = *1.5* x *R*', respectively. The meniscus height is defined in the same way as Figure 5.5.

Table 5.1. Relative deviation of simulation results from analytical calculation.

Saturation Ratio	Relative deviation*		
	R=1.5R'	R=R'	1.5R=R'
0.40	0.30	0.27	0.26
0.60	0.24	0.15	0.18
0.80	0.18	0.17	0.13
0.92	0.21	0.17	0.11
0.95	0.22	0.20	0.18
0.98	0.30	0.22	0.21

* Relative deviation is defined as (simulation result-analytical calculation) / simulation result.

Finally, the effect of proximity between two surfaces was explored, which plays a major role in the formation and disappearance of liquid bridges. Equilibrium density profiles are obtained at the specific saturation condition by changing the surface-surface distance (d=4, 6, and 8 lattice spacings) and compared with the case of two contacting surfaces. In Figure 5.9, average meniscus profiles for different gas spacings at a saturation ratio of 0.60 were illustrated and it is observed that a small change of the gap space significantly affects the meniscus formation. The detailed gap space dependence of the relative meniscus height is shown in Figure 5.10, in which each relative meniscus height is obtained from various average meniscus profiles at different saturation ratios and different gap spacings. The gap space is known to generally invoke a hysteresis effect of capillary condensation and, as the space becomes larger, the first onset of the meniscus happens at higher saturation condition. The comparison between the case of d=0 and d≠0 shows that the effect of the surface-surface distance is mainly significant as the saturation condition decreases and becomes less important at higher saturation above 0.90. The results obtained at the saturation ratio of 0.90 show that deviations from the case of contacting surfaces are less than 10%. At the longest distance (d=8 lattice spacings, ~6 nm) of this simulation, a sudden formation of meniscus is observed near the saturation of 0.70 and its height is 14 lattice spacings equivalent to ~10 nm. As the

surface-surface distance decreases, the first meniscus formation starts at lower saturation but the difference of meniscus height from the case of two contacting surfaces is significant under the saturation of 0.90.

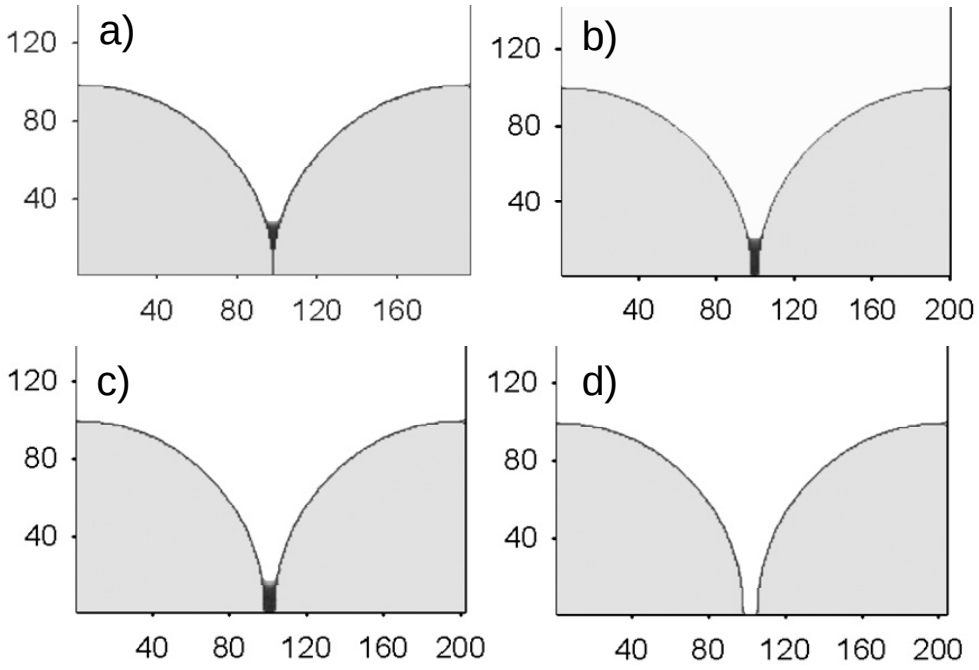

Figure 5.9 Average profiles of the menisci for different gap spaces between particles at the saturation ratio of 0.60. a) is for the gap space of 0 lattice, b) is for 4 lattices, c) is for 6 lattices, and d) is for 8 lattices. Scales in x-y axis show the number of lattice sites with the same lattice size of Figure 5.4.

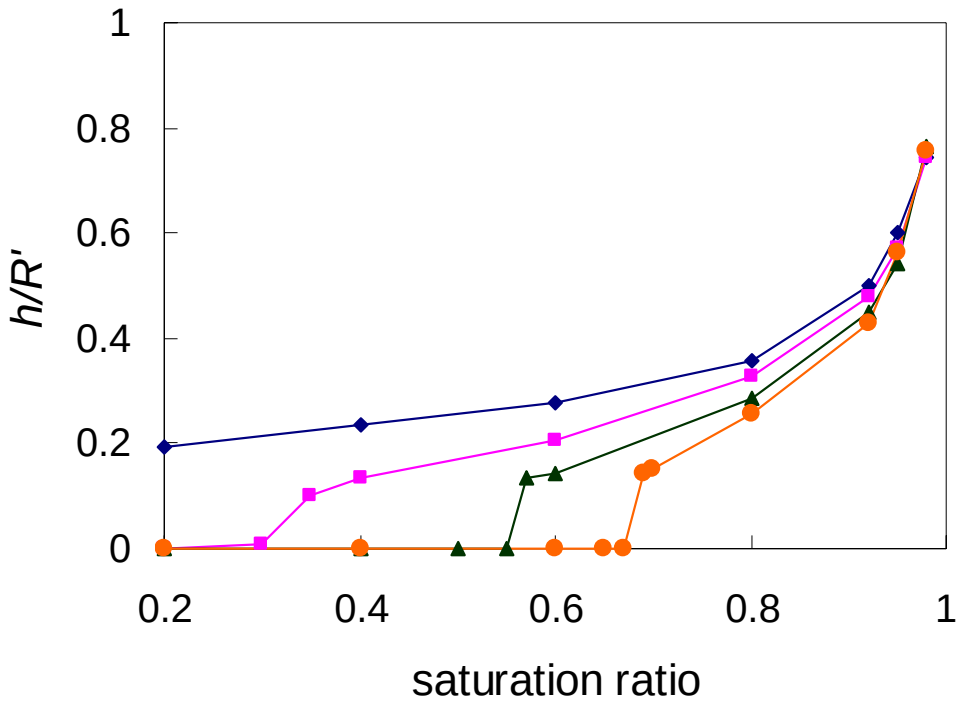

Figure 5.10 Effect of gap space between particles on a relative meniscus height by capillary condensation. Diamond (♦) symbols represent a case of no gap spacing, square (■) 4 lattice spacings, triangle (▲) 6 lattice spacings, and circle (●) 8 lattice spacings with one lattice size of 7.17A.

Based on simulation results for various possible geometries, it is hypothesized that the conditions for capillary condensation between two curved surfaces are dependent on not only thermodynamics but also the nanoscale dimensions including sphericity of the surface and the surface-surface distance. The curvature effect significantly affects the meniscus height at the higher saturation close to 1.0 and the surface-surface distance results in the decrease of meniscus height or even the disappearance of the meniscus at lower saturation under 0.9.

5.6 Concluding remarks

I presented theoretical analyses and computer simulations for liquid condensation on two curved surfaces. This study is motivated by the experimental study in chapter 4, in which the thickness of the coated silica layer on titania nanoparticle was found to be strongly dependent on the geometrical shape of the capillary zone as well as the saturation conditions. In the experimental study, it is very hard to control the shape and size of nanoparticle in an exact manner. Thus, GCMC simulation of a simple lattice gas model was utilized in order to examine the characteristics of the liquid meniscus by considering various saturation conditions and possible capillary zone geometries. The

particle size, the energetic parameters, and the fluid-surface interactions were determined in order to simulate the wetting phenomena of TEOS on the surface of titania nanoparticle in an approximate but physically meaningful way.

This combined study of analytical calculations and simulation results for capillary condensation on two contacting particles shows that meniscus height generally increases as the saturation ratio increases and the change of the height is more drastic near the saturation of 1.0. It shows that the saturation condition could be tuned in order to obtain the specific dimension of the meniscus. The comparison of the analytical calculation with the simulation result presents a relative validity of Kelvin equation based on macromolecular properties. The analytical prediction shows reasonable results at the intermediate saturation, but it seems less exact for the saturation condition near 1.0, likely because of the non-sphericity of the meniscus interface and for small menisci with mean radii of curvature less than few nanometers, possibly because of deviations of surface tension from bulk values.

The effect of the confined geometry was also investigated in terms of the surface curvature and the gap space. The curvature change results in a change in the width of the capillary zone between two surfaces, which affects the amount of condensate and the meniscus dimensions. This effect becomes more important as the saturation ratio

increases. The gap distance also shows a significant effect at lower saturation but this effect becomes less as the saturation approaches the saturation of 1.0. From the above results, it is concluded that the combination of these two effects is not negligible. Experimental conditions should be manipulated carefully in order to obtain the meniscus formation on various mixed particles with different shapes and gap distances among particles.

VI. PHOTOCATALYTIC ACTIVITY OF SURFACE-MODIFIED TITANIA NANOPARTICLE MIXTURE CONSISTING OF ANATASE AND RUTILE PAHSES

6.1 Abstract

Photocatalytic activity of bi-phase (anatase and rutile) titania nanoparticles with various phase compositions and surface-modified titania nanoparticles with silica layers was investigated by following photodegradation of methylene blue in an aqueous solutions. The performance of titania nanoparticles as photocatalysts was analyzed based on pseudo first-order reaction kinetics. Preliminary experimental results show that the physically mixed sample of separate anatase and rutile has enhanced photocatalytic activity. This effect is maximized when the mass ratio of anatase and rutile is 4:1. The surface-modified 4:1 anatase to rutile titania nanoparticles were prepared by a surface modification process. The original mixture samples were treated at various saturation conditions and, among those samples, the sample treated at a saturation ratio of 1.1 shows even higher photoactivity than the original mixture sample.

6.2 Introduction

Semiconductor photocatalysis has attracted much attention because it is inexpensive, nontoxic, and convenient to use (Fox and Dulay, 1993). Furthermore, semiconductor particles recovered by filtration, centrifugation, or when immobilized in a fluidized bed reactor retain much of their native activity after repeated catalytic cycles. Among various possible semiconductors such as metal oxides (TiO_2, ZnO, CeO_2, …) and metal sulfide (CdS, ZnS, …), titanium dioxide (TiO_2), also known as titania, has been shown to be the most suitable for the photodegradation of toxic organic molecules due to its excellent photocatalytic performance with maximum quantum yields (Hoffmann et al., 1995).

Titanium dioxide has two principal catalytically active phases (anatase and rutile). The anatase form appears to be more photoactive and practical for widespread environmental application such as water purification, waste water treatment, and air purification (Stafford et al., 1996). However, commercial titania powder P25 from Degussa, which shows high activity for many kinds of photocatalytic reactions, consists of a mixture of the two phases. Its interesting high activity has motivated further research into the mixed phases. Ohno et al. (Ohno et al., 2001) studied the morphology of the anatase and rutile phases in P25 by measuring the TEM images and the diffuse

reflectance spectra. It was concluded that the anatase and rutile exist separately in the P25 and the synergy effect is expected if rutile and anatase particles are in physical contact. Sun et al. (Sun et al., 2003) investigated various combinations of titania catalysts having different particle sized and impurity contents. Their experiments showed that the synergistic effect between anatase and rutile phase was not universal but, related to the relative Fermi levels of two different phases and the shape of the particle. This synergistic effect is usually explained by a model that the transfer of electrons from anatase to a lower energy rutile electron trapping site serves to reduce the recombination rate of anatase, leading to more efficient catalytic reactivity (Bickley et al., 1991). This hypothesis was investigated by various empirical measurement techniques such as electron paramagnetic resonance spectroscopy (Hurum et al., 2003) and photoluminescence spectroscopy (Nakajima et al., 2005), but an exact explanation of enhanced photoactivity in the mixed phase is still controversial. The synergistic effect was also observed in mechanical mixtures of two phases (Wu et al., 2004) and two phase mesoporous films (Yu et al., 2002) which are prepared by sol-gel method followed by calcination.

Recently, a new process was developed to make interparticle connections between nanoparticles using capillary condensation and surface reaction. From this

process, surface-modified titania nanoparticles with a bridge-shaped silica layer were obtained, the thickness of which is tunable by adjusting the experimental conditions. In the present study, the photocatalytic activity of bi-phase titania nanoparticles with various phase compositions is investigated and effect of the silica layer between particles on the photocatalytic activity is tested.

6.3 Experimental

Two different phases of titania nanoparticles were used: anatase and rutile, which are commercially available. The anatase phase (99.9%, Alfa Aesar Co.) is spherical and its average size is ~35 nm from the manufacturer's specifications. The rutile phase (99.5%, Sigma Aldrich Co.) has a needle-like shape with the dimensions of approximately 10 nm by 40 nm as determined from analysis of transmission electron microscope images. In order to prepare the mixture of two phases with various compositions, the titania particles were dispersed in distilled water, sonicated for 30 min, and dried in the oven at 100 °C for 12 hours. After drying the particles, I ground the chunk of powders using glass beads (Cole Parmer Instrument Co.) of 1.0 mm and filtered

them using a series of sieves. Some of the samples were modified by the capillary condensation process, as described in Chapter 4.

To evaluate the photocatalytic activity of the samples, the decomposition behavior of methylene blue (MB, $C_{16}H_{18}N_3S$, Sigma Aldrich Co.) in water was performed at room temperature because MB has strong adsorption characteristics on the surfaces of many solid particles, good resistance to light degradation and a well defined optical absorption. The photodegradation of MB in an aqueous suspension of catalyst was carried out in an annular quartz photocatalytic reactor (Ace Glass Inc. No. 7863) as shown in Figure 6.1. The suspension for photocatalytic reaction was prepared by dispersing 5 mg catalyst and 500 ml of MB solution, 15 ppm MB in water, for 30 minutes in an ultrasonic bath (Branson Ultrasonic Corp., Model 5510). The suspended solution was transferred into the glass reactor and agitated by a magnetic stirrer at the bottom for 30 minutes, and air was pumped into solution continuously at the rate of 20 cc/min. The 450 W UV immersion lamp (Ace Glass Inc., No. 7825-34) was used as radiation source and a Pyrex filter (Ace Glass Inc., No. 7740) was placed between the lamp and the reactor to filter out the far- and mid-UV bands of the lamp emission spectrum. A thermometer and a condenser are used to observe the solution temperature and to cool the volatile vapor, respectively. Reaction temperatures were maintained at 35-40 °C.

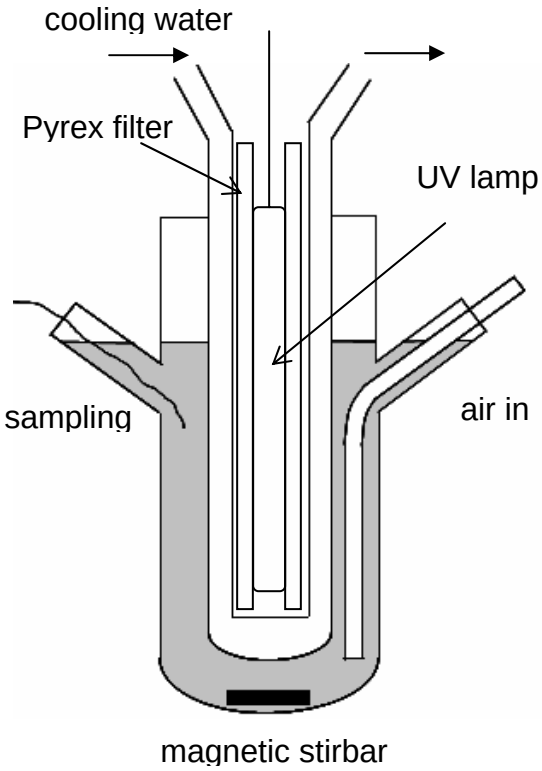

Figure 6.1 Schematic diagram of the annular quartz photocatalytic reactor.

Samples were withdrawn at every 10 min up to 90 min. In order to eliminate the effects of particles on photoabsorption, samples were centrifuged before MB concentrations were measured.

The change of MB concentration was determined with a UV-visible spectrophotometer (Varian Inc., Cary 50). The calibration curves were prepared using the solutions of known concentrations with an analytical wavelength of 609 nm. Although the maximum adsorption wavelength of MB typically appeared at 660 nm, it was often shifted during the reaction. Therefore, a wavelength of 609 nm was selected for the measurement of MB concentration in these experiments. The Brunauer-Emmett-Teller (BET) surface area of the catalysts was measured on a surface area analyzer (Quantachrome Instruments, Nova 1200) at 77 K using liquid nitrogen. X-ray diffractometer (XRD, Bruker AXS D8, Advance) with CuKα was used to characterize the phase of the catalysts and the 2θ was varied in the range from 20° to 50°. The morphology of the mixed titania particles was examined using a Hitachi H600 transmission electron microscopy (TEM) and Jeol 2100F field emission TEM.

6.4 Results and discussion

Two principal phases (anatase and rutile) of titania nanoparticles used in the present study were analyzed using X-ray diffraction (XRD) analysis, as shown in Figure 6.2. Commercial titania nanoparticles from Alfa Aesar Co. and from Sigma Aldrich Co. were confirmed to be anatase and rutile phases respectively by the XRD results, which were consistent with the manufacturer's specifications.

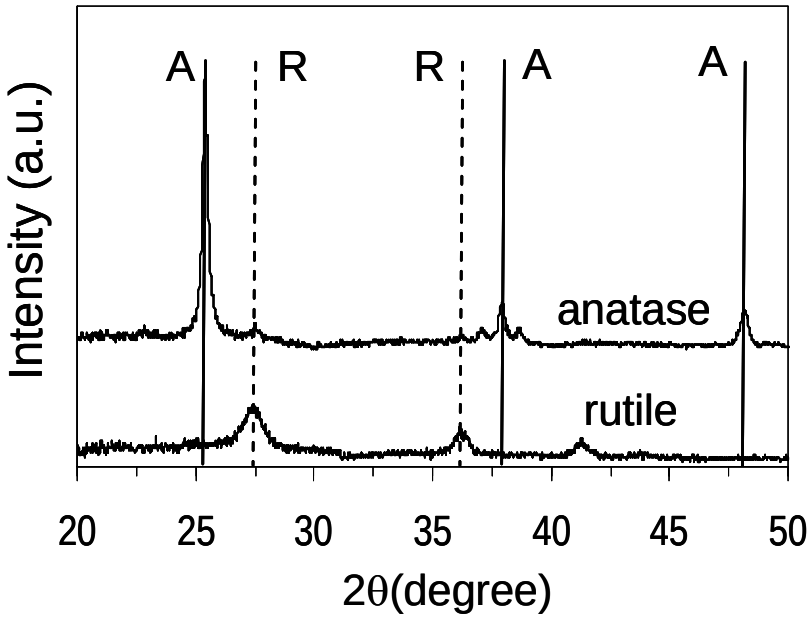

Figure 6.2 XRD of the pure anatase (A) and rutile (R) phases used in this study.

Two phases have different shapes based on manufacturer's specification and the difference was observed by TEM photographs in Figure 6.3 (a) and (b). The anatase is spherical and the rutile needlelike. TEM photographs of the two phase mixtures with different compositions show that anatase and rutile nanoparticles are well mixed at nanoscale, as shown in Figure 6.3 (c). Additional TEM images of different compositions are given in Appendix D. The BET surface areas of various titania samples were measured and listed in Table 6.1. The surface areas of pure anatase and pure rutile were 42 and 152 m^2/g, respectively. The surface areas of bi-phase mixtures with different compositions of anatase were also measured and their values decrease with the increase of anatase amount, which represents that the original particle size and structure were maintained after the physical mixing by sonication. The comparison of the surface areas between an original mixture sample (sample E in Table 6.1) and a surface-modified sample (sample F in Table 6.1) shows that the surface modification process does not significantly affect the surface area of nanoparticles. TEM photographs of the original mixture sample and the modified sample are shown in Figure 6.3 (c) and (d).

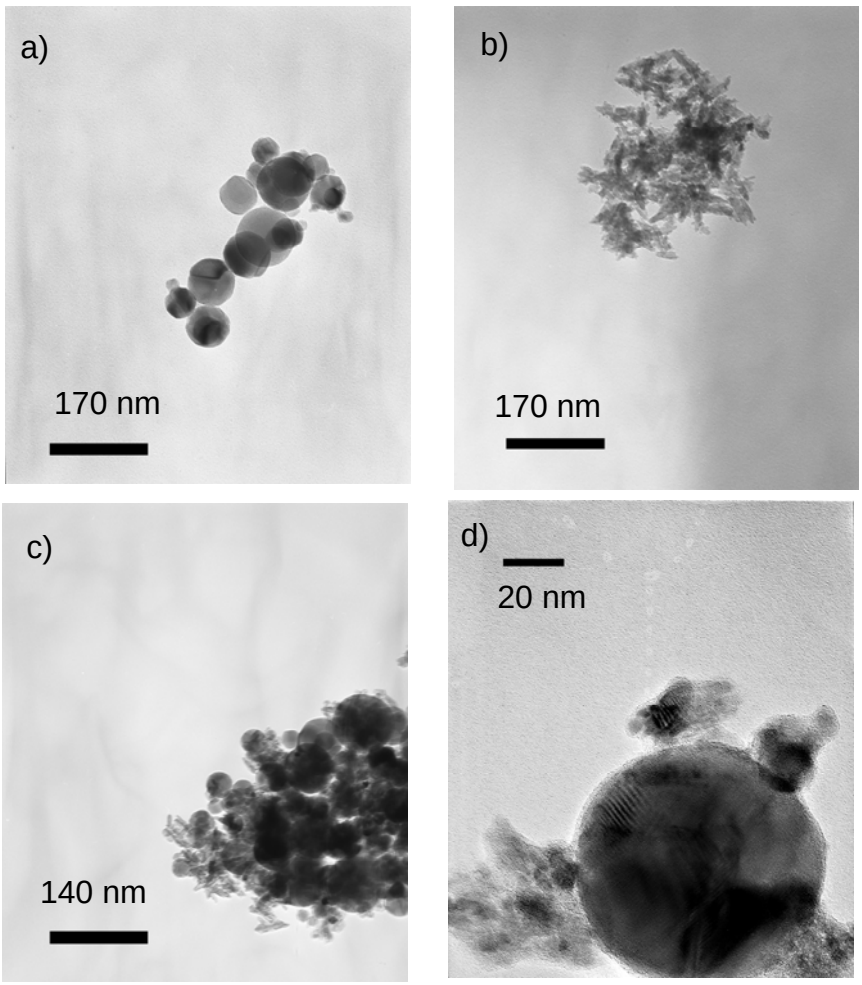

Figure 6.3 TEM photographs of a) pure anatase, b) pure rutile, c) anatase-rutile mixture (4:1), and d) modified mixture sample at a saturation ratio of 1.1.

Table 6.1 Selected properties of titania samples used in the present study.

	sample	Titania (%)	BET surface area (m^2/g)	Avg. particle diameter (nm)[c]
A	Pure anatase (spherical shape)	99.9[a]	42	37
B	Pure rutile (needle shape)	99.5[a]	152	9
C	Mixture (A:B=1:1)		88	17
D	Mixture (A:B=3:1)		63	24
E	Mixture (A:B=4:1)		53	28
F	Modified E[b]		52	29

[a] From manufacture's specifications

[b] Modified at a saturation ratio of 1.1

[c] Equivalent diameter calculated from the BET surface area

The performance of titania as photocatalyst for the photodegradation of MB was briefly investigated using an annular quartz photocatalytic reactor and UV light source system. It has been confirmed that the rate of photodegradation of organic compounds generally follows the pseudo first-order reaction kinetics for low concentration of organic (Matthews, 1988; Matthews, 1989)

$$-\ln(\frac{C}{C_0}) = kt \qquad (1)$$

where C_0 is an initial concentration, C is a concentration at given UV irradiation time, k is reaction rate constant, and t is UV irradiation time. According to equation (1), a plot of the logarithmic value of concentration vs. time should be a straight line whose slope is k.

Results of the photodegradation of MB with different samples of titania as catalysts are summarized in Table 6.2. Generally, the rutile phase of titania is known to be almost inactive.(Herrmann, 1999) However, in the photo degradation of MB, it was observed in the previous research (van Dyk and Heyns, 1998) that the quantitative differences between the photocatalytic activities of rutile and anatase are not significant. The present experimental results show that the photocatalytic activity of rutile phase is close to that of anatase phase, as shown in Table 6.2, because the surface area of rutile is 3 times higher than anatase phase.

Table 6.2 Reaction rate constants of prepared samples.

No	Titania nanoparticles	Saturation ratio	k (min^{-1})
A	Pure anatase		0.0061 ± 0.0002
B	Pure rutile		0.0056 ± 0.0002
C	A:B=1:1		0.0059 ± 0.0001
D	A:B=3:1		0.0067 ± 0.0001
E	A:B=4:1		0.0076 ± 0.0001
F[a]	A:B=4:1	1.1	0.0082 ± 0.0003
G[a]	A:B=4:1	0.84	0.0067 ± 0.0004
H[a]	A:B=4:1	1.7	0.0043 ± 0.0005

[a] Samples were modified at the given saturation condition by the surface modification process

Some experimental studies (Datye et al., 1995; Ohno et al., 2001) showed that the commercial titania P25 from Degussa contains anatase and rutile phases in a ratio of about 3:1 and its high photocatalytic activity (synergistic effect) is proposed to results from the physical contact between two phases. In the present study, I prepared anatase-rutile mixture samples with various compositions and obtained the reaction rate constants from concentration profiles as a function of time in order to determine the photocatalytic activities of various samples. Figure 6.4 shows a typical plot of the logarithmic value of concentration as a function of time for various anatase and rutile mixtures while the total mass concentration of titania was fixed. In this system, the synergistic effect seems to be maximized when the ratio of anatase and rutile is 4:1.

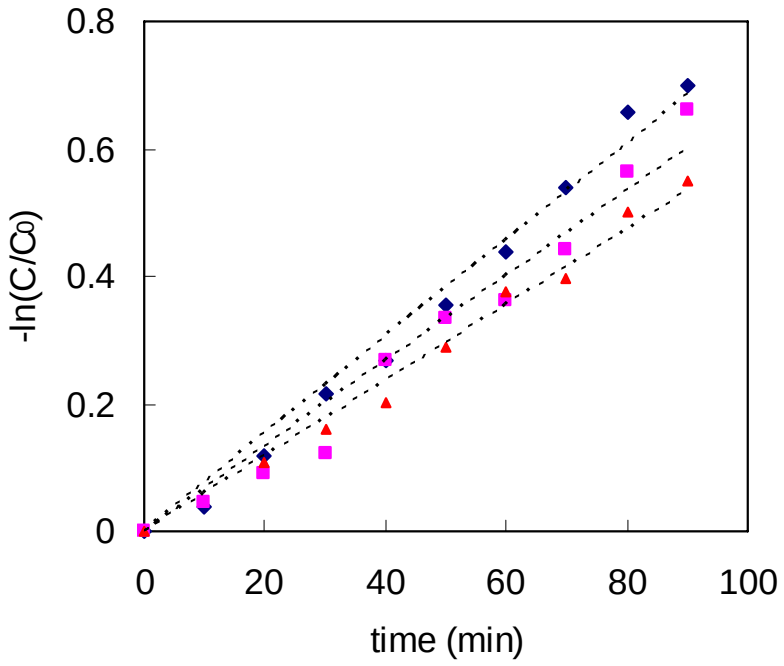

Figure 6.4 Plot of logarithmic values of concentration as a function of time for various anatase-rutile mixtures: diamond (♦) is 4:1, square (■) 3:1, and triangle (▲) 1:1.

For the sample consisting of anatase and rutile in the ratio of 4:1, I used the surface modification process described in Chapter 4 and formed silica layers at different saturation ratios to make interparticle connections between nanoparticles with various thickness. The photocatalytic activities of these modified samples were also characterized by the calculation of reaction rate constants. Based on the previous study about the surface modification process, the bridge-shaped silica layer dominantly forms

in the space between nanoparticles up to the saturation ratio of ~ 1.0, creating in interparticle connections. A uniform silica layer forms on the entire surface at a saturation ratio of 2.0. As shown in Figure 6.5, when the bridge-shaped silica layer was formed of sufficient thickness to increase the interparticle connections at the saturation ratio of 1.1, the photocatalytic activity of the surface-modified sample (sample F in Table 2) increased compared to that of the original mixture sample (sample E in Table 2) by ~8 %. However, if a thick silica layer covers all the surface of titania particles (at the saturation ratio of 1.7) or a very small amount of silica does not form sufficient interparticle connections (at the saturation ratio of 0.84), the photocatalytic activity seems to be significantly decreased. The effect of silica loading on single phase titania nanoparticles was already observed in some studies (Anderson and Bard, 1995; van Dyk and Heyns, 1998; Li et al., 2005). They discussed that the reason of the photocatalytic activity increase might be due to the increased adsorption amount of MB on silica or the increased dispersion stability. However, the exact reason of the photocatalytic activity change is still controversial.

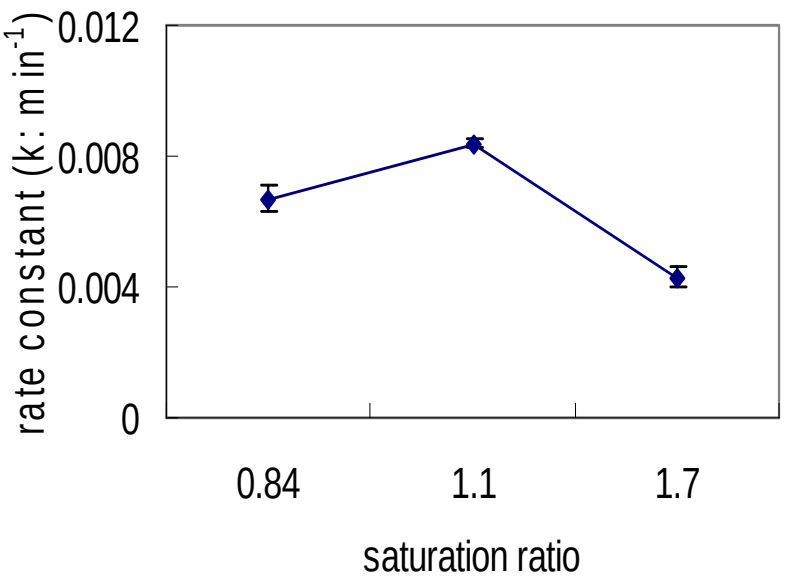

Figure 6.5 Reaction rate constant variation of surface modified titania mixtures at different saturation conditions. Anatase-rutile mixtures (4:1) were modified by the capillary condensation process at different saturation ratios and photocatalytic activities of the modified samples were measured.

6.5 Conclusions

The photocatalytic activity of various bi-phase titania mixtures and surface-modified mixtures were investigated by using an annular quartz photocatalytic reactor and UV light source system. Anatase and rutile titania nanoparticles used in the present study were characterized by XRD analysis and BET surface area measurement. An apparent synergistic effect was observed for a sample consisting of anatase and rutile in a ratio of 4:1, which shows the highest photocatalytic activity among the bi-phase mixture samples prepared by sonication. The surface-modified bi-phase titania sample, which was treated at a saturation ratio of 1.1, shows even higher photocatalytic activity than original bi-phase mixture sample. These results represent that the specific amount of silica layer on titania nanoparticles can enhance the photocatalytic activity of original titania.

VII. Conclusions

7.1 Summary

Capillary condensation on metal oxide nanoparticles was studied in a controlled manner. A tubular flow chamber was designed to obtain uniform saturation conditions at the location of the particle sample. Results from a study incorporating a computational dynamics simulation of the chamber showed that there is a large region with constant saturation condition near the end of the chamber. Thus, the control of chamber wall temperature can lead to various saturation conditions and result in heterogeneous condensation of vaporized precursor on nanoparticle samples. The combinations of the chamber, temperature control units, precursor vaporization unit, and TCD detector, can be considered as a new process for forming interconnections between metal oxide nanoparticles.

Using this process, titania nanoparticles interconnected by silica layers were prepared at a variety of saturation conditions. The silica layer was formed dominantly in the capillary zone between particles and, in qualitative agreement with predictions made using the Kelvin equation, the thickness of silica layer increased as the saturation ratio increased up to a saturation ratio of 1.0. However, in supersaturated conditions

(saturation ratio > 1.0), the change of the silica layer thickness was not directly proportional to the change in saturation ratio and a uniformly thick silica layer was observed at high saturation ratio of 2.0.

In this experimental study, it is very hard to investigate effects of the nanoscale geometries of the particles and the proximity of two particles on saturation conditions in an exact manner. Thus, a GCMC simulation of a simple lattice gas model was developed to examine the characteristics of the liquid meniscus formed between nanoparticles. Simulation results show that the curvature of the particle surface and the proximity of the two particles lead to the spatial change of capillary zone, and these factors affect the amount of condensate and meniscus dimensions.

This combined study shows that surface modification by capillary condensation can be used to obtain nanoparticles interconnected by a second species and the amount of the other species is also controllable by changing experimental conditions. However, particle shapes and the gap space between particles significantly affect the required saturation condition for capillary condensation and the experimental conditions need to be adjusted to consider these effects.

The application of the proposed process was also considered by measuring photocatalytic activity change before and after the surface modification. For a bi-phase

anatase and rutile titania nanoparticle mixture, the surface-modified sample with strong interconnection by silica showed a higher ability to degrade methylene blue in aqueous solution than the original unmodified sample. However, this silica effect seemed to reduce the photoactivity if a thick silica layer covers the entire surface of the sample or very small amount of silica does not form the enough interparticle connections. This result suggests a specific amount of silica loading on titania nanoparticles can enhance the photocatalytic activity of original titania and the proposed process can be applicable to vary the amount of silica on the titania nanoparticles.

7.2 Future work

In this dissertation, titania nanoparticles and TEOS were used as the original sample and precursor, respectively. However, the proposed process is based on condensation and surface reaction of a precursor, and the thickness of the layer mostly depends on saturation conditions and the wetting characteristics of precursor on the particle surface. This fact suggests that different precursors can be used to form a layer of various materials on the surface of titania. One of the challenging precursor choices is titanium tetraisopropoxide (TTIP), which is common precursor for the production of nanosized titania particles in an aerosol reactor using vapor hydrolysis (Seto et al., 1995;

Chan et al., 1999). However, it is known that the hydrolysis reaction of TTIP is so rapid even at room temperature and TTIP vapor is not likely to form stable meniscus in the capillary condensation process described in this dissertation. Recently, some researchers reported that titania thin films can be synthesized by an evaporation-induced self-assembly process where acetylacetonade and HCl are used as hydrolysis inhibitors (Soler-Illia et al., 2002; Kartini et al., 2004). This mixture solution could be a possible precursor to obtain a titania layer by homogeneous condensation and prepare bi-phase (rutile and anatase) titania materials. Photoactivity of this composite is also interesting topic as discussed in Chapter 6.

The enhancement of photocatalytic activity by mixing two different nanoparticles is also an interesting topic. In this study, bi-phase titania nanoparticles were used to investigate the effect of surface modification on photocatalytic activity but it is well known that a combination of titania nanoparticles with different semiconductor particles such as CdS and SnO_2 leads to an enhancement of photodegradation in a specific organic chemical system (Carp et al., 2004). This coupled system has been investigated in various forms such as colloid mixture, immobilezed film, and slurry solution (Spanhel et al., 1987; Bedja and Kamat, 1995; Vinodgopal et al., 1996). Thus, semiconductor particles coated with other semiconductor films with optimal thickness

may result in efficient charge separation. Of course, geometry of particles, characteristics of surface, and particle size play a significant role in interparticle electron transfer. The change of photocatalytic properties in the coupled system is believed to rise from interparticle electron transfer and beneficial aspects of semiconductor particles coated with other semiconductor material for photocatalysis are recommended as subjects of future work by combining the present studies given in Chapter 4 and Chapter 6.

APPENDIX A ESTIMATION OF TEOS PROPERTIES BASED ON CORRELATION METHOD

The TEOS critical properties are estimated from Lydersen's correlation, which is based on the group contribution method. With this estimation, the errors are normally less than 2 percent for critical temperature and 5 percent for critical pressure except for high molecular weight compounds (>1000). Viscosity, heat capacity, and thermal conductivity can also be estimated by corresponding-states methods. Each property was calculated by the following equations.

$$T_c = \frac{T_b}{0.567 + \sum \Delta T - (\sum \Delta T)^2} \quad [K] \tag{B1}$$

$$P_c = \frac{M}{(0.34 + \sum \Delta p)^2} \quad [atm] \tag{B2}$$

where T_b is the boiling temperature, M is molecular weight, and ΔT and ΔP are evaluated by group contributions. Viscosity is calculated by equation (B3), Thodos & coworkers' correlation,

$$\eta\xi = 4.610\, T_r^{0.618} - 2.04\, e^{-0.449\, T_r} + 1.94\, e^{-4.058\, T}$$
$$, \ \xi = T_c^{1/6} M^{-1/2} P_c^{-2/3} \tag{B3}$$

with η in μP, T_c in kelvin, and P_c in atmospheres. Thermal conductivity and heat capacity are also obtained by equation (B4) and (B5), Harrison and Seaton correlation and the Eucken correlation respectively.

$$C_p^0 = a_1 + a_2 C + a_3 H + a_4 O + a_{11} Si \quad \text{(B4)}$$

$$\lambda_G = (C_v + 4.47)(\eta / M) \quad [cal/(cm \cdot s \cdot K)] \quad \text{(B5)}$$

where a1, a2, a3, a4, and a11 are parameters given in literature14, C, H, O, and Si are the numbers of each atom in the molecule, η is the low-pressure gaseous viscosity, P, and Cv is heat capacity at constant volume, cal/(mol·K).

APPENDIX B ADDITIONAL TEM IMAGES OF ANATASE AND RUTILE MIXTURES OF DIFFERENT COMPOSITIONS

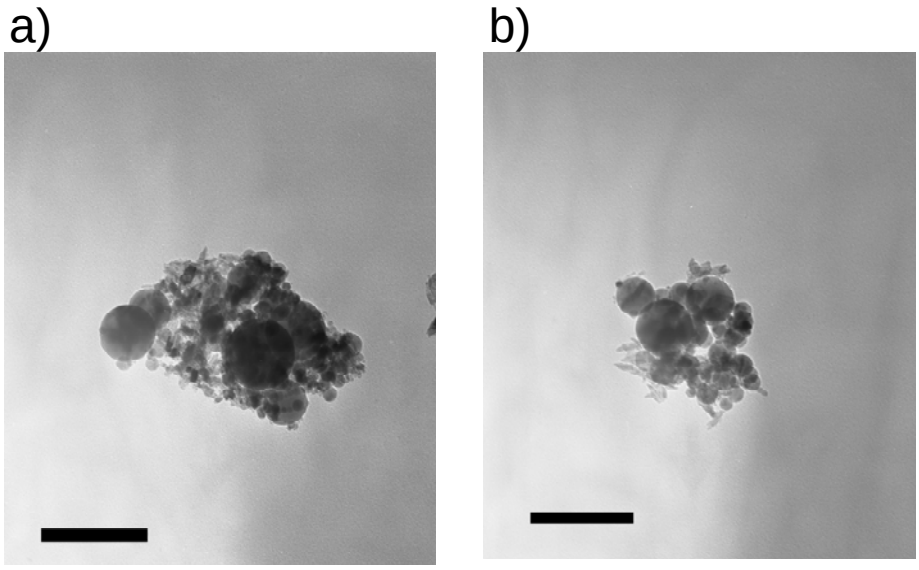

Figure B.1 TEM images of anatase and rutile mixture a) anatase: rutile= 1:1 and b) anatase: rutile=3:1.

APPENDIX C STANDARD OPERATING PROCEDURE OF THE CAPILLARY CONDENSATION PROCESS

1. Put a precursor solution into a bubbler
2. Assemble the bubbler and place it in a water bath
3. Put a sample on the holder and fix it by the clip
4. Turn on the power strip and a immersion heater, and set the temperature of the bath at 81.1 'C
5. Turn on a TCD unit and a recorder
6. Turn on the power controllers for heating tapes
7. Set the temperature of PID controller
8. Open valves of argon cylinder
9. Purge the chamber with argon gas until the temperature of chamber reaches the objective temperature (1~2 hours)
10. Check the TCD recorder in order to verify the stable baseline
11. Change a valve from the purge line to bubbler and start supplying precursor vapor
12. Let the precursor vapor flow for 2 hours
13. Keep recording TCD measurements

14. Close the valve on the bubbler and open the valve of the purge line

15. Turn off the immersion heater

16. When the TCD measurement show that there is no precursor in the flow, turn off the TCD unit

17. Turn off the power controllers for heating tapes and power strip

18. Close the argon cylinder

19. Obtain the sample after the overnight

APPENDIX D STANDARD OPERATING PROCEDURE FOR PHOTOCATLYTIC REACTION OF TITANIA PARTICLE IN METHYLENE BLUE SOLUTION

I. Preparation of methylene blue solution

1. Weigh 0.15g of methylene blue into a flask
2. Add 100mL of water to make a desired concentrated solution
3. Mix the solution for 30 min
4. Keep ~20 mL of solution for later calibration
5. Dilute the solution to obtain the final desired concentration and leave some part of the dilution water to wash down the remainder of the solution for the reactor (Dilute 5mL MB solution/395 mL water, add 100mL later)
6. Mix the solution for 20 min
7. Add titania particles (10mg) to the solution
8. Put the titania-suspended solution in the sonicator for 30 min

II. Photoactive reaction

1. Assemble the reactor
2. Turn on cooling water line
3. Adjust water flow rate

4. Check the cooling water temp

5. Add ice to the bucket - Check cooling water temp

6. Prepare and label centrifuge tubes and vials

7. Pour 395 mL of MB solution into the reactor

8. Wash down the flask with 100mL of water to finish 15ppm sol-n

9. Cover the solution outlet with parafilm

10. Turn on the stirrer

11. Mix for 20 min

12. Withdraw a sample (~10mg) before turning on the lamp

13. Turn on the compressed air

14. Leave the cooling water running, turn on the lamp (record temp)

15. Add ice to the bucket within 5 min of warmup (record temp)

16. Withdraw a sample after the 10 min warmup

17. Restart the timer and withdraw a sample every 10 min for 90 min (record temp)

18. Clean the syringe and take temp every time you withdraw a sample

19. Turn off the lamp for cooldown

20. Clean the reactor

21. Clean out the gas tube by sticking it in the bucket and running it

Reference

Adams, M. J., Johnson, S. A., Seville, J. P. K. and Willett, C. D. (2002). "Mapping the influence of gravity on pendular liquid bridges between rigid spheres." Langmuir **18**(16): 6180.

Adamson, A. W. (1990). Physical chemistry of surfaces. New York, Wiley.

Adamson, A. W. and Gast, A. P. (1997). Physical chemistry of surfaces. New York, Wiley.

Albano, E. V., Binder, K. and Paul, W. (1997). "Capillary condensation in the two-dimensional lattice gas: A Monte Carlo test of fluctuation corrections to the Kelvin equation." Journal of Physics a-Mathematical and General **30**(10): 3285.

Alekabi, H. and Demayo, P. (1986). "Surface Photochemistry - on the Mechanism of the Semiconductor Photoinduced Valence Isomerization of Hexamethyl-Dewar Benzene to Hexamethylbenzene." Journal of Physical Chemistry **90**(17): 4075.

Allen, M. P. and Tildesley, D. J. (1987). Computer simulation of liquids. Oxford New York, Clarendon Press; Oxford University Press.

Anderson, C. and Bard, A. J. (1995). "Improved Photocatalyst of Tio2/Sio2 Prepared by a Sol-Gel Synthesis." Journal of Physical Chemistry **99**(24): 9882.

Anderson, J. S., Roberts, M. W. and Stone, F. S. (1972). Reactivity of solids: proceedings of the Seventh International Symposium on the Reactivity of Solids, Bristol, 17-21 July 1972. London, Chapman and Hall.

Anisimov, M. P., Hameri, K. and Kulmala, M. (1994). "Construction and Test of Laminar-Flow Diffusion Chamber - Homogeneous Nucleation of Dbp and N-Hexanol." Journal of Aerosol Science **25**(1): 23.

Augugliaro, V., Palmisano, L., Sclafani, A., Minero, C. and Pelizzetti, E. (1988). "Photocatalytic Degradation of Phenol in Aqueous Titanium-Dioxide Dispersions." Toxicological and Environmental Chemistry **16**(2): 89.

Barbe, C. J., Arendse, F., Comte, P., Jirousek, M., Lenzmann, F., Shklover, V. and Gratzel, M. (1997). "Nanocrystalline titanium oxide electrodes for photovoltaic applications." Journal of the American Ceramic Society **80**(12): 3157.

Bates, S. P., Gillan, M. J. and Kresse, G. (1998). "Adsorption of methanol on TiO2(110): A first-principles investigation." Journal of Physical Chemistry B **102**(11): 2017.

Bates, S. P., Kresse, G. and Gillan, M. J. (1998). "The adsorption and dissociation of ROH molecules on TiO2(110)." Surface Science **409**(2): 336.

Bedja, I. and Kamat, P. V. (1995). "Capped Semiconductor Colloids - Synthesis and Photoelectrochemical Behavior of Tio2-Capped Sno2 Nanocrystallites." Journal of Physical Chemistry **99**(22): 9182.

Bell, A. T. (2003). "The impact of nanoscience on heterogeneous catalysis." Science **299**(5613): 1688.

Bickley, R. I., Gonzalezcarreno, T., Lees, J. S., Palmisano, L. and Tilley, R. J. D. (1991). "A Structural Investigation of Titanium-Dioxide Photocatalysts." Journal of Solid State Chemistry **92**(1): 178.

Binder, K. and Baumgärtner, A. (1984). Applications of the Monte Carlo method in statistical physics. Berlin; New York, Springer-Verlag.

Binder, K. and Heermann, D. W. (1988). Monte Carlo simulation in statistical physics: an introduction. Berlin; New York, Springer-Verlag.

Binder, K. and Landau, D. P. (1992). "Capillary Condensation in the Lattice Gas-Model - a Monte-Carlo Study." Journal of Chemical Physics **96**(2): 1444.

Bird, R. B., Stewart, W. E. and Lightfoot, E. N. (2002). Transport phenomena. New York, J. Wiley.

Birkett, G. R. and Do, D. D. (2006). "The adsorption of water in finite carbon pores." Molecular Physics **104**(4): 623.

Bock, H. and Schoen, M. (1999). "Phase behavior of a simple fluid confined between chemically corrugated substrates." Physical Review E **59**(4): 4122.

Boehm, H. P. (1971). "Acidic and Basic Properties of Hydroxylated Metal-Oxide Surfaces." Discussions of the Faraday Society(52): 264.

Bohlen, H. and Schoen, M. (2005). "Effect of fluid-substrate attraction and pore geometry on fluid adsorption." Journal of Chemical Physics **123**(12).

Boonstra, A. H. and Mutsaers, C. A. H. A. (1975). "Photohydrogenation of Ethyne and Ethene on Surface of Titanium-Dioxide." Journal of Physical Chemistry **79**(19): 2025.

Brandriss, S. and Margel, S. (1993). "Synthesis and Characterization of Self-Assembled Hydrophobic Monolayer Coatings on Silica Colloids." Langmuir **9**(5): 1232.

Bredow, T. and Jug, K. (1995). "Theoretical Investigation of Water-Adsorption at Rutile and Anatase Surfaces." Surface Science **327**(3): 398.

Brinker, C. J. (1988). "Hydrolysis and Condensation of Silicates - Effects on Structure." Journal of Non-Crystalline Solids **100**(1-3): 31.

Brodskaya, E. N. and Piotrovskaya, E. M. (1994). "Monte-Carlo Simulations of the Laplace Pressure-Dependence on the Curvature of the Convex Meniscus in Thin Unwetted Capillaries." Langmuir **10**(6): 1837.

Brown, G. M. (1960). "Heat or Mass Transfer in a Fluid in Laminar Flow in a Circular or Flat Conduit." AIChE Journal **6**(2): 179.

Cai, R., Hashimoto, K., Kubota, Y. and Fujishima, A. (1992). "Increment of Photocatalytic Killing of Cancer-Cells Using TiO_2 with the Aid of Superoxide-Dismutase." Chemistry Letters(3): 427.

Cai, R. X., Kubota, Y., Shuin, T., Sakai, H., Hashimoto, K. and Fujishima, A. (1992). "Induction of Cytotoxicity by Photoexcited TiO_2 Particles." Cancer Research **52**(8): 2346.

Carman, P. C. (1953). "Properties of Capillary-Held Liquids." Journal of Physical Chemistry **57**(1): 56.

Carp, O., Huisman, C. L. and Reller, A. (2004). "Photoinduced reactivity of titanium dioxide." Progress in Solid State Chemistry **32**(1-2): 33.

Carraway, E. R., Hoffman, A. J. and Hoffmann, M. R. (1994). "Photocatalytic Oxidation of Organic-Acids on Quantum-Sized Semiconductor Colloids." Environmental Science & Technology **28**(5): 786.

Carrizos, I., Moreno, F. and Munuera, G. (1971). "Comparative Study on Water Vapor Adsorption on Anatase and Rutile Varieties of TiO_2." Anales De Quimica-International Edition **67**(11): 919.

Chan, C. K., Porter, J. F., Li, Y. G., Guo, W. and Chan, C. M. (1999). "Effects of calcination on the microstructures and photocatalytic properties of nanosized titanium dioxide powders prepared by vapor hydrolysis." Journal of the American Ceramic Society **82**(3): 566.

Clark, W. C., Haynes, J. M. and Mason, G. (1968). "Liquid Bridges between a Sphere and a Plane." Chemical Engineering Science **23**(7): 810.

Coasne, B. and Pellenq, R. J. M. (2004). "Grand canonical Monte Carlo simulation of argon adsorption at the surface of silica nanopores: Effect of pore size, pore morphology, and surface roughness." Journal of Chemical Physics **120**(6): 2913.

Conley, N., Lawal, A. and Mujumdar, A. S. (1985). "An Assessment of the Accuracy of Numerical-Solutions to the Graetz Problem." International Communications in Heat and Mass Transfer **12**(2): 209.

Cunningham, J. and Sedlak, P. (1994). "Interrelationships between Pollutant Concentration, Extent of Adsorption, TiO_2-Sensitized Removal, Photon Flux and Levels of Electron or Hole Trapping Additives.1. Aqueous Monochlorophenol-TiO_2(P25) Suspensions." Journal of Photochemistry and Photobiology a-Chemistry **77**(2-3): 255.

Datye, A. K., Riegel, G., Bolton, J. R., Huang, M. and Prairie, M. R. (1995). "Microstructural Characterization of a Fumed Titanium-Dioxide Photocatalyst." Journal of Solid State Chemistry **115**(1): 236.

de Lazzer, A., Dreyer, M. and Rath, H. J. (1999). "Particle-surface capillary forces." Langmuir **15**(13): 4551.

Debisschop, F. R. E. and Rigole, W. J. L. (1982). "A Physical Model for Liquid Capillary Bridges between Adsorptive Solid Spheres - the Nodoid of Plateau." Journal of Colloid and Interface Science **88**(1): 117.

Defay, R. and Prigogine, I. (1966). Surface tension and adsorption. New York, Wiley.

Digilov, R. (2000). "Kelvin equation for meniscuses of nanosize dimensions." Langmuir **16**(3): 1424.

Feng, A. G., McCoy, B. J., Munir, Z. A. and Cagliostro, D. (1998). "Wettability of transition metal oxide surfaces." Materials Science and Engineering a-Structural Materials Properties Microstructure and Processing **242**(1-2): 50.

Fisher, L. R. and Israelachvili, J. N. (1981). "Experimental Studies on the Applicability of the Kelvin Equation to Highly Curved Concave Menisci." Journal of Colloid and Interface Science **80**(2): 528.

Fisher, R. A. (1926). "On the capillary forces in an ideal soil; Correction of formulae given by W. B. Haines." Journal of Agricultural Science **16**: 492.

Fokin, L., Popov, V., Kalashnikov, A., Zarkova, L., Pirgov, P. and Petkov, I. (2001). "Joint Russian and Bulgarian academies of sciences database of intermolecular potentials and diffusion coefficients for components of the CVD processes in microelectronics." International Journal of Thermophysics **22**(5): 1497.

Fox, M. A. and Dulay, M. T. (1993). "Heterogeneous Photocatalysis." Chemical Reviews **93**(1): 341.

Frenkel, D. and Smit, B. (2002). Understanding molecular simulation: from algorithms to applications. San Diego, Calif.; London, Academic.

Fujishim.A and Honda, K. (1972). "Electrochemical Photolysis of Water at a Semiconductor Electrode." Nature **238**(5358): 37.

Gamble, L., Hugenschmidt, M. B., Campbell, C. T., Jurgens, T. A. and Rogers, J. W. (1993). "Adsorption and Reactions of Tetraethoxysilane (Teos) on Clean and Water-Dosed Titanium-Dioxide (110)." Journal of the American Chemical Society **115**(25): 12096.

Gamble, L., Jung, L. S. and Campbell, C. T. (1996). "Decomposition and protonation of surface ethoxys on TiO2(110)." Surface Science **348**(1-2): 1.

Gatica, S. M. and Cole, M. W. (2005). "Capillary condensation in cylindrical nanopores." Physical Review E **72**(4).

Gleiter, H. (1989). "Nanocrystalline Materials." Progress in Materials Science **33**(4): 223.

Haines, W. B. (1925). "Studies in the physical properties of soils II A note on the cohesion developed by capillary forces in an ideal soil." Journal of Agricultural Science **15**: 529.

Hameri, K., Kulmala, M., Krissinel, E. and Kodenyov, G. (1996). "Homogeneous nucleation in a laminar flow diffusion chamber: The operation principles and possibilities for quantitative rate measurements." Journal of Chemical Physics **105**(17): 7683.

Hemming, C. J. and Patey, G. N. (2006). "Nanoscopic liquid bridges between chemically patterned atomistic walls." Journal of Physical Chemistry B **110**(8): 3764.

Herrmann, J. M. (1999). "Heterogeneous photocatalysis: fundamentals and applications to the removal of various types of aqueous pollutants." Catalysis Today **53**(1): 115.

Hill, T. L. (1956). Statistical mechanics: principle and selected applications. New York, McGraw-Hill.

Hill, T. L. (1986). An introduction to statistical thermodynamics. New York, Dover Publications.

Hill, T. L. (1987). Statistical mechanics: principles and selected applications. New York, Dover Publications.

Hinshelwood, C. N. (1926). The kinetics of chemical change in gaseous systems. Oxford, Clarendon press.

Hoffmann, M. R., Martin, S. T., Choi, W. Y. and Bahnemann, D. W. (1995). "Environmental Applications of Semiconductor Photocatalysis." Chemical Reviews **95**(1): 69.

Hollabaugh, C. and Chessick, J. J. (1961). "Adsorption of Water and Polar Paraffinic Compounds onto Rutile." Journal of Physical Chemistry **65**(1): 109.

Homann, T., Bredow, T. and Jug, K. (2004). "Adsorption of small molecules on the anatase(100) surface." Surface Science **555**(1-3): 135.

Hotta, K., Takeda, K. and Iinoya, K. (1974). "Capillary Binding Force of a Liquid Bridge." Powder Technology **10**(4-5): 231.

Hurum, D. C., Agrios, A. G., Gray, K. A., Rajh, T. and Thurnauer, M. C. (2003). "Explaining the enhanced photocatalytic activity of Degussa P25 mixed-phase TiO2 using EPR." Journal of Physical Chemistry B **107**(19): 4545.

Imhof, A. (2001). "Preparation and characterization of titania-coated polystyrene spheres and hollow titania shells." Langmuir **17**(12): 3579.

Ireland, J. C., Klostermann, P., Rice, E. W. and Clark, R. M. (1993). "Inactivation of Escherichia-Coli by Titanium-Dioxide Photocatalytic Oxidation." Applied and Environmental Microbiology **59**(5): 1668.

Jang, J. Y., Schatz, G. C. and Ratner, M. A. (2002). "Liquid meniscus condensation in dip-pen nanolithography." Journal of Chemical Physics **116**(9): 3875.

Jenny, B. and Pichat, P. (1991). "Determination of the Actual Photocatalytic Rate of H_2O_2 Decomposition over Suspended TiO_2 - Fitting to the Langmuir Hinshelwood Form." Langmuir **7**(5): 947.

Jin, T. and White, J. M. (1988). "Characterization of Silica Overlayers Deposited on ZrO_2 and TiO_2 by CVD of $Si(OC_2H_5)_4$." Surface and Interface Analysis **11**(10): 517.

John F. M., W. F. S., Peter E. S., and Kenneth D. B. (1995). Handbook of X-ray photoelectron spectroscopy, Physical electronics Inc.

Jurgens, T. A. and Rogers, J. W. (1995). "Reactions of Tetraethoxysilane Vapor on Polycrystalline Titanium-Dioxide." Journal of Physical Chemistry **99**(2): 731.

Kampen, N. G. v. (1981). Stochastic processes in physics and chemistry. Amsterdam; New York, North-Holland; sole distributors for the USA and Canada Elsevier North-Holland.

Kartini, I., Meredith, P., da Costa, J. C. D., Riches, J. D. and Lu, G. Q. M. (2004). "Formation of mesostructured titania thin films using isopropoxide precursors." Current Applied Physics **4**(2-4): 160.

Katz, J. L. (1970). "Condensation of a Supersaturated Vapor.1. Homogeneous Nucleation of Normal-Alkanes." Journal of Chemical Physics **52**(9): 4733.

Klein, S., Thorimbert, S. and Maier, W. F. (1996). "Amorphous microporous titania-silica mixed oxides: Preparation, characterization, and catalytic redox properties." Journal of Catalysis **163**(2): 476.

Kohonen, M. M. and Christenson, H. K. (2000). "Capillary condensation of water between rinsed mica surfaces." Langmuir **16**(18): 7285.

Kohonen, M. M., Maeda, N. and Christenson, H. K. (1999). "Kinetics of capillary condensation in a nanoscale pore." Physical Review Letters **82**(23): 4667.

Kormann, C., Bahnemann, D. W. and Hoffmann, M. R. (1991). "Photolysis of Chloroform and Other Organic-Molecules in Aqueous TiO_2 Suspensions." Environmental Science & Technology **25**(3): 494.

Kreidenweis, S. M., Flagan, R. C., Seinfeld, J. H. and Okuyama, K. (1989). "Binary Nucleation of Methanesulfonic-Acid and Water." Journal of Aerosol Science **20**(5): 585.

Kuchta, B. and Firlej, L. (2005). "Influence of strength of atom-wall interactions on adsorption mechanism." Adsorption-Journal of the International Adsorption Society **11**: 367.

Li, Q. Y., Chen, Y. F., Zeng, D. D., Gao, W. M. and Wu, Z. J. (2005). "Photocatalytic characterization of silica coated titania nanoparticles with tunable coatings." Journal of Nanoparticle Research **7**(2): 295.

Li, Z. J., Hou, B., Xu, Y., Wu, D. and Sun, Y. H. (2005). "Hydrothermal synthesis, characterization, and photocatalytic performance of silica-modified titanium dioxide nanoparticles." Journal of Colloid and Interface Science **288**(1): 149.

Lian, G. P., Thornton, C. and Adams, M. J. (1993). "A Theoretical-Study of the Liquid Bridge Forces between 2 Rigid Spherical Bodies." Journal of Colloid and Interface Science **161**(1): 138.

Libby, B. and Monson, P. A. (2004). "Adsorption/desorption hysteresis in inkbottle pores: A density functional theory and Monte Carlo simulation study." Langmuir **20**(10): 4289.

Maeda, N. and Christenson, H. K. (1999). "Direct observation of surface effects on the freezing and melting of an n-alkane." Colloids and Surfaces a-Physicochemical and Engineering Aspects **159**(1): 135.

Maeda, N. and Israelachvili, J. N. (2002). "Nanoscale mechanisms of evaporation, condensation and nucleation in confined geometries." Journal of Physical Chemistry B **106**(14): 3534.

Marmur, A. (1993). "Tip Surface Capillary Interactions." Langmuir **9**(7): 1922.

Mason, G. and Clark, W. C. (1965). "Liquid Bridges between Spheres." Chemical Engineering Science **20**(10): 859.

Matthews, R. W. (1988). "Kinetics of Photocatalytic Oxidation of Organic Solutes over Titanium-Dioxide." Journal of Catalysis **111**(2): 264.

Matthews, R. W. (1989). "Photocatalytic Oxidation and Adsorption of Methylene-Blue on Thin-Films of near-Ultraviolet-Illuminated Tio2." Journal of the Chemical Society-Faraday Transactions I **85**: 1291.

Matthews, R. W. and Mcevoy, S. R. (1992). "A Comparison of 254 Nm and 350 Nm Excitation of TiO_2 in Simple Photocatalytic Reactors." Journal of Photochemistry and Photobiology A-Chemistry **66**(3): 355.

Mayer, R. P. and Stowe, R. A. (2005). "Nodoids and toroids: comparison of two geometries for the meniscus profile of a wetting liquid between two touching isolated spheres and extensions to the model of a collection of packed spheres." Journal of Colloid and Interface Science **285**(2): 781.

Mazzoco, R. R. and Wayner, P. C. (1999). "Aqueous wetting films on fused quartz." Journal of Colloid and Interface Science **214**(2): 156.

Mcfarlane, J. S. and Tabor, D. (1950). "Adhesion of Solids and the Effect of Surface Films." Proceedings of the Royal Society of London Series a-Mathematical and Physical Sciences **202**(1069): 224.

McQuarrie, D. A. (1976). Statistical mechanics. New York, Harper & Row.

Melrose, J. C. (1966). "Model Calculations for Capillary Condensation." Aiche Journal **12**(5): 986.

Melrose, J. C. (1972). "Chemical Potential Changes in Capillary Condensation." Journal of Colloid and Interface Science **38**(2): 312.

Melrose, J. C. and Wallick, G. C. (1967). "Exact Geometrical Parameters for Pendular Ring Fluid." Journal of Physical Chemistry **71**(11): 3676.

Metropolis, N., Rosenbluth, A. W., Rosenbluth, M. N., Teller, A. H. and Teller, E. (1953). "Equation of State Calculations by Fast Computing Machines." Journal of Chemical Physics **21**(6): 1087.

Milis, A., Peral, J., Domenech, X. and Navio, J. A. (1994). "Heterogeneous Photocatalytic Oxidation of Nitrite over Iron-Doped TiO_2 Samples." Journal of Molecular Catalysis **87**(1): 67.

Miyahara, M., Kanda, H., Yoshioka, T. and Okazaki, M. (2000). "Modeling capillary condensation in cylindrical nanopores: A molecular dynamics study." Langmuir **16**(9): 4293.

Moody, M. P. and Attard, P. (2001). "Curvature dependent surface tension from a simulation of a cavity in a Lennard-Jones liquid close to coexistence." Journal of Chemical Physics **115**(19): 8967.

Moody, M. P. and Attard, P. (2003). "Curvature-dependent surface tension of a growing droplet." Physical Review Letters **91**(5).

Nakajima, H., Mori, T., Shen, Q. and Toyoda, T. (2005). "Photoluminescence study of mixtures of anatase and rutile TiO2 nanoparticles: Influence of charge transfer between the nanoparticles on their photo luminescence excitation bands." Chemical Physics Letters **409**(1-3): 81.

Nguyen, Q. T., Kidder, J. N. and Ehrman, S. H. (2002). "Hybrid gas-to-particle conversion and chemical vapor deposition for the production of porous alumina films." Thin Solid Films **410**(1-2): 42.

Nyquist, R. A., Putzig, C. L., Leugers, M. A., Kagel, R. O. and Nyquist, R. A. (1997). The handbook of infrared and Raman spectra of inorganic compounds and organic salts. San Diego, Academic Press.

Ohno, T., Sarukawa, K., Tokieda, K. and Matsumura, M. (2001). "Morphology of a TiO2 photocatalyst (Degussa, P-25) consisting of anatase and rutile crystalline phases." Journal of Catalysis **203**(1): 82.

Okamoto, K., Yamamoto, Y., Tanaka, H., Tanaka, M. and Itaya, A. (1985). "Heterogeneous Photocatalytic Decomposition of Phenol over TiO_2 Powder." Bulletin of the Chemical Society of Japan **58**(7): 2015.

Orr, F. M., Scriven, L. E. and Rivas, A. P. (1975). "Pendular Rings between Solids - Meniscus Properties and Capillary Force." Journal of Fluid Mechanics **67**(Feb25): 723.

Pandit, R., Schick, M. and Wortis, M. (1982). "Systematics of Multilayer Adsorption Phenomena on Attractive Substrates." Physical Review B **26**(9): 5112.

Papadopoulou, A., Vanswol, F. and Marconi, U. M. B. (1992). "Pore-End Effects on Adsorption Hysteresis in Cylindrical and Slit-Like Pores." Journal of Chemical Physics **97**(9): 6942.

Perry, R. H., Green, D. W. and Maloney, J. O. (1997). Perry's chemical engineers' handbook. New York, McGraw-Hill.

Pol, V. G., Pol, S. V., Gofer, Y., Calderon-Moreno, J. and Gedanken, A. (2004). "Thermal decomposition of tetraethylorthosilicate (TEOS) produces silicon coated carbon spheres." Journal of Materials Chemistry **14**(6): 966.

Porter, J. F., Li, Y. G. and Chan, C. K. (1999). "The effect of calcination on the microstructural characteristics and photoreactivity of Degussa P-25 TiO_2." Journal of Materials Science **34**(7): 1523.

Puibasset, J. (2005). "Capillary condensation in a geometrically and a chemically heterogeneous pore: A molecular simulation study." Journal of Physical Chemistry B **109**(10): 4700.

Puibasset, J. and Pellenq, R. J. M. (2005). "Water adsorption in disordered mesoporous silica (Vycor) at 300 K and 650 K: A Grand Canonical Monte Carlo simulation study of hysteresis." Journal of Chemical Physics **122**(9).

Rocken, P. and Tarazona, P. (1996). "Capillary condensation in structured pores." Journal of Chemical Physics **105**(5): 2034.

Sato, N. L., Fujisawa, N., Maeda, Y. and Fukui, M. (1992). "A Method to Eliminate Odor from Recirculating Air in the Animal House." Experimental Animals **41**(1): 39.

Schindler, K. M. and Kunst, M. (1990). "Charge-Carrier Dynamics in TiO_2 Powders." Journal of Physical Chemistry **94**(21): 8222.

Seto, T., Shimada, M. and Okuyama, K. (1995). "Evaluation of Sintering of Nanometer-Sized Titania Using Aerosol Method." Aerosol Science and Technology **23**(2): 183.

Soler-Illia, G. J. D. A., Louis, A. and Sanchez, C. (2002). "Synthesis and characterization of mesostructured titania-based materials through evaporation-induced self-assembly." Chemistry of Materials **14**(2): 750.

Spanhel, L., Weller, H. and Henglein, A. (1987). "Photochemistry of Semiconductor Colloids.22. Electron Injection from Illuminated Cds into Attached Tio2 and Zno Particles." Journal of the American Chemical Society **109**(22): 6632.

Stafford, U., Gray, K. A. and Kamat, P. V. (1996). "Photocatalytic degradation of organic contaminants: Halophenols and related model compounds." Heterogeneous Chemistry Reviews **3**(2): 77.

Strey, R., Wagner, P. E. and Schmeling, T. (1986). "Homogeneous Nucleation Rates for N-Alcohol Vapors Measured in a 2-Piston Expansion Chamber." Journal of Chemical Physics **84**(4): 2325.

Sun, B., Vorontsov, A. V. and Smirniotis, P. G. (2003). "Role of platinum deposited on TiO2 in phenol photocatalytic oxidation." Langmuir **19**(8): 3151.

Thiel, P. A. and Madey, T. E. (1987). "The Interaction of Water with Solid-Surfaces - Fundamental-Aspects." Surface Science Reports **7**(6-8): 211.

Tolman, R. C. (1938). The principles of statistical mechanics. Oxford, The Clarendon Press.

Twu, C. H. and Coon, J. E. (1996). "CEOS/A(E) mixing rules constrained by vdW mixing rule and second virial coefficient." AIChE Journal **42**(11): 3212.

van Dyk, A. C. and Heyns, A. M. (1998). "Dispersion stability and photo-activity of rutile (TiO2) powders." Journal of Colloid and Interface Science **206**(2): 381.

Verweij, H. (1998). "Nanocrystalline and nanoporous ceramics." Advanced Materials **10**(17): 1483.

Vinodgopal, K., Bedja, I. and Kamat, P. V. (1996). "Nanostructured semiconductor films for photocatalysis. Photoelectrochemical behavior of SnO2/TiO2 composite systems and its role in photocatalytic degradation of a textile azo dye." Chemistry of Materials **8**(8): 2180.

Vohra, V. and Heist, R. H. (1996). "The flow diffusion nucleation chamber: A quantitative tool for nucleation research." Journal of Chemical Physics **104**(1): 382.

Wang, D. Y. and Caruso, F. (2002). "Polyelectrolyte-coated colloid spheres as templates for sol-gel reactions." Chemistry of Materials **14**(5): 1909.

Wang, Y. H., Supothina, S., De Guire, M. R., Heuer, A. H., Collins, R. and Sukenik, C. N. (1998). "Deposition of compact hydrous aluminum sulfate thin films on titania particles coated with organic self-assembled monolayers." Chemistry of Materials **10**(8): 2135.

Willett, C. D., Adams, M. J., Johnson, S. A. and Seville, J. P. K. (2000). "Capillary bridges between two spherical bodies." Langmuir **16**(24): 9396.

Wu, C. Y., Yue, Y. H., Deng, X. Y., Hua, W. M. and Gao, Z. (2004). "Investigation on the synergetic effect between anatase and rutile nanoparticles in gas-phase photocatalytic oxidations." Catalysis Today **93-95**: 863.

Xia, B., Huang, H. Z. and Xie, Y. C. (1999). "Heat treatment on TiO_2 nanoparticles prepared by vapor-phase hydrolysis." Materials Science and Engineering B-Solid State Materials for Advanced Technology **57**(2): 150.

Yoshioka, Y., Tsujimoto, M., Koshino, M., Nemoto, T., Ogawa, T., Kurata, H. and Isoda, S. (2004). "Characterization of Gratzel dye on TiO_2 particles by transmission electron microscopy." Molecular Crystals and Liquid Crystals **424**: 95.

Yu, J. C., Ho, W. K., Lin, J., Yip, K. Y. and Hong, P. K. (2003). "Photocatalytic activity, antibacterial effect, and photoinduced hydrophilicity of TiO_2 films coated on a stainless steel substrate." Environmental Science & Technology **37**(10): 2296.

Yu, J. G., Yu, J. C., Ho, W. K. and Jiang, Z. T. (2002). "Effects of calcination temperature on the photocatalytic activity and photo-induced super-hydrophilicity of mesoporous TiO2 thin films." New Journal of Chemistry **26**(5): 607.

Yu, S. Z., Wong, T. K. S., Hu, X. and Pita, K. (2003). "The effect of TEOS/MTES ratio on the structural and dielectric properties of porous silica films." Journal of the Electrochemical Society **150**(5): F116.

Zafra, A., Garcia, J., Milis, A. and Domenech, X. (1991). "Kinetics of the Catalytic-Oxidation of Nitrite over Illuminated Aqueous Suspensions of TiO_2." Journal of Molecular Catalysis **70**(3): 343.

Zhang, F. X., Chen, J. X., Zhang, X., Gao, W. L., Jin, R. C., Guan, N. J. and Li, Y. Z. (2004). "Synthesis of titania-supported platinum catalyst: The effect of pH on morphology control and valence state during photodeposition." Langmuir **20**(21): 9329.

Zimon, A. D. (1982). Adhesion of dust and powder. New York, Consultants Bureau.